On Gust Buffeting Design of Slender Chimneys - Building Interference and Fatigue

by

Hodei Aizpurua Aldasoro

born 28 November 1985

in San Sebastian, Spain

Von der Fakultät Architektur, Bauingenieurwesen und Umweltwissenschaften
der Technischen Universität Carolo-Wilhelmina zu Braunschweig
zur Erlangung des Grades eines Doktoringenieurs (Dr.-Ing.)
genehmigte Dissertation

Eingereicht am:	23. April 2014
Disputation am:	31. Oktober 2014
Berichterstatter:	Prof. Dr.-Ing. Dr.-Ing. E.h. Udo Peil Prof. Dr.-Ing. Hans-Jürgen Niemann

Schriftenreihe des Instituts für Stahlbau

Heft 2

Hodei Aizpurua Aldasoro

On Gust Buffeting Design of Slender Chimneys – Building Interference and Fatigue

Shaker Verlag
Aachen 2015

Bibliographic information published by the Deutsche Nationalbibliothek
The Deutsche Nationalbibliothek lists this publication in the Deutsche Nationalbibliografie; detailed bibliographic data are available in the Internet at http://dnb.d-nb.de.

Zugl.: Braunschweig, Techn. Univ., Diss., 2014

Printed in Germany.

ISBN 978-3-8440-3538-4
ISSN 2198-8722

Shaker Verlag GmbH • P.O. BOX 101818 • D-52018 Aachen
Phone: 0049/2407/9596-0 • Telefax: 0049/2407/9596-9
Internet: www.shaker.de • e-mail: info@shaker.de

I dedicate this work to all the things, that my parents had to give up in order to invest in my education and in the education of my siblings.

'Ceterum censeo Carthaginem esse delendam'.

Cato the Elder (3rd century BC)

Acknowledgements

First of all I want to thank my tutor Univ.-Prof. Dr.-Ing. Dr.-Ing. E.h. Udo Peil for giving me the possibility to write this PhD work at the Institute of Steel Structures of the Technische Universität Braunschweig. It was a privilege for me to carry out this work as a member of his wind engineering team. I will always remember the conversations we had about music, politics, the correct use of the German language and his interest in learning about the Basque language. Therefore, the fruitful cooperation with Prof. Peil was not only focused on wind engineering, but also on not less important cultural aspects.

I express my gratitude to the Basque Government for the sponsorship of the work between 2010 and 2014. Specially, I am grateful to Prof. Pedro Luis Arias Ergueta for his support and interest in the research project during these last years. I would like to thank Ms. Lourdes Arana Uli for her fundamental support in funding possibilities for a doctoral project. I express also my gratitude to CICIND for the financial support of the research projects associated with this work. A special mention also to Prof. Iñigo Puente from TECNUN University of Navarra for introducing me in the research field and convincing how useful is a PhD thesis for an engineer.

All my gratitude to Univ.-Prof. Dr. sc. techn. Klaus Thiele for his support, interesting questions and recommendations during the last years of the project. Special thanks to Prof. Dr.-Ing. Hans-Jürgen Niemann from Ruhr-Universität Bochum, for his interest in the research and for evaluating the presented work. Due to his international reputation in wind engineering, it is an honour for me that he accepted to support this work.

The most important scientific support I had here during the last four years was given by Dr.-Ing. Mathias Clobes. We had many inspiring discussions and his ideas have always been vital for the progress of the work. I remember his motivation during my first months in Braunschweig; allowing me to travel with him to international conferences, in particular to St. Petersburg in May 2011. That was my first international experience and I will never forget it.

Thomas Höbbel M.Sc. has also been very helpful during this time, having a parallel trajectory and being a co-worker during the construction of the wind tunnel.

Special thanks are addressed to Dr.-Ing. Frank Kemper from RTWH Aachen, who selflessly helped me during the development of the chapter regarding the wind-induced fatigue. I want to thank Prof. Giovanni Solari from Genoa University for providing me advices about the gust response factor approach and for accessing me additional litera-

ture. I would also like to acknowledge Prof. Dr. Bernd Leitl from Universität Hamburg for the useful advices provided for the construction of the wind tunnel, as well as for allowing us to visit the facilities of the Meteorological Institute.

I will emphasize the excellent atmosphere at the Institute of Steel Structures provided by people like Dipl.-Ing. Oliver Steiln, Dr.-Ing. Andreas Willecke, Dr.-Ing. Arno Kirch, Dipl.-Ing. Florian Minuth-Hadi, Dipl.-Ing. Julian Unglaub, Dr.-Ing. Jorge Muñoz Barrantes, Dipl.-Ing. Ingo Schendel, Ding Cai M.Sc. etc. Thank you for your friendly company. I am also grateful to Eric Kuate Simo M.Sc. due to his work as loyal student assistant since the beginning of the work. Dipl.-Ing. Nahia Jimenez de Pablo and Fabian Fengler M.Sc. have also supported this work with their interesting contributions to the institute. I would also like to mention the comprehensive effort made by my friend Christian Simon, who thoroughly proofread the grammar, syntax and style of this work. My gratitude to Jose Mari Sasieta for his drawings, that aim to combine nature, wind and art inside a scientific book.

This work is the summary of a personal effort during the last years, but also a long-term educational investment of my parents Ana and Isidro. Without their daily support, perseverance and discipline this work would not have been possible.

Finally, I want to acknowledge my girlfriend Alina for her personal, emotional and intellectual support during these last years. I have no words to express my gratitude to her.

Hodei Aizpurua Aldasoro
Hamburg, March 2014

Abstract

This work describes the experimental and numerical investigation about the improvement of the buffeting wind design of industrial slender chimneys considering interference effects and long-term wind profile statistics.

The first part of the investigations is related to the along-wind response design of slender chimneys considering the frequent perturbations on the wind field associated with the interference effect. This phenomenon occurs always in the presence of nearby buildings and its importance increases if the slenderness of the chimney becomes larger. The experimental study is carried out in the boundary layer wind tunnel of the Institute of Steel Structures of the TU Braunschweig. To simulate the effect of power houses on the wind flow, a parametric study on the building shape has been carried out. Different building shapes, positions of the chimney and wind directions have been considered. For each configuration, the wind field characteristics acting on the chimney have been measured. Using this information, the buffeting response of a 150 m high propped chimney has been numerically calculated assuming quasi-steady wind loading. The results show a significant increase of the bending moment at the roof support with respect to the undisturbed flow associated with the Eurocode 1. The aerodynamic admittance function under disturbed wind conditions has been also determined experimentally. The wind load acting on a chimney model is calculated again in the wind tunnel using the high frequency force balance technique. The results obtained demonstrate that the aerodynamic admittance function does not vary with respect to the undisturbed configuration. The design approach in Eurocode 1 is based on a procedure proposed by Solari and cannot be implemented when chimneys are supported at the top of the building, since there is no constant sign in the mode shape. The proposed modification takes into account the roof supported structural system as well as the corrected wind profiles and turbulence spectra due to the interference effect. In other words, a linear mode shape from the top of the building to the top of the chimney is chosen. The study reveals a big dependency of the gust response factor on the cantilevered length of the propped chimney. Finally, an increasing factor that fully covers the interference effect as well as the change of the structural configuration for different eigenfrequencies and heights is proposed. It has to be applied to correct the calculation following the Eurocode 1 procedure for the cantilevered length of the chimney.

On the contrary to the first part of the investigations associated with extreme wind situations, the second part covers the fatigue life prognosis considering low and moderate wind conditions. Using the useful information about long-term wind statistics provided by previous works, a realistic analysis of the expected fatigue damage is carried out. The wind data measured in Gartow, a rural area located in Northern Germany with a roughness grade equivalent to an industrial area, was useful to classify the mean wind speed profiles in six different shapes. To study the fatigue prognosis, a Monte-Carlo simulation has been carried out using a large number of synthetic profiles generated from the presented statistics. For each generated wind profile, the buffeting response of a 150 m tall chimney is individually calculated in the frequency domain. Starting from the spectral information of the bending moment obtained at the foundation, the Dirlik method has been applied to calculate the probability distribution of the stress amplitudes in order to study the expected fatigue damage of the structure. From these results, load collectives for a lifetime of 50 years have been generated. The consideration of six wind classes c yields to a more economic design as compared to a scenario where only the logarithmic wind profile shape is considered. The damping, eigenfrequency and wind statistics at site Gartow have a direct influence on the shape of the load collective, thus the unique application of the proposal given in the Eurocode for each structure and site can produce a largely overestimated fatigue prognosis.

Zusammenfassung

Für schwingungsanfällige Tragwerke wie hohe Stahlschornsteine ist die böige Windeinwirkung bemessungsrelevant. Im Rahmen dieser Arbeit wurden experimentelle und numerische Untersuchungen zur Böenbeanspruchung durchgeführt. Hierbei wurde ein besonderer Blick auf dem Einfluss von Interferenzeffekten durch benachbarte Bebauung, sowie eine Ermüdungsprognose unter Berücksichtigung von realistischen Windprofilen geworfen.

Häufig werden Schornsteine an unmittelbar neben hohen Bauwerken errichtet. Diese benachbarten Gebäude beeinflussen die Windbelastung auf den Schornstein in Abhängigkeit von dessen dynamischen Eigenschaften deutlich, es kann zu höheren Beanspruchungen gegenüber der Windsituation ohne das benachbarte Gebäude kommen. Es hat darüber hinaus wirtschaftliche Vorteile, den Stahlschornstein mit dem benachbarten Gebäude zu verbinden damit das statische System vom Kragarm zum günstigeren Einfeldträger mit Kragarm zu verändern. Am Institut für Stahlbau der Technischen Universität Braunschweig wurden Untersuchungen an mastäblichen Modellen im Grenzschichtwindkanal durchgeführt. Dabei wurden die Gebäudeform, Position des Schornsteins bezüglich des Gebäudes sowie Windrichtung variiert. Für jede Konfiguration wird das gestörte Windfeld gemessen. Mit dieser Information wurden eine dynamische Berechnungen für verschiedene Modellschornsteine unter Böenrregung unter Verwendung des quasi-stationärem Windlastansatzes durchgeführt. Hierbei zeigt sich, dass das benachbarte Bauwerk, in Abhängigkeit von Windwinkel und Position des Schornsteines, die für die Beanspruchung des Schornsteins magebende Windstruktur stark beeinflusst und damit zu einer bemessungsrelevanten Erhöhung der Beanspruchung führt. Um einen direkten Vergleich zwischen die vorliegenden Untersuchungen und dem in Eurocode EN 1991-1-4 verankerten Verfahren zur Ermittlung des Böenreakstionsfaktors zu ermöglichen, sind Informationen die aerodynamische Admittanzfunktion notwendig. Zur Bestimmung dieser Admittanzfunktion wurden im Windkanal die Windkräfte an einem Schornsteinmodell mit Hilfe einer Windkanalwaage erfasst. Die Ergebnisse zeigen keinen deutlichen Einfluss des Interferenzeffektes auf den Verlauf der aerodynamischen Admittanzfunktion. Das in EN 1991-1-4 beschriebener Verfahren zur Böenerregung gilt jedoch nur für ein vertikales Kragsystem unter Berücksichtigung der Grundschwingungsform. Eine Anwendung auf den Fall einer seitlichen Verbindung des Schornsteines mit dem Gebäude und das so veränderte statische System ist jedoch nicht möglich. In dieser Arbeit wird ein Verfahren zur Ermittlung des

Böenreaktionsfaktors vorgeschlagen, das die Interferenzeffekte sowie das veränderlichen statischen System berücksichtigt.

Darüber hinaus wird in dieser Arbeit ein Beitrag zur Ermüdung von Stahlschornsteine unter Böerregung vorgestellt. Mit Hilfe von statistischen Auswertungen gemessener Windprofile wird eine verbesserte Prognose der Lebensdauer durchgeführt. Grundlage dieser Statistik sind die Langzeitmessdaten am Mast Gartow II der seit mehr als 20 Jahre vom Institut für Stahlbau betrieben wird. Die Unterteilung der gemessenen Windprofile in sechs verschiedenen Windprofilklassen auf Basis einer vorangegangenen Arbeit wird im Rahmen einer Monte-Carlo Simulation der Böerregung eines Stahlschornsteines berücksichtigt. Die Berechnung erfolgte im Frequenzbereich mit entsprechend der Langzeitstatistik variierenden Windprofilformen. Die Häufigkeitsverteilung der Doppelspannungsamplitude wurde aus den Antwortspektren mittels der Methode nach Dirlik bestimmt. Diese Methode erlaubt die Bestimmung der Wahrscheinlichkeitsdichtefunktion der Doppelspannungsamplitude, unabhängig von der Bandbreite des Antwortprozesses. Die Lastkollektive nach EN 1991-1-4 basieren hingegen auf der Annahme einer schmalbandigen Antwortprozesses für einen Einfreiheitsgradschwinger. Die Betrachtung sechs unterschiedlicher Windprofilformen, fhrt zu einer Reduzierung der erwarteten Ermüdungsbeanspruchung der Struktur während ihrer Lebensdauer. Windstatistik und strukturelle Parameter sind entscheidend um eine realistische Lebensdauer prognostizieren zu können.

Contents

Notation

Latin Variables

A	scale parameter [m/s]
A_{ref}	reference area [m^2]
$a(f_0, \zeta)$	coefficient
B_j	width of element j [m]
$b(\zeta)$	coefficient
C_{D0}	two dimensional drag coefficient
C_{Ds}	overall drag coefficient
C_x, C_y, C_z	decay coefficients
$\mathbf{COV}_{\bar{U}}$	covariance matrix of $\bar{U}(z)$
c	wind class
$c_0(z)$	orography factor at height z
$c_r(z)$	roughness factor at height z
$c_s c_d$	structural factor
D_{ext}	diameter of the chimney [m]
D	structural damage [-]
D_j	deep of the element j [m]
$\mathbf{D}$	damping matrix

$\mathbf{D}_{\text{mech}}$	mechanical damping matrix
$\mathbf{D}_{\text{aero}}$	aerodynamic damping matrix
$E[P]$	expected number of peaks
$E[0]$	expected number of zero-crossings
$\bar{F}(z)$	mean wind force [N]
f	frequency [Hz]
f_H	correction factor on C_{D0} for effect of free end
f_L	normalized frequency
f_S	correction factor on C_{D0} for effect of shear flow
f_i	natural frequencies [Hz]
f_0	fundamental frequency [Hz]
f_v	vortex-shedding frequency[Hz]
$\mathbf{f}$	force vector
G_x	gust response factor [-]
g_x	peak factor
H	height of the chimney [m]
H^*	height of the cantilevered part $H^* = H - h$ [m]
H^c	ocurrence frequency of the wind class c [%]
$\lvert H(f)\rvert^2$	mechanical transfer function
$\mathbf{H}(f)$	mechanical transfer matrix
h	height of the adjacent building [m]
$I_u(z)$	turbulence intensity at height z [-]
IF_{G_x}	increasing factor of the gust response factor G_x [-]
i	node index
j	element index
$K_{a,b}$	wind structure-dependent factors

$K_{x,z}$	factors included in the aerodynamic function
$\mathbf{K}$	stiffness matrix
k	shape parameter [m/s]
k_i^c, k_i^p	factors of calculation ($i = 1...6$)
k_r	terrain factor
k_r/D_{ext}	rib ratio
k_s/D_{ext}	roughness ratio
L_j	length of the element j [m]
$L_u(z)$	integral length scale at height z [m]
$L^x(z)$	wave length [m]
m_i	statistical moments
$\mathbf{L}$	lower triangular matrix
$\mathbf{M}$	mass matrix
$N'(\Delta\sigma)$	probability distribution of stress amplitude $\Delta\sigma$ for period T
N_G	number of occurrences of a certain load level
$p(\bar{U})$	probability density function of the mean wind speed $\bar{U}$
$p(\Delta\sigma)$	probability density function of the stress amplitudes $\Delta\sigma$
Q	background factor
R	resonant response factor
R_D	reduction factor of the damage D
Re	Reynolds number
$R_N(z, f)$	normalized power spectral density function at height z
$R_y(z, f)$	cross wind aerodynamic admittance function
$R_z(z, f)$	vertical aerodynamic admittance function
$\mathbf{r}$	random vector
S_t	Strouhal number

$S_u(z, f)$	PSDF at height z [(m/s)^2· s]
$S^*_{u-eq}(f)$	equivalent wind spectrum EWST
$S_{uu}(P_1, P_2, f)$	cross-spectrum between points P_1 and P_2 [(m/s)^2· s]
$\mathbf{S_{ff}}(f)$	spectral matrix of wind forces
$S_x(z, f)$	PSDF of structural displacements x at height z [(m)^2· s]
T	time period [s]
T_{Life}	design timelife of the structure [s]
T_{ref}	reference time period [s]
$T_u(z)$	integral time scale at height z [s]
t	wall thickness [mm]
$\bar{U}(z)$	mean wind speed at height z [m/s]
$\bar{U}_d(z)$	corrected mean wind speed at height z [m/s]
U_b	basic wind velocity [m/s]
u	aleatory component of wind speed [m/s]
$u^*_{eq}(t)$	equivalent turbulent fluctuation [-]
u_*	friction velocity [m/s]
W	section modulus [m^3]
$\bar{X}(z)$	mean structural response [m]
$\hat{X}(z)$	maximal structural response [m]
z	height above the ground [m]
z_d	zero-plane displacement [m]
z_G	height of the beginning of the geostrophic wind [m]
z_{ref}	reference height for the mean wind speed [m]
z_s	reference height
z_0	roughness length [m]

Greek Variables

α	factor for the Rayleigh damping
α_{I_u}	exponent of the turbulence intensity profile profile $I_u(z)$
α_{L_u}	exponent of the integral length scale $L_u(z)$
$\alpha_{\bar{U}}$	exponent of the mean wind speed profile $\bar{U}(z)$
β	factor for the Rayleigh damping
$\beta_{\bar{U}}(z,\theta)$	correction factor of the mean wind speed $\bar{U}(z)$
$\Gamma(x)$	Gamma function
γ	irregularity factor
$\gamma_{i,j}(f)$	coherence function between points i and j
$\Delta_{x,y,z}$	distances between points
$\Delta\sigma$	stress amplitude [MPa]
$\Delta\sigma_D$	constant amplitude fatigue limit [MPa]
$\Delta\sigma_L$	cut-off limit [MPa]
ζ	damping ratio [%]
$\eta(f)_{y,z}$	crosswind and vertical frequency-dependent coefficients
θ	wind direction
κ	the Kármán's constant
Λ	logarithmic decrement of structural damping [-]
λ_L	geometrical scale
λ_U	velocity scale
λ_R	roughness factor (ESDU 80025)
λ_T	time scale
λ_t	turbulence factor (ESDU 80025)
μ	dynamic viscosity [Kg/s $\cdot$ m]

$\boldsymbol{\mu}_{\bar{U}}$	vector of mean wind speeds [m/s]
ν	expected frequency [Hz]
ν^*	kinematic viscosity [m^2/s]
ρ	air density [kg/m^3]
$\rho_{uu}^T(z,\tau), \rho_{uu}^x(z,r_x)$	autocorrelation functions
σ_{M_y}	standard deviation of the bending moment M_y [kN·m]
$\sigma_{\bar{U}}(z)$	standard deviation of $\bar{U}$ at height z [m/s]
$\sigma_u(z)$	standard deviation of u at height z [m/s]
$\sigma_x(z)$	standard deviation of the structural response at height z [m]
$\lvert\chi(f)\rvert^2$	aerodynamic admittance function
$\psi_0(z)$	fundamental mode of vibration of the structure

1 State of the art

In the present chapter, a brief introduction to the nature of wind is given. The atmospheric boundary layer is presented with the aim of providing the reader a simplified concept of the characteristics of the wind and the effects produced by the gusts on structural elements located inside the atmospheric boundary layer. The statistical properties of the stochastic nature of the gusty wind are defined and the assumptions made for a valid mathematical definition of this random process are also noted.

In order to distinguish between the ideal and the realistic wind acting on a chimney, the wind field at industrial areas is described. This will be focused on two main topics: firstly, the interference effect produced by a nearby industrial building on the wind structure and secondly, the consideration of realistic mean wind speed profile shapes according to long-term wind measurements. Considering these last realities, a critical point of view is given about the approaches provided in the Eurocode EN 1991-1-4 for the calculation of the along-wind response as well as for the fatigue life prognosis of industrial chimneys.

1.1 Introduction to the atmospheric boundary layer

Wind is defined as the movement of the air relative to the Earth's surface. This motion is produced by several forces caused by differences in pressure values, which are in turn produced due to the heat exchanges occurring in different regions of the Earth's surface. The large differences in the atmospheric heating process between the equator and the poles produce large-scale wind streams which are transported due to the rotation of the Earth. The interaction between the surface and the air results in the appearance of frictional forces reducing the wind speed near to the ground. The gradient of the wind speed along the height of this turbulent zone is called the *atmospheric boundary layer* and can extend up to 1000 m height (Holmes [2007]) coinciding with the geostrophic wind. Inside the atmospheric boundary layer, the average wind speed increases as the height increases, contrary to the grade of turbulence, which decreases for increasing height.

The characteristics of the terrain have a direct influence on the height of the atmospheric boundary layer. The roughness of the terrain and the physical obstacles located on the ground, such as houses or trees, produce alterations on the height of the wind speed gradient. Figure 1.1 shows three examples of different boundary layers. The mean wind

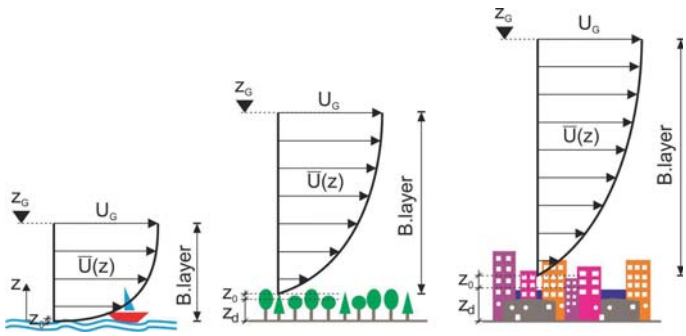

Figure 1.1: Different examples of boundary layers (Clobes u. a. [2012a])

speed profile $\bar{U}(z)$ is plotted along the height above the ground z for different terrains. The top of the boundary layer is symbolized as z_G and denotes the beginning of the geostrophic wind. It increases when the terrain's roughness becomes larger. At very low heights, the friction between air and ground surface generates vortex with zero mean wind speed. These zones are usually defined with roughness length z_0 depending on the terrain roughness. Strictly, the roughness length is situated above the zero-plane displacement z_d. This the height above the ground at which the zero wind speed is obtained as result of flow obstacles.

Table 1.1: Eurocode 1 proposal of roughness lengths z_0 for different terrain categories (EN 1991-1-4)

Roughness length z_0 [m]	Terrain category
0.003	0: Sea, coastal area
0.01	I: Lakes, negligible vegetation
0.05	II: Low vegetation and/or isolated obstacles
0.3	III: Regular cover of vegetation or buildings
1	IV: Amount of buildings

Table 1.1 shows the proposed values for the roughness length z_0 given in the Eurocode 1991-1-4. The European standard and the Spanish technical building code (CTE) distinguish between five different terrain categories depending on the ground's roughness. Other international standards make other distinctions between terrain categories: the German National Annex DIN EN 1991-1-4/NA, equivalent to the old DIN 1055-4, and the Australian AS/NZS 1170.2:2011 propose four different terrain categories while the American standard ASCE 7-05 distinguishes between three types of terrains.

1.1.1 Profile of the mean wind speed

Figure 1.2 shows the wind speed measurements carried out at different heights. It can be observed how the wind speed fluctuates during the sample period having a random behaviour produced by the turbulent boundary layer. The vast majority of structures considered in wind engineering are located inside the atmospheric boundary layer. For this purpose, it is necessary to propose mathematical models of the wind performance to ensure the engineers tools to estimate the wind loads on the projected structures.

Natural phenomena can be divided into deterministic and stochastic processes. Deterministic processes can be described using a time dependent function. That means that the events are fully determined over time. On the other hand, the stochastic or random processes, like the wind, do not follow a time dependent function. Consequently, only using statistical terms can be expected that a variable takes a certain value during a period of time. The stochastic nature of wind is considered as a stationary ergodic process allowing to treat it statistically in an easier way. Wind velocity can be divided into two parts: a mean term $\bar{U}$ that remains invariable during the observation period and a random component u with zero mean value.

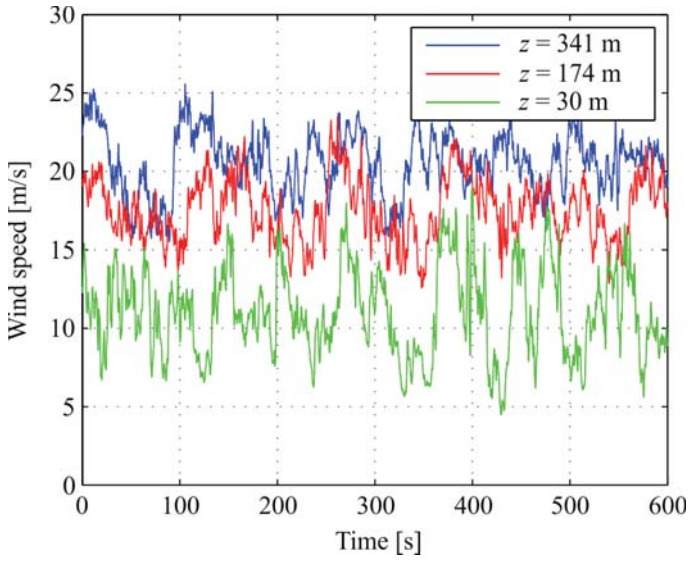

Figure 1.2: Wind speed measurements at Gartow (northern Germany) at three different heights

Using a Cartesian coordinate system, the instantaneous wind velocities are defined as:

$$\begin{aligned} U(x,y,z,t) &= \bar{U}(x,y,z) + u(x,y,z,t) \\ V(x,y,z,t) &= \bar{V}(x,y,z) + v(x,y,z,t) \\ W(x,y,z,t) &= \bar{W}(x,y,z) + w(x,y,z,t) \end{aligned} \tag{1.1}$$

In wind engineering, the longitudinal wind direction is defined in the x-axis and is considered as the term which includes the largest energy component. In order to avoid complications, some conditions are assumed to describe the turbulent flow: the wind is defined as horizontally homogeneus flow (statistical the same in longitudinal direction Stull [1991]) and the direction of the wind does not change over the height z. Consequently, the velocities at time t can be reduced to the following expression (Dyrbye u. Hansen [1997]):

$$\begin{aligned} &\text{in the longitudinal direction } U(z,t) = \bar{U}(z) + u(x,y,z,t) \\ &\text{in the lateral direction } v(x,y,z,t) \\ &\text{in the vertical direction } w(x,y,z,t) \end{aligned} \tag{1.2}$$

where the mean wind speed $\bar{U}(z)$ depends only on the height z and the fluctuations u, v and w are stochastic processes with zero mean value. Regarding the shape of the boundary layer, several methods are proposed to obtain a mathematical model to describe the mean wind speed profile $\bar{U}(z)$ above the ground.: First, applying the equations of motion of a body inside a turbulent flow, a solution of the differential equation which dictates the mean wind speed along the height can be formulated near the ground. The solution depends on the roughness length z_0 (in which the boundary condition of $\bar{U}(z_0) = 0$ has been used) and leads to the following expression:

$$\bar{U}(z) = u_* \cdot \frac{1}{\kappa} \cdot \ln \frac{z}{z_0} \tag{1.3}$$

where κ is the Kármán's constant ($\kappa \approx 0.4$) and u_* is the friction velocity. In the Eurocode 1 (EN 1991-1-4) an equivalent formula is provided to describe the mean wind speed profile along the height.

Second, a parallel formulation can be defined using a power-law profile. The origin of this formula is empirical and stems from a large number of observations:

$$\bar{U}(z) = \bar{U}(z_{ref}) \cdot \left(\frac{z}{z_{ref}} \right)^{\alpha_{\bar{U}}} \tag{1.4}$$

where z_{ref} is defined as the reference height. The exponent $\alpha_{\bar{U}}$ dominates the shape of the profile and depends on the terrain characteristics (its value increases if the roughness also increases). This type of formula is also given in other standards, as in the German National Annex DIN EN 1991-1-4/NA or in the American ASCE 7-05. Figure 1.3 shows the comparison between the two proposals of wind profile up to 200 m. For the logarithmic law the roughness length is $z_0 = 0.05$ m and for the power law the exponent $\alpha_{\bar{U}} = 0.16$ has been used.

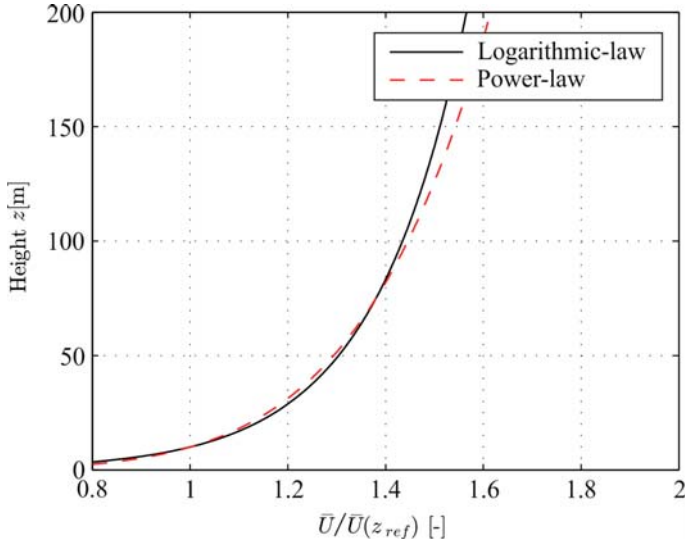

Figure 1.3: Comparison between logarithmic and power-law profile (Dyrbye u. Hansen [1997])

The previous expressions to define the profile of the mean wind speed are only valid if it is assumed that the upstream distance with uniform terrain roughness is sufficient large to stabilize the profile sufficiently. In case of small countries with short distances between different roughness categories (e.g. Germany), the application of these formulas are questionable. For example, if the wind transients from sea to land, after crossing the coastline, the increase of surface drag modifies the equilibrium of the wind at sea. There-

fore, the wind at higher levels do not start to slow down until some distance downwind the coast (Cook [1985]). The same effect can occur also from low vegetation to rural areas or from rural areas to a urban boundary. To solve this uncertainties, the National Annexes of the Eurocode propose some mixed or transitional profiles. These profiles are defined analytically in the Table NA.B.4 of the German National Annex or corrected graphically in terms of coefficients in the UK National Annex.

1.1.2 Mathematical model of the wind turbulence

As shown in Figure 1.2 the wind velocity inside the atmospheric boundary layer is highly influenced by the turbulence grade. Therefore, its fluctuations should be taken into account and mathematically modelled. The fundamental assumption is the consideration of the wind velocity as an ergodic process, equivalent definition to a homogeneous and stationary turbulent process (Stull [1991]). This can be described using four statistical functions: the root mean square, the probability density function, the autocorrelation function and the power spectral density function (Meseguer u. a. [2013]). The standard deviation for the turbulence components u, v and w can be directly calculated:

$$\sigma_u = \sqrt{\bar{u^2}} \qquad \sigma_v = \sqrt{\bar{v^2}} \qquad \sigma_w = \sqrt{\bar{w^2}} \tag{1.5}$$

The turbulence intensity is defined as the ratio between the standard deviation of the wind fluctuations and the mean wind speed:

$$I_j(z) = \frac{\sigma_j(z)}{\bar{U}(z)}\,, \quad \text{with } j = u, v, w \tag{1.6}$$

Due to the dependence of the turbulence intensity on the mean wind speed, this variable depends also on the terrain roughness. Its value increases if the roughness increases, and it decreases if the height above the ground z increases.

In wind engineering it is accepted that the fluctuations of the turbulence components of the atmospheric wind vary randomly over the time and space. It is assumed that there is a spatial coherence between the variations of the wind components. The description of the time and spatial variations of the turbulent wind can be fulfilled using the time scale and the integral length scale. These functions are described in terms of autocorrelation

functions and variances. The temporary variation of the wind turbulence can be defined using the following autocorrelation function as:

$$\rho_{uu}^{T}(z,\tau) = \frac{R_{uu}(z,\tau)}{\sigma_u^2(z)} = \frac{1}{\sigma_u^2(z)} \cdot \lim_{T\to\infty} \frac{1}{T} \int_{t_1}^{t_1+T} u(z,t) \cdot u(z,t+\tau) dt \tag{1.7}$$

This last expression can be physically described as how much information a turbulence component measurement $u(z,t)$ defined in the mean wind direction x will provide about the value of $u(z,t+\tau)$ at the same place but measured τ time later. The integral time scale represents the relationship between two wind measurements carried out at different time and could be physically defined as the transit time of the vortices inside a gust. It is defined as:

$$T_u(z) = \int_0^{\infty} \rho_{uu}^{T}(z,\tau) d\tau \tag{1.8}$$

In the same way, the integral length scale can also be defined as the average size of a gust in the wind direction:

$$L_u(z) = \int_0^{\infty} \rho_{uu}^{x}(z,r_x) dr_x \tag{1.9}$$

where $\rho_{uu}^{x}(z,r_x)$ represents the cross correlation function between two u components carried out simultaneously but separated in the wind direction by a distance r_x. Using the *frozen turbulence* concept defined by Taylor, an easy relationship between both integral scales can be used. If it is assumed that the movement of the gusts in wind direction does not decay, the statistical description of the temporal turbulence variations could be based on spatial wind field characteristics and vice-versa, without significant errors (Dyrbye u. Hansen [1997]). Therefore, the Taylor hypothesis allows the definition of the following relationship between integral scales:

$$L_u(z) = T_u(z) \cdot \bar{U}(z) \tag{1.10}$$

For the dynamic analysis of structures, it is important to know the frequency-related information of the turbulence components regarding the loading process. The structure can be excited with an important energy contribution at frequencies near the eigenfrequency of the system, which should be seriously taken into account. The power spectral

density function $S_{uu}(z, f)$ represents the energy distribution of the turbulent along-wind velocity component u in the frequency domain. Normally this function is presented in a non-dimensional form:

$$R_N(z, f) = \frac{f \cdot S_{uu}(z, f)}{\sigma_u^2} = A \cdot f_L^{-3/2} \tag{1.11}$$

It can be mathematically derived that for the high frequency range, the spectral density decays in a ratio $f^{-5/3}$ with the frequency. This relationship is associated to the balance of produced and dissipated energy and is normally described as the Kolmogorov's inertial range (Kolmogorov [1941]). In case of a normalized spectrum $R_N(z, f)$, the decay is proportional to the normalized expression $f_L^{-3/2}$ being $f_L = f \cdot L^x(z)/\bar{U}(z)$ a non-dimensional frequency being $L^x(z)$ the wave lenght of the turbulence. Figure 1.4 shows different power spectral density functions proposed in the literature as EN 1991-1-4, von Kàrmàn [1948], Davenport [1967] and Harris [1990]. These formula are based on full-scale spectral density functions carried out at different places and heights. For the representation of the Davenport's spectrum, a wave length of $L^x \approx 1200$ m has been chosen. On the other hand, for the spectrum proposed by Harris a value of $L^x \approx 1800$ m has been used. For a non-dimensional frequency of $f_L = 0.3$, the spectrum proposed by Davenport gives the largest spectral values in comparison to the other ones. As explained in Dyrbye u. Hansen [1997], using a value of $A = 0.14$, the straight line satisfies the inertial subrange criterion specified in the Eurocode 1. This range is located between the low frequency range caused by large eddies and the high frequency range, where the energy dissipation occurs due to small eddies. For the majority of structures studied in wind engineering, the spectral information included in the inertial subrange is of prominence importance due to location of most eigenfrequencies of the structures. Strictly speaking, the wave length of the turbulence $L^x(z)$ and the integral length scale $L_u(z)$ are different concepts. In the literatur, depending on the author, the normalized frequency f_L used to describe the spectrum is defined in terms of $L^x(z)$ or $L_u(z)$. In Section 2.3.1, these differences are discussed.

The cross-spectrum $S_{uu}(P_1, P_2, f)$ represents the statistical dependence between the turbulence component u at two points P_1 and P_2 at a given frequency f, as well as the dependence on the spatial dimension of the vortices in the wind field (Dyrbye u. Hansen [1997]). In addition, the normalized cross-spectrum S_N is defined as:

$$S_N = \frac{S_{uu}(P_1, P_2, f)}{\sqrt{S_{uu}(P_1, f) \cdot S_{uu}(P_2, f)}} \tag{1.12}$$

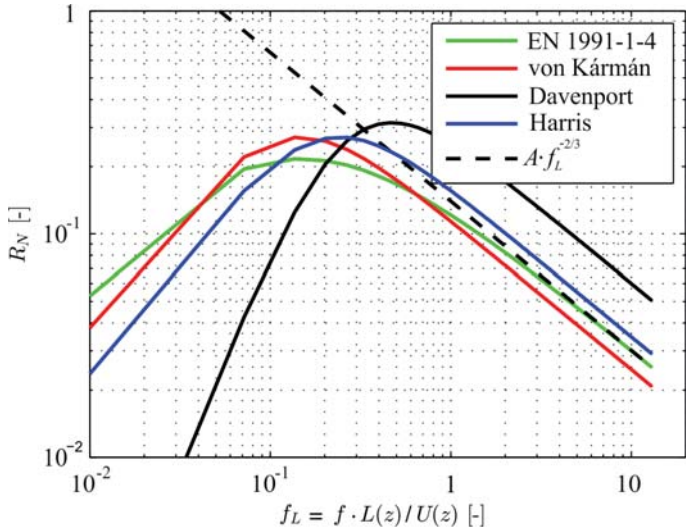

Figure 1.4: Representation of different power spectral density functions

The cross-spectrum S_N is a complex term. The real part is the most important term for the response calculations. However, if the assumption of a zero-phase is made, the argument is identical to the real part allowing the define it with an empirical formula. This function is then known as the coherence function $\gamma_{i,j}(f)$ and was originally proposed by Davenport [1967]:

$$|S_N| = \gamma_{i,j}(f) = exp\left(\frac{-2 \cdot f \cdot \sqrt{(C_x \cdot \Delta_x)^2 + (C_y \cdot \Delta_y)^2 + (C_z \cdot \Delta_z)^2}}{\bar{U}_i + \bar{U}_j}\right) \tag{1.13}$$

where Δ_x, Δ_y and Δ_z are the relative distances in the Cartesian axes x, y and z between points $P_i(x_i, y_i, z_i)$ and $P_j(x_j, y_j, z_j)$. The non-dimensional terms C_x, C_y and C_z are known as decay coefficients and can be experimentally calculated. Typical values given in the literature are $C_x \approx 3$ and $C_y = C_z \approx 11$ (Clobes [2008]). When comparing this coherence formula with eq. 1.9 it becomes evident that there is an inconsistency: for small frequencies, the coherence function tends to unity. That is not true for separations between points of the same order or larger than the integral length scale L, where there is a lack of correlation, even at low frequencies (Dyrbye u. Hansen [1997]). Nevertheless, the coherence function $\gamma_{i,j}(f)$ is widely used in wind engineering due to its simplicity for the calculation of the spectral wind field.

1.2 Wind field in industrial areas

Industrial areas are the natural places where steel chimneys are normally built. Usually, these areas are located outside the cities, where the logistic process is more effective. The chimney provides ventilation for hot smoke, water steam or fluent gas generated during the production process and is an important part of the total costs of an industrial facility. In particular, chimneys are sensitive to wind and seismic actions due to their high slenderness. In the absence of seismical action, the wind is beside ice the only relevant loading case for the structural analysis of chimneys, and its importance increases with the height of the structure.

Figure 1.5: Examples of industrial facilities: Slender chimneys and nearby buildings

Often, as depicted in Figure 1.5, the chimneys are located near an industrial building, which can be considered as significantly higher than the surrounding obstacles. But for design purposes the chimney is usually considered as a single object placed in an homogeneous terrain without consideration of the nearby building. For its design, an undisturbed wind profile over the height as shown in Figure 1.3 is assumed and its application seems to be an incorrect solution: the adjacent power house has a significant influence on the local wind structure and consequently, on the wind load acting on the chimney. This disturbance of the flow may also change the dynamic response of the slender chimney. In wind

engineering, the alteration in the wind structure by an obstacle is known as interference effect.

Many papers are found in the literature concerning the interference effects between high rise buildings or different circular stacks (Khanduri et al. [1998]). But studies about the influence of lower surrounding buildings on the dynamic response of high slender structures are almost non-existent in the literature. Wind tunnel measurements were carried out by Ruscheweyh ([1997] and [1998]) to study the vortex-induced vibrations of a stack in the vicinity of a building. For some wind angles, the wind load can be reduced due to the shadow effect produced by the presence of the building. But for some boundary conditions and critical wind directions, an increase of the local pressure occurs or non-expected aeroelastic effects appear. Figure 1.6 depicts the results presented in Ruscheweyh [1997] showing the relative amplitude k^* of the chimney's tip depending on the wind angle θ. If the chimney is located at the corner of the building, the presence of the nearby building generates vortices inducing an increase of more than 30% of the amplitude k^* for critical wind directions.

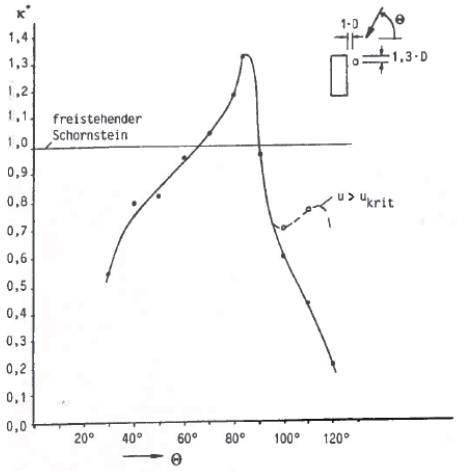

Figure 1.6: Relative amplitude k^* of the chimney's tip for different wind angles (Ruscheweyh [1997])

The above presented interference effect is normally considered as the change produced with respect to the mean wind speed profile presented in Figure 1.3 and characteristic for extreme wind conditions. On the contrary, when the wind is calmed and blows lightly, the mean wind speed profile can diverge in form. According to long-term measurements made

by Telljohann [1998] or Clobes u. a. [2011a], the exponential shape depicted in Figure 1.3 appears only in several occasions associated to the extreme wind conditions.

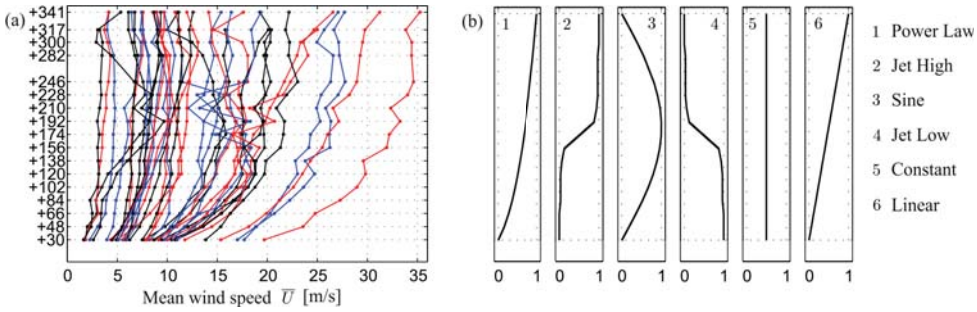

Figure 1.7: (a) Mean wind speed profiles derived from full scale data. (b) Normalized wind profile shapes Clobes u. a. [2011a]

As shown by Willecke [2013], the atmospheric boundary layer can produce many different mean wind speed profile shapes, especially in the presence of low and moderate wind conditions. The Institute of Steel Structures of the Technical University Braunschweig operates a 344 m high guyed mast as measurement center of wind speed, wind direction and temperature. The mast is located in a rural area in northern Germany, which coincides with the description of the ideal place for the construction of an industrial complex with its corresponding steel chimney. An example of this scatter phenomenon is presented in Figure 1.7(a) where few recorded wind profiles are shown to illustrate the large variation of profile shapes. The statistical model developed in his work identifies the presence of six different profile shapes and their normalized forms are given in Figure 1.7(b). An interesting conclusion of their investigation is that the classical power law class of Figure 1.3 has an occurrence frequency of only 55.9 % of the total mean wind speed profile measurements covered during the last 20 years.

1.3 Eurocode EN 1991-1-4 as design tool

The European standard Eurocode EN 1991-1-4 is conceived as a design tool for engineers. It describes the principles and the methodology for calculating design wind actions on structures. The formulas presented there are a combination of theoretical concepts, analytical simplifications and empirical approximations from wind tunnel and/or full scale measurements.

1.3.1 Extreme wind conditions and structural factor

For the calculation of the wind loading on a structure a representative reference wind velocity is introduced. The basic wind velocity U_b is necessary for the mathematical definition of the mean static wind pressure, the mean wind speed and turbulence intensity profiles. According to the European practice, the basic wind velocity can be calculated for a 10-minute time period at 10 m above terrain, regardless of the direction and season and applying a roughness length of $z_0 = 0.05$ m. The basic wind velocity U_b varies between regions being a result of an extreme value analysis of long-term measurements. Furthermore, the annual probability of exceedance of U_b is 2%, which corresponds roughly to a return period of 50 years. Figure 1.8 shows the Spanish and German basic wind velocity maps given in CTE and DIN EN 1991-1-4/NA, respectively. Spain is divided into three different wind zones and Germany into four. The Eurocode uses a modification of eq. 1.3 to define the value of the mean wind speed inside the atmospheric boundary layer up to 200 m above the ground:

$$\bar{U}(z) = c_r(z) \cdot c_0(z) \cdot U_b \tag{1.14}$$

where $c_r(z)$ is the roughness factor and $c_0(z)$ is the orography factor. The latter can be approximated to the unity if a flat terrain is considered.

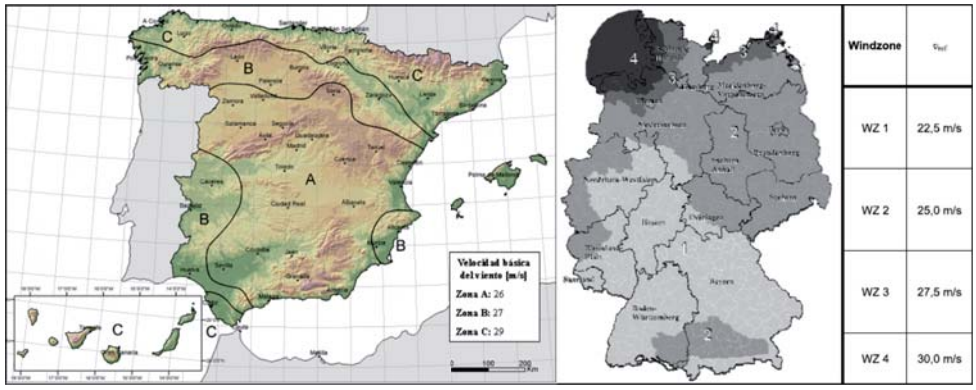

Figure 1.8: Spanish and German basic wind velocity maps

The roughness factor $c_r(z)$ accounts for the variability of the mean wind speed due to the height z above the ground and due to the roughness of the terrain upwind of the place of calculation. The dependence on the height z is given by:

$$\begin{aligned} c_r(z) &= k_r \cdot \ln\left(\frac{z}{z_0}\right) \quad \text{for } z_{min} \leq z \leq 200 \text{ m} \\ c_r(z) &= c_r(z_{min}) \quad \text{for } z \leq z_{min} \end{aligned} \tag{1.15}$$

and the dependence on the terrain roughness is given by the terrain factor k_r:

$$k_r = 0.19 \cdot \left(\frac{z_0}{0.05}\right)^{0.07} \tag{1.16}$$

This factor is defined in proportion to the reference roughness length, which corresponds to a terrain category II ($z_{0,II} = 0.05$ m).

In a similar way, the turbulence intensity $I_u(z)$ at height z is defined as the ratio between the standard deviation of the turbulence σ_u and the mean wind speed $\bar{U}$. The standard deviation can be determined using the following expression:

$$\sigma_u = k_r \cdot k_I \cdot U_b \tag{1.17}$$

where k_I is the turbulence factor. From this expression, it can be deduced that in a conservative way, the standard deviation σ_u is considered in the Eurocode as a constant value above the height z. However, an identical expression is given for the direct calculation of the turbulence intensity I_u above the height z:

$$\begin{aligned} I_u(z) &= \frac{\sigma_u}{\bar{U}(z)} = \frac{k_I}{c_0(z) \cdot \ln\left(\frac{z}{z_0}\right)} \quad \text{for } z_{min} \leq z \leq 200 \text{ m} \\ I_u(z) &= I_u(z_{min}) \quad \text{for } z \leq z_{min} \end{aligned} \tag{1.18}$$

The spatial structure of the wind turbulence is also given in the Eurocode and is based on ESDU 74031. The integral length scale $L_u(z)$ of the wind fluctuation u is defined as follows:

$$\begin{aligned} L_u(z) &= L_t \cdot \left(\frac{z}{z_t}\right)^{\alpha_{L_u}} \quad \text{for } z_{min} \leq z \leq 200 \text{ m} \\ L_u(z) &= L_u(z_{min}) \quad \text{for } z \leq z_{min} \end{aligned} \tag{1.19}$$

with a reference height of $z_t = 200$ m, a reference length scale of $L_t = 300$ m, and an exponent $\alpha_{L_u} = 0.67 + 0.05 \cdot \ln(z_0)$. The value of α_{L_u} increases if the terrain roughness becomes larger and therefore, the value of L_u for a given height z decreases if the terrain roughness increases.

The non-dimensional power-spectral density function $R_N(z, f)$ presented in the Eurocode was proposed by Kaimal u. a. [1972] and it is depicted in Figure 1.4:

$$R_N(z, f) = \frac{f \cdot S_{uu}(z, f)}{\sigma^2(z)} \frac{6.8 \cdot f_L}{(1 + 10.2 \cdot f_L)^{5/3}} \tag{1.20}$$

The structural factor $c_s c_d$ is used for the calculation of the equivalent static wind force in the along-wind direction produced by the gusty wind. The factor represents the combination of the size factor c_s and the dynamic factor c_d. The expression of $c_s c_d$ is given as follows:

$$c_s c_d = \frac{1 + 2 \cdot g_x \cdot I_u(z_s) \cdot \sqrt{Q^2 + R^2}}{1 + 7 \cdot I_u(z_s)} \tag{1.21}$$

where z_s is the reference height for determining the structural factor (in case of chimneys at 60 % of the entire height of the structure) and g_x is the peak factor. The variable Q^2 is known as the background factor, which allows for the lack of full correlation of the pressure and R^2 is the resonance response factor, responsible for the increase of the resonant response with the vibration mode.

1.3.2 Moderate wind conditions

Statistical information about the relative occurrence frequencies of moderate wind speed is necessary for the calculation of the fatigue life prognosis of structures. In wind engineering, for the determination of the occurrence probability of different wind speeds, the Weibull distribution is commonly used. This distribution is characterized by two parameters: the

shape parameter k and the scale parameter A. The Weibull probability density function $p(\bar{U})$ is given as:

$$p(\bar{U}) = k \cdot \frac{\bar{U}^{k-1}}{A^k} \cdot \exp\left(-\left(\frac{\bar{U}}{A}\right)\right)^k \tag{1.22}$$

The fitting process of the mean wind speed $\bar{U}$ to a Weibull distribution is a result of long-term wind speed measurements. The values of A and k depend on several factors and vary if different sites are considered. In the case of Europe, information about the scale and shape parameters can be directly obtained from the European Wind Atlas according to Troen u. Petersen [1979].

Even if a fatigue analysis is not explicitly demanded in the Eurocode, the risk of fatigue problems should be kept in mind, especially if a slender structure is considered. No explicit information about a statistical distribution of the mean wind speed is presented. However, from the information to calculate the number of load cycles caused by vortex excitation, a Weibull distribution can be decrypted. It is defined using a shape factor of $k = 2$ and a scale factor of $A(z) = \bar{U}(z)/5$ (Clobes u. a. [2011b]).

1.4 Lacks of information on Eurocode EN 1991-1-4

If an industrial chimney is to be designed using the Eurocode 1 or an equivalent standard, certain doubts could appear during the design process. The problem introduced above concerning the interference effect due to the presence of neighbouring structures is barely taken into account in the European standard. Annex A.4 presents some simple formulas for the design of the nearby structures, which can be affected by the detour of the high speeds down to ground level due the presence of a building. The solution to this problem lies in the increase of the reference height z_n for the calculation of the peak velocity pressure $q_p(z_n)$ acting on the neighbouring buildings, i.e. the design of the adjacent buildings is adjusted due to the presence of a high structure, but the opposite influence is not considered. The interference effect is also taken into account in terms of its influence on the aeroelastic instability known as galloping. To avoid the occurrence of the interference galloping between large cylinders, the Eurocode 1 gives in Annex E.3 an easy methodology to obtain the critical wind velocity v_{CIG} in which the galloping appears. The basic formula depends mainly on geometrical parameters, but is only applicable for chimneys or stacks with the same diameter and height. No consideration about the interference effect is provided in the code if a slender chimney is located nearby a huge building as shown in Figure 1.5. Due to this lack of information for framing the rule for other structural shapes and heights, wind tunnel measurements need to be carried out. This expensive solution

was also proposed by Stathopoulos [1984] due to its difficulty to asses it analytically. As output from the tests, special warnings of possible adverse situations in building codes were given.

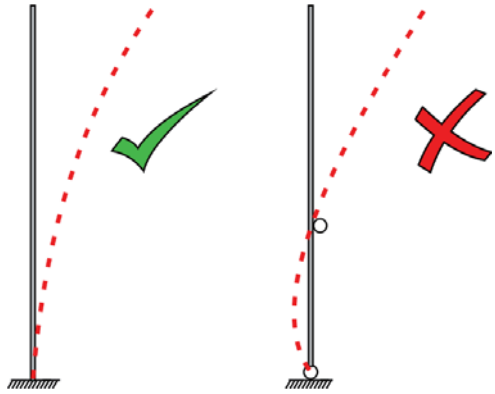

Figure 1.9: Eigenmodes of a cantilevered chimney (a) and a chimney with a propped connection (b) (Clobes u. a. [2012a])

Another serious drawback appears if the chimney is connected to the power plant. Usually, when the chimney is located in the proximity of the building, the designers decide to use it as an additional support for the chimney. This fact reduces the slenderness of the cantilevered structure reducing the dynamic gust response of the chimney and obtaining a financial advantage.

Figure 1.9 schematically shows the change of the static system due to the connection of the chimney at the building's roof. The structural system changes from a cantilevered chimney (left) to a propped one (right). The design of this type of static system using the Eurocode procedure is problematic in formal terms: the regulatory procedures for the calculation of the structural factor $c_s c_d$ is only applicable, if the first mode shape of the chimney has a constant sign. Therefore, the Eurocode cannot be used to calculate propped chimneys with a mode shape as shown in Figure 1.9(b). This principle was originally formulated by Solari [1982] who is the main author of the procedure to estimate the dynamic response of a structure under wind buffeting in the along-wind direction presented in the Eurocode.

The interference effect is a complex problem due the large number of variables involved. The shape, height and relative position of the building, roughness of the terrain and the structure's surface or the wind direction play an important role in the wind load modification mechanism, and therefore, a parametric approach is always necessary to study this phenomenon.

Although the Eurocode gives no guidance on the susceptibility of the structures to fatigue produced by wind buffeting, its effects must be assessed. Due to the time-dependent and stochastic nature of the wind, industrial chimneys are continuously exposed to varying stress amplitudes. The stresses depend on the wind characteristics and the structural properties of the chimney. Generally, the fatigue of chimneys is related to the vortex-induced vibrations characterized by critical velocities of appearance. In case of wind buffeting, the fatigue is also problematic because it acts on every wind speed range. From an analytical point of view, the fatigue problem can be studied using probability distributions of the wind speed, power spectral density functions and of the mechanical characteristics of the structure. This information leads to the calculation of a series of load cycles that allow for the damage prognosis of the structure. The Eurocode proposes in Annex B a method to estimate the number of times N_G that a load level ΔS is reached or exceeded during a period of 50 years. ΔS is expressed as a percentage of a maximal effect S_k (displacement, acceleration, bending moment etc.) on the structure due to a 50 years return period wind action.

$$\frac{\Delta S}{S_k} = 0.7 \cdot \log^2(N_G) - 17.4 \cdot \log(N_G) + 100 \tag{1.23}$$

The origin of eq. 1.23 is absolutely diffuse. From the literature review, the mathematical background of the curve is directly related to the mathematical method proposed by Davenport [1966]. As reasoned by Aizpurua-Aldasoro u. Clobes [2013], the formulation of the problem is not only vague in the definition itself but also in the conditions in which the corresponding expression can be used. Interestingly, no specifications about the site-dependent wind parameters and/or structural characteristics are necessary to apply the formula. And it does not take into account the possibility of occurrence of the different profile shapes in case of moderate winds. As explained by Kemper [2013], when carrying out numerical simulations on linear structures, the influences of several parameters like the site-dependent wind characteristics, fundamental frequency and damping are decisive on the fatigue life of the structure.

1.5 Scope of the study

During the last years, the Institute of Steel Structures of the Technische Universität Braunschweig has been involved in research projects to improve the actual design procedures on wind buffeting of industrial chimneys. This work summarizes these last efforts. Under consideration of the problems presented above, the new approach will cover the interference effect produced by the nearby buildings, the static configuration of the struc-

ture and the influence on the fatigue life prognosis of the industrial chimney if long-term wind profile statistics are considered. Each of these main issues has to be solved step by step.

The interference effect will be studied using the boundary layer wind tunnel (BLWT) of the Institute of Steel Structures. Wind tunnel tests will be carried out to measure the change on the wind profiles and turbulence spectra due to the presence of a large nearby building. The study will cover different power house shapes, different positions of the chimney with respect to the building and varying wind directions. For an engineering application, an analytical representation of the disturbed mean wind speed profile $\bar{U}_d(z)$ has to be defined.

Numerical simulations on the dynamic response of an industrial chimney will be performed to study the real influence of the interference effect. The inputs used for the simulation should be those obtained from the wind tunnel measurements. In order to study the frequency-dependent relation between wind turbulence and wind force, the aerodynamic admittance function $|\chi(f)|^2$ has to be experimentally identified. Using a carbon fiber model of an industrial chimney, and considering the Reynolds number effect, the forces and bending moments acting on the chimney should be measured under interference wind conditions using the high frequency force balance (HFFB).

Using the analytical representation of the new mean wind speed profile $\bar{U}_d(z)$ and the spectral information measured in the wind tunnel tests, the wind field is fully described. Therefore, a new approach for the calculation of the peak response of a chimney $\hat{X}_d$ under disturbed flow conditions will be deduced. For this, the mathematical background of the gust response factor must be studied to introduce the interference effect and if necessary, the propped static system.

Regarding the fatigue life prognosis of industrial chimneys under gust buffeting, the long-term wind profile statistics obtained at the Gartow II mast will be used to propose a refined method compared to the approach given in the Eurocode EN 1991-1-4. In previous works by Clobes u. a. [2011a] and Willecke [2013], a new wind field for low, moderate and high speed conditions was statistically described. These works were focused on the vortex-induced vibrations, which depend on critical wind speeds and for which the fluctuating component is not described as precisely for a buffeting approach. Since the model for the turbulence intensity presented in Willecke [2013] is a rough approximation of the standard deviation of the wind fluctuations $\sigma_u(z)$, a refined analysis of this variable has to be carried out. A correct definition of $\sigma_u(z)$ is fundamental for the fatigue analysis for buffeting due to its high importance on the stochastic nature of the loads acting on the structure.

To analyse the influence of the different wind profile classes on the response of the chimney, a Monte-Carlo simulation will be used. The buffeting responses of the chimney can be calculated in the frequency domain linking this output to the approach of Dirlik Dirlik [1985]. This methodology is widely used in industrial processes and it is helpful to calculate the probability density function of the rainflow-ranges. With this results, it is possible to define a fatigue life prognosis of a real industrial steel chimney under realistic wind conditions.

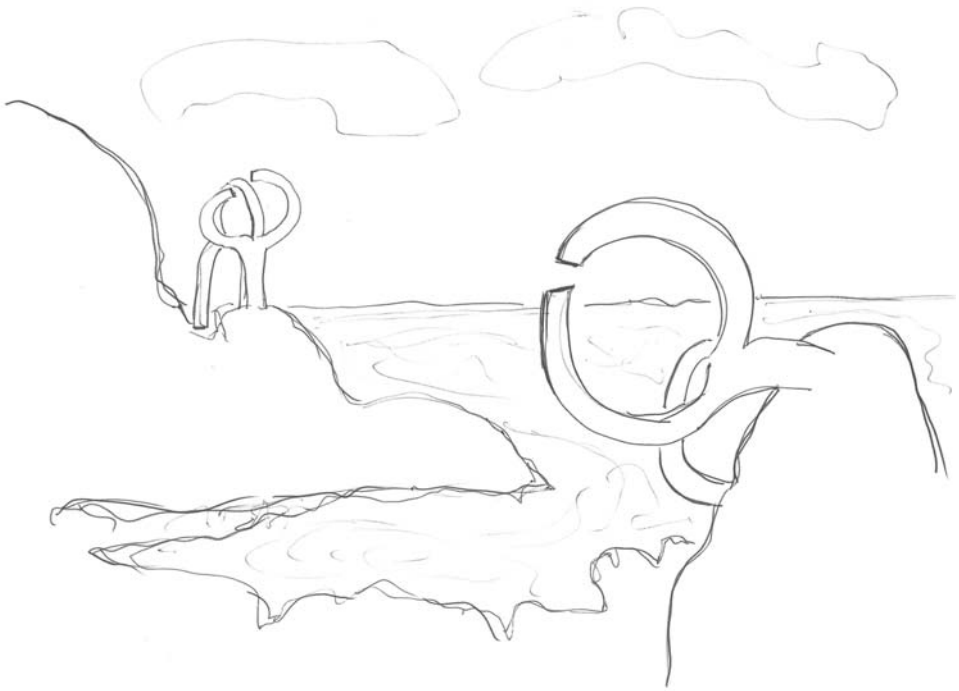

Eduardo Chillida. "Windkamm". San Sebastian

2 Wind structure under interference conditions

As explained in the introduction, the current standards are not always applicable for the determination of the wind loads acting on structures. For example, some design buildings with filigree geometry can not be compared with the basic geometries given by the standards and for this reason, wind tunnel experiments are a useful tool for the safe determination of aerodynamic forces or instabilities acting on such kind of structures.

In this chapter, an introduction to the boundary layer wind tunnel (BLWT) of the Institute of Steel Structures of the TU Braunschweig is given. After simulation of the atmospheric boundary layer inside the wind tunnel, the wind acting on an industrial chimney was measured using a multi-hole pressure sensor. The wind structure has been measured for undisturbed and disturbed wind conditions. For the latter, power house models are introduced in the wind tunnel. Wind speed and turbulence spectra are measured over the height for different building shapes and chimney positions. Finally, a correction of the mean wind speed profile $\bar{U}(z)$ will be presented depending on the shape of the building, position of the chimney regarding the adjacent building and wind direction.

2.1 BLWT of the Institute of Steel Structures of the TU Braunschweig

The Institute of Steel Structures of the TU Braunschweig operates since 2010 a boundary layer wind tunnel (BLWT) for building aerodynamics. The BLWT is an open suction Eiffel type one. The total length of the wind tunnel including the fan is 12.85 m. Its working section is approximately 8 m long and 1.4 m wide and has an adjustable height ranging from 1.2 to 1.5 m. The ceiling is adjustable from the entrance up to the end. The wind velocity inside the tunnel is controlled externally by the user. A 55 kW blower accelerates the flow up to a maximal wins speed of 25 m/s. A turntable with a diameter of 1.2 m is used to study the wind effects from all wind directions rotating the model.

Figure 2.1 shows a schematic view of the BLWT. The wind tunnel contains two test sections. The test section 1, located at the entrance of the working section, is usually used

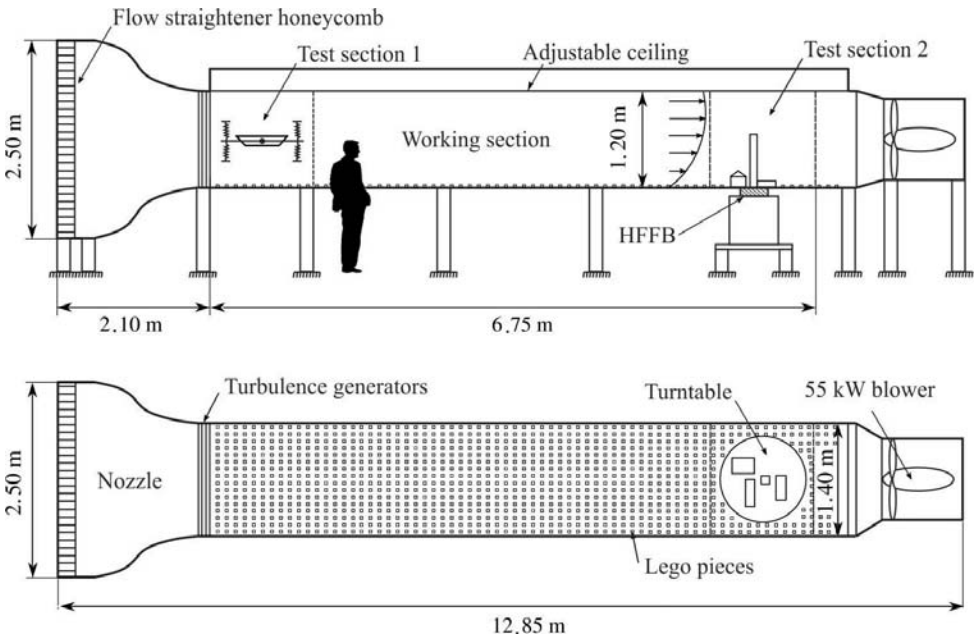

Figure 2.1: Schematic view of the wind tunnel

for experiments characterized by low turbulence specifications or aeroelastic experiments on sectional models. On the other hand, it is sometimes necessary to determine the wind loads or wind flow acting over the whole structure model. For this purpose, the simulation of an atmospheric boundary layer is necessary. These kind of tests are carried out at the end of the working section, which is assigned as test section 2 in Figure 2.1. The addition of passive devices, such as Lego pieces along the working section makes possible to simulate an atmospheric boundary layer at the test section 2. That requires a working section length in the range of 15 to 30 m (Cermak [1958]). But in this case, due to the relatively short working section, additional grids or turbulence generators are installed as boundary layer augmentation devices (ASCE [1999]). Despite the large number of proposals given in the literature for the determination of the turbulence generators and roughness elements as Counihan [1969], Standen [1972] and Irwin [1981], none of the published configurations could be successfully implemented. Therefore, own developments have offered the best results.

2.2 Measurement techniques

2.2.1 TFI Cobra Probe

The turbulent wind flow is measured using the TFI Cobra Probe depicted in Figure 2.2. This is a multi-hole pressure probe that provides dynamic, 3D components of the wind velocity and local static pressure measured with a high time resolution of up to 2,000 Hz. Due to its high sampling rate, the device is suitable to measure turbulent flow fields. The Cobra Probe is around 160 mm in length, with a body diameter of 14 mm and a faceted head with a width of 2.6 mm. Four small pressure taps are located on the head of the device, and are responsible for the collection of the pressure field acting on the Cobra. This device is often referenced in the literature for the measurement of the wind field inside wind tunnels, as in Eaddy u. Melbourne [2011].

Figure 2.2: TFI Cobra Probe

The raw data measured by the TFI is provided by 4 analogue voltage signals, which are firstly amplified and then sampled by an A/D-converter NI PXI DAQ with a sampling frequency of 1,200 Hz. The digitalized discrete signal is processed in a Matlab-routine to compute the three-dimensional wind speed vector and the dynamic pressure.

2.2.2 High frequency force balance

The high frequency force balance technique (HFFB) can be used to measure directly the wind load on a structure. For this purpose, a stiff and lightweight geometric representation of the building must be connected to the force balance. A high stiffness of the balance is a *sine qua non* condition for a successful application of this technique. Although high sensitivity and rigidity can be interpreted as opposite concepts, the piezo-transducers provide an excellent compromise. The measurement problem lies in the fact that the balance-system and model eigenfrequencies must be well above the range of frequencies of interest for the simulated building response. Therefore, measuring wind forces it is

necessary to ensure that this technique is not prone to resonance and to prevent it from acting as an accelerometer (Cook [1983]).

Figure 2.3 shows the HFFB installed in the wind tunnel. It consists of four force link elements Kistler Type 9317B6 built as four table legs. Each sensor measures the dynamic or quasi-static wind forces in the three orthogonal components. The obtained forces allow for the calculation of the shear forces as well as torsional and bending moments produced by the wind load on the connected model. This device has an ultra-sensitive accuracy (about 0.01 N resolution), as well as a high force range up to 1 kN in X and Y direction and 2 kN in Z. The operation of the sensors is based on the transformation of the yielded charge signal provided by the piezo-sensors into voltage. Due to the low signal produced by the piezo elements, charge amplifiers are needed to transform the charge signal into a voltage proportional to the force. Although the 3-component transducers give twelve individual charge signals, six charge amplifiers Kistler Type 5015A are installed. Comparing piezo and strain gauges balances, the former are more expensive because of the advanced electronics of the charge amplifiers, but for dynamic measurements, the piezo-system is the most advanced choice in the market to measure forces in wind tunnel experiments (Schewe [1990]).

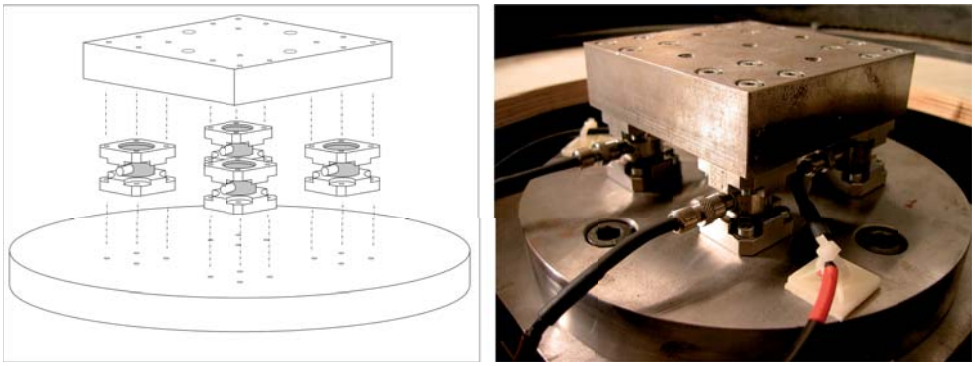

Figure 2.3: High frequency force balance

The substructure is made of steel and weights 800 kg. As Figure 2.4 shows, it follows a cylindrical form allowing the rotation around the axes of the balance. To isolate external vibrations produced by the blower or other sources, four Bilz type BiAir springs are installed under the steel structure. The active isolation provided by the springs creates optimal conditions for a proper use of the HFFB technique, thus avoiding a rigid connection to ground and, consequently, to the wind tunnel. The four sensors have a high

natural frequency of about 5 kHz in X and Y direction and 21 kHz in Z direction. The left part of Figure 2.4 shows the transfer function of the whole system, including balance and substructure. For the calculation of the function an impact hammer testing has been carried out. The sensors of the balance have been considered as output signals in the modal analysis. The test concluded that no dynamic amplification can be observed up to 400 Hz.

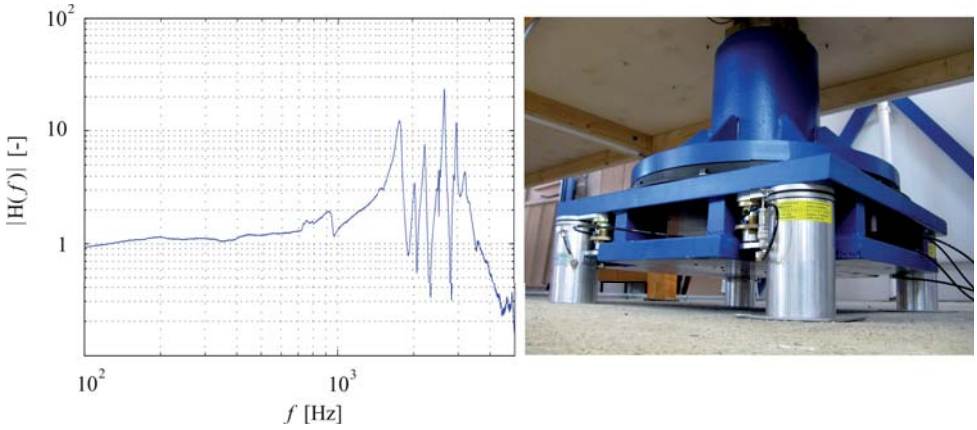

Figure 2.4: Transfer function of the balance and substructure

The use of piezoelectric transducers needs much attention, because the electrical signal drifts with time and, therefore, quasi-static loads, can only be measured with careful consideration. The drift can be easily corrected due to its linear behaviour if the following data acquisition procedure is applied (Clobes u. a. [2012a]):

i. Starting the data acquisition (measurements of zero values without wind).

ii. Switching-on of the wind tunnel.

iii. Measuring the wind load in the stationary state.

iv. Switching-off of the wind tunnel.

v. Stopping the data acquisition (measurement of zero values without wind).

vi. Calculation of the slope of the linear drift of the two measurements of the zero values.

Many tests have shown the extreme sensitivity of the piezo-sensors to temperature changes. If the surface of the sensors is touched with the tip of the fingers before the measurement

begins, an incorrigible exponential drift appears. For this reason, a supplementary temperature isolation is installed around the substructure.

In conclusion, accordign to Cermak [2003], the major benefits derived from the HFFB technique can be summarized as follows:

- Statistics of overall wind loads became accessible.
- Quick and low cost tests compared to aeroelastic experiments.
- For a given building geometry only one test is necessary to determine the dynamic response.
- The aerodynamic admittance function can be acquired.
- Critical wind directions can be identified.
- Findings can be used to determine the need for aeroelastic tests.

Although the balance produces 12 signals simultaneously, only six charge amplifiers are in use. To solve this inconvenience, some electrical connections are made unifing the X and Y force components of sensors. The following forces according to Figure 2.5 can be measured:

$$F_{x1+x3} \qquad F_{x2+x4} \qquad F_{y1+y2} \qquad F_{y3+y4} \qquad F_{z1} \qquad F_{z2} \qquad F_{z3} \qquad F_{z4} \tag{2.1}$$

Starting from these separated forces, the total forces and moments can be obtained in real time applying the following expressions:

$$\begin{aligned}
F_x &= F_{x1+x3} + F_{x2+x4} \\
F_y &= F_{y1+y2} + F_{y3+y4} \\
F_z &= F_{z1} + F_{z2} + F_{z3} + F_{z4} \\
M_x &= a \cdot (-F_{z1} + F_{z2} - F_{z3} + F_{z4}) \\
M_y &= a \cdot (-F_{z1} - F_{z2} + F_{z3} + F_{z4}) \\
M_z &= a \cdot (F_{x1+x3} - F_{x2+x4} + F_{y1+y2} - F_{y3+y4})
\end{aligned} \tag{2.2}$$

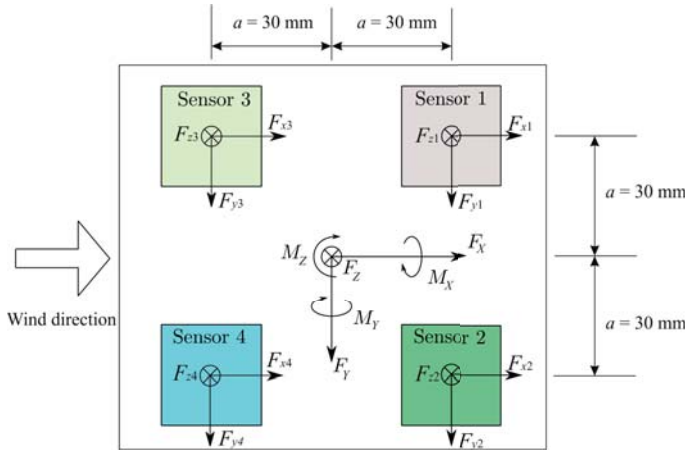

Figure 2.5: Schematic view of the force distribution between sensors

A large number of experiments has been carried out using the high frequency force balance. All information about these experiments are comprehensively explained in Chapter 4.

2.3 Simulation of interference effects

In this section, the results of wind tunnel experiments for the determination of the influence of the interference on the wind field are presented. To perform efficient tests, the simulation of a full atmospheric boundary layer matching the target wind field is needed. Mean wind speed, turbulence intensity, integral length scale and wind spectrum should be assessed in the first place. After a successful completion of these conditions, interference effects are simulated. For this purpose, scale models of industrial buildings are introduced in the wind tunnel. The disturbed wind field has been measured at the position where a nearby industrial chimney is supposed to be. Simulations have been carried out considering two different power house shapes (cubic and rectangular), two different positions of the chimney with respect to the building and varying wind directions. The reference wind speed inside the wind tunnel during the tests is 12 m/s.

2.3.1 Non disturbed wind conditions

A terrain category II according to the German National Annex DIN EN 1991-1-4/NA has been simulated considering the typical areas where industrial chimneys are built. As

in Table 1.1, the German document defines TC II as an area with low vegetation, such as grass, and isolated structures characterized by a roughness length of $z_0 = 0.05$ m. Therefore, industrial areas in open country exposure correspond to this definition.

In order to correctly simulate the desired boundary layer, some calibration tests have been carried out, varying the sequence of the roughness elements along the working section and spires. The best results have been obtained using the configuration shown in Figure 2.6. The turbulence generators are built with a low fence barrier combined with pentagons, triangles and vertical bars. The material of the spires is wood, while the roughness elements are commercial Lego pieces.

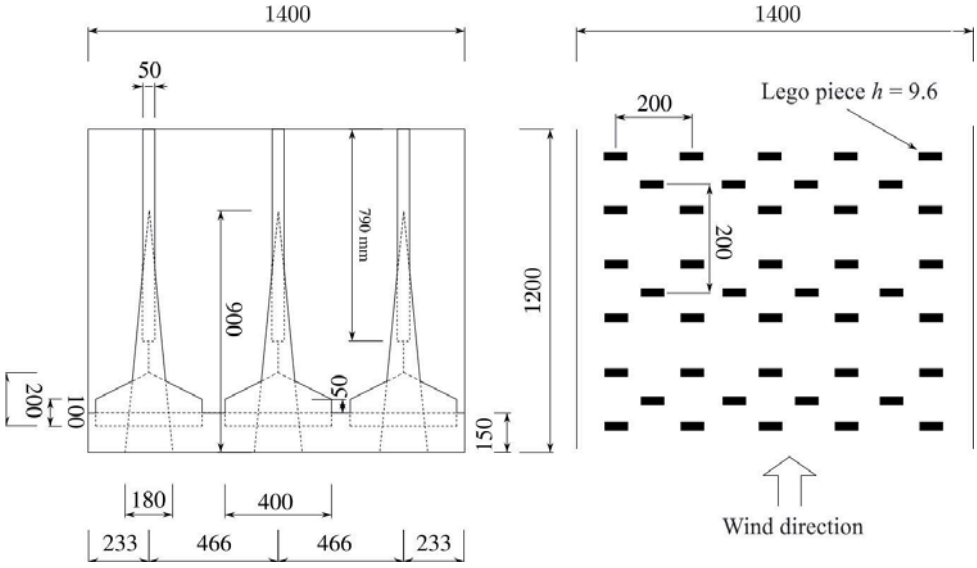

Figure 2.6: Turbulence generators and roughness elements [mm]

Figure 2.7 depicts the profiles of the mean wind speed, the turbulence intensity and the integral length scale. A 1:300 geometric scale λ_L is selected for the wind tunnel simulations, taking into account the problematic of the blockage ratio. The velocity scale λ_U, which is defined as the ratio of the basic wind speed in natural winds at $z = 10$m and the wind speed produced in the wind tunnel at $z = 10/\lambda_L$, is about 1:3. Therefore, the time scale λ_T, which is defined as $\lambda_T = \lambda_L/\lambda_U$, has a value of about 1:100. These scale values are within the range proposed in Davenport [2007] as ideal scale values for the simulation of building aerodynamics in wind tunnels.

The blue dots on Figure 2.7 represent the data measured in the wind tunnel at the test section 2 along the height. The blue lines of the mean wind speed and turbulence intensity represent the measured data following the exponential law and $z_{ref} = 10$ m. Regarding the mean wind speed profile, the blue line is approximated using an exponent coefficient of $\alpha_{\bar{U}} = 0.14$. For the turbulence intensity, an exponent coefficient of $\alpha_{I_u} = -0.31$ has been used. The shaded areas represent the limits given for the same terrain category defined by the German wind association WtG. Contrary to the standards, this rule proposes an interval of $\alpha_{\bar{U}}$ and α_{I_u} suitable for each terrain category. At higher heights, a lower turbulence intensity as compared to the standard is to observed in wind tunnel experiments, but its influence can be neglected (Kopp [2012]).

The selection of the scale cannot always be predefined. The profile of the mean speed $\bar{U}(z)$ is the easiest variable to be adjusted in a wind tunnel, while the integral length scale L_u, associated with the quality of the gusts, is more difficult to be fulfilled due to its scatter along the height and due to the different methods used for its calculation. Experienced voices in wind tunnel techniques advice that the correct scale is reached if the turbulence intensity I_u at the top of the model coincides with the expected value in full scale. In the current work, a 50 cm height chimney model (150 m in full scale) will be tested in the wind tunnel. According to Figure 2.7(b), the blue dot at this height (and below) is in good concordance with the turbulence intensity I_u given in the Eurocode and WtG. Consequently, the geometrical scale of 1:300 seems to be a correct choice.

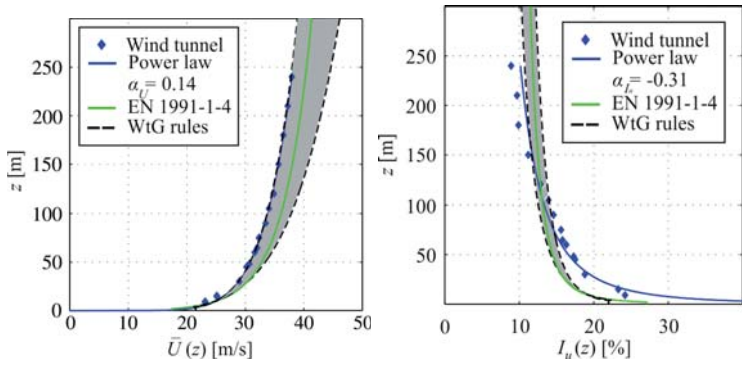

(a) mean wind speed profile $\bar{U}(z)$ (b) turbulence intensity $I_u(z)$

Figure 2.7: Simulated profiles in the wind tunnel

The spatial structure of the simulated wind turbulence is associated with the integral length scale L_u and turbulence spectra S_{uu}. In the case of wind buffeting simulations, these parameters are very important due to their relation with the turbulent process and

frequency scale. Therefore, they have to be correctly fulfilled. Due to the utilization of a unique TFI Cobra device, it was not possible to calculate L_u according to eq. 1.9. Nevertheless, considering the Taylor hypothesis presented in eq. 1.10, the integral length scale can be easily obtained from the integral time scale T_u obtained from the autocorrelation function of the time series at a unique point. According to Clobes [2008], T_u can be determined using for example the following techniques:

- Integration of the autocorrelation function $\rho_{uu}^{T}(\tau)$ up to first zero-cross point.
- Approximation of $\rho_{uu}^{T}(\tau)$ to an exponential curve and its integration.
- Approximation of the measured turbulence spectra S_{uu} to a parametric function having T_u as a free parameter.

On the other hand, the one-sided turbulence spectrum of the wind fluctuations S_{uu} is obtained by a Fast Fourier Transformation FFT of the fluctuating wind velocity part $u(t)$:

$$S_{uu}(z,f) = 2 \cdot \left(\lim_{T \to \infty} \frac{1}{T} \cdot \mathcal{F}^{*}(u(z,t)) \cdot \mathcal{F}(u(z,t)) \right) \equiv 4 \cdot \int_{0}^{\infty} R_{uu}(\tau) \cdot e^{(-i2\pi f \tau)} d\tau \quad (2.3)$$

Schrader [1994] compares different methodologies to determine integral time scales T_u from wind tunnel measurements, as well as from numerical simulations. As conclusion, he recommends the use of the multi variable Fichtl-McVehil spectrum, fitting it to the measured turbulence spectrum S_{uu}:

$$\frac{f \cdot S_{uu}}{\sigma_u^2} = \frac{a \cdot \left(\frac{f}{f_m}\right)}{\left(1 + 1.5 \left(\frac{f}{f_m}\right)^{r}\right)^{\left(\frac{5}{3 \cdot r}\right)}} \quad (2.4)$$

where r controls the crest of the spectrum and f_m the position of the maxima (Niemann [1997]). The constant a is defined as follows (Solari [1987]):

$$a = \frac{1.5^{1/r} \cdot r \cdot \Gamma\left(\frac{5}{3 \cdot r}\right)}{\Gamma\left(\frac{2}{3 \cdot r}\right) \cdot \Gamma\left(\frac{1}{r}\right)} \quad (2.5)$$

Keeping in mind the following relationship between spectrum S_{uu} and integral time scale T_u (Clobes [2008]):

$$\lim_{f \to 0} S_{uu}(f) = 4 \cdot \int_0^{\infty} \rho_{uu}^{T}(\tau) d\tau = 4 \cdot T_u \cdot \sigma_u^2 \tag{2.6}$$

then:

$$T_u = \lim_{f \to 0} \frac{S_{uu}(f)}{4 \cdot \sigma_u^2} \tag{2.7}$$

The integral time scale T_u can be obtained as follows if the measured $S_{uu}(f)$ is approximated by eq. 2.4:

$$f_m = \frac{a}{4 \cdot T_u} \tag{2.8}$$

The parameter r is of special interest. As stated by Niemann [1997], eq. 2.4 coincides with the spectrum of von Kàrmàn if $r = 2$ and with Kaimal, which is implemented in the Eurocode, if $r = 1$. The results given by Fichtl-McVehil show a $r = 0.845$, while the results presented by Schrader from wind tunnel simulations provide a parameter r between 0.5 and 0.9. Figure 2.8(a) shows the approximation of the turbulence spectra at $z = 30$ cm together with the spectrum proposed by Fichtl u. McVehil [1970]. The latter is approximated using a r variable of 1.08. The spectrum is plotted up to 2 Hz in full scale (200 Hz in the wind tunnel) covering the main range of frequencies associated with building aerodynamics and clearly above the Nyquist frequency.

The normalized spectra of the longitudinal turbulence are presented in Figure 2.8(b). In order to facilitate an analytical representation of the measured data, the set of spectra have been approximated to the following six-coefficient expression using Matlab:

$$\frac{f \cdot S_{uu}(z, f)}{\sigma_u^2} = \frac{c_1 \cdot f_L(z)^{c_2}}{(c_3 + c_4 \cdot f_L(z)^{c_5})^{c_6}} \tag{2.9}$$

where f_L is the normalized frequency defined as:

$$f_L(z) = f \cdot \frac{L_u(z)}{\bar{U}(z)} \tag{2.10}$$

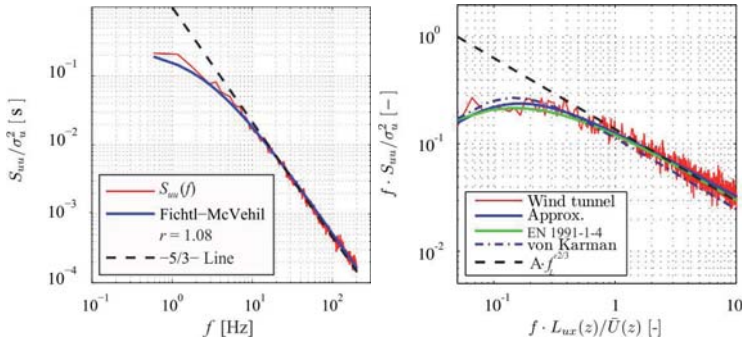

(a) Approximation using Fichtel-MecVehil spectrum

(b) Normalized spectrum

Figure 2.8: Approximation of $S_{uu}(f)$ at $z = 90$ m

The results show a better equivalence of the measured spectrum to the spectrum according to Eurocode as to the spectrum of von Kàrmàn. The selected integral scale L_u for the normalization of the spectrum of Figure 2.8(b) has been obtained from an integral time scale T_u calculated after integration of its exponential approximation.

Figure 2.9 shows the comparison of the L_u values calculated from the wind tunnel tests applying different methodologies. In addition, the results are compared with field measurements, as well as with curves proposed in the literature or standards. The blue dots represent the results associated with the calculation of the integral time scale T_u integrating an exponential function approximated to the real autocorrelation function. The green dots are obtained fitting the measured spectra to the Fichtl-McVehil spectrum. In this case, the measured spectra have been approximated to the spectrum of von Kàrmàn. The red dots have been obtained after approximation of the measured spectrum to the Kaimal u. a. [1972] spectrum. The black dots have been calculated fitting the measured spectrum without restraints in the variable r. Here, the results of wind tunnel tests have shown that the r parameter varies along the height. For example, at $z = 3$ cm its value is $r = 0.77$ and at 70 cm increases up to $r = 1.64$.

Regarding the field measurements, two different sources are plotted in Figure 2.9. Clobes [2008] provided more than 600 results of integral length scales calculated at the telecommunication mast Gartow. The results are concentrated on two different heights, 66 m and 102 m. The measured spectra have been approximated to a Fichtl-McVehil spectrum with $r = 2$ due to the good agreement between the field measurements and the spectrum of von Kàrmàn. The results cover wind speeds between 4 and 21 m/s, clearly under the extreme wind situations given in the codes. It can be observed that the variabil-

ity of the results increases with increasing height, confirming the large scatter observed in the literature. Duchene-Marullaz [1975] presents results of integral length scales from field measurements carried out in the outskirts of a city. For a height of 60 meters, the nominal value of $L_u = 190$ m shows variations between 120 m $< L_u <$ 290 m.

The German National Annex DIN EN 1991-1-4/NA proposes a power law profile similar to eq. 1.19. In this case, the profile is defined up to 300 m high and the exponent, the reference value and the reference height change:

$$L_u(z) = 300 \cdot \left(\frac{z}{300}\right)^{\epsilon} \tag{2.11}$$

where the exponent ϵ depends on the roughness length z_0. Niemann [1992] cited a proposal of L_u used in the draft of the European standard CEN 1. This expression depends on the basic wind velocity U_b at 10 m high, as well as the exponent $\alpha_{\bar{U}}$ from the power law expression of eq. 1.4:

$$L_u(z) = 2.49 \cdot U_b \cdot (z/10)^{(0.2+\alpha_{\bar{U}})} \tag{2.12}$$

Simiu u. Scanlan [1985] noted that the value of L_u depends significantly upon the length and the degree of stationarity of the record being analysed. For example, at $z = 150$ m variations of the integral scale from $L_u = 120$ m up to $L_u = 630$ m can be observed. They used the empirical expression derived by Counihan [1975] to represent the variation of $L_u(z)$ along the height:

$$L_u(z) = C \cdot z^m \tag{2.13}$$

where C and m are parameters that depend on the roughness length z_0. The International Standard ISO 4354:2009 defines a unique formula for the determination of the integral length scale without consideration of the terrain roughness or other parameters:

$$L_u(z) = 100 \cdot \left(\frac{z}{30}\right)^{0.5} \tag{2.14}$$

The German wind association WtG also proposes a power law expression for the integral length scale:

$$L_u(z) = L_{ref} \cdot \left(\frac{z}{z_{ref}}\right)^{\alpha} \tag{2.15}$$

In this case, for a same terrain category, a maximum and minimum value of L_{ref} and α are given. Consequently, the large scatter observed in $L_u(z)$ can be limited. ESDU 75001 proposes an equation for L_u based on the field observations made by Harris [1970] and Duchene-Marullaz [1975]:

$$L_u(z) = 25 \cdot \frac{z^{0.35}}{z_0^{0.063}} \tag{2.16}$$

ESDU 85020 updates the old document ESDU 74031 and adds an analytical derivation of the wave length L^x. This variable is conceptually different to the integral length scale L_u presented above, but is often used in the representation of spectral densities. The wave length is used in the normalization of the frequency axis f_L for the representation of the von von Kàrmàn [1948] spectrum or Davenport [1967] spectrum ($L^x = 1200$ m) and can be theoretically determined. Starting from Kolmogorov's spectral model, ESDU derives a mathematical model of L^x up to 300 m from a spectral density which is dependent only on the mean wind speed profile parameters:

$$L^x = \frac{A^{3/2} \cdot (\sigma_u/u_*)^3 \cdot z}{2.5 \cdot K_z^{3/2} \cdot (1 - z/h)^2 \cdot (1 + 5.75 \cdot z/h)} \tag{2.17}$$

where A and K_z are defined as follows:

$$A = 0.115 \cdot \left[1 + 0.315 \cdot (1 - z/h)^6\right]^{2/3} \tag{2.18}$$

$$K_z = 0.19 - (0.19 - K_0) \cdot \exp[-B \cdot (z/h)^N] \tag{2.19}$$

where K_0, B and N depend on the friction velocity u_*, terrain roughness z_0 and Coriolis parameter f_c. The heights h and z are the boundary layer height and above zero plane height respectively. The Kolmogorov parameter K_z has been fitted with the results provided by field measurements to produce height-dependent integral length scale values. The relationship of eq. 2.17 takes into account the influence of the roughness length z_0 on the size of the eddies at low heights, as well as the theory that at larger heights above ground, the size of the eddies depends on the depth of the planetary boundary layer.

Harris [1970] proposes an expression of L_u obtained applying the homogeneous-isotropic-theory on Davenport's spectrum. The formula is defined for a constant wave length $L^x = 1800$ m along the height z:

$$L_u(z) = 0.084 \cdot L^x \cdot \frac{\bar{U}(z)}{\bar{U}(10)} \tag{2.20}$$

According to the theory of turbulence, the main energy component of a flow is associated with the biggest eddy and, theoretically, the relationship $L_u = L^x$ should be fulfilled Maier-Erbacher u. Plate [1988]. The results provided by Teunissen [1979] and Schroers u. Zilch [1981] have shown that in reality, a relationship of $L^x/L_u \cong 3.1$ is observed. As reasoned by Maier-Erbacher u. Plate [1988], the main energy component does not correspond to the eddy size obtained by the integral length scale according to eq. 1.10. Assuming the Taylor-Hypothesis, the turbulent eddies are transported with the mean wind speed $\bar{U}$, but with inclusion of fluctuating movements, the eddies are deformed and subjected to momentum exchanges. Consequently, the application of eq. 1.10 does not cover only the eddies with the main energy component, but rather the influence of adjacent smaller eddies reducing its value. That can be the main reason for the large scatter of L_u observed between literature sources. In Figure 2.9 the differences between L_u and L^x according to ESDU are plotted.

The results of integral length scales obtained from the wind tunnel experiments are in good concordance with the results and curves given in the literature independently of the methodology selected for their calculation. The results depicted with the blue dots are smaller than those given by the red ones, but with an equivalent tendency. The latter are of special interest due to the good agreement between the measured spectra along the height and the Kaimal spectrum as shown in Figure 2.8(b). For larger heights, the obtained values of L_u decrease slightly. This effect, contrary to a natural boundary layer, can be related to the influence of the ceiling of the wind tunnel limiting its height. Another reason may be related to the special shape of the turbulence generators depicted in Figure 2.6. Nevertheless, for an intelligent comparison between integral length scales, it is necessary to know the mathematical method for which they are calculated. Therefore, results of L_u provided by field measurements, wind tunnel experiments or theories derived from fluid dynamics are difficult to compare.

The method for calculating L_u from the first zero-cross has been omitted in the current work due to the random nature of this point.

The behaviour of the wind spectra along the height is depicted in Figure 2.10. The fitted curves according to eq. 2.9 are plotted for the heights 10, 16, 30 and 40 cm. The shape of the approximated curves seems to be quite similar among each other. At each

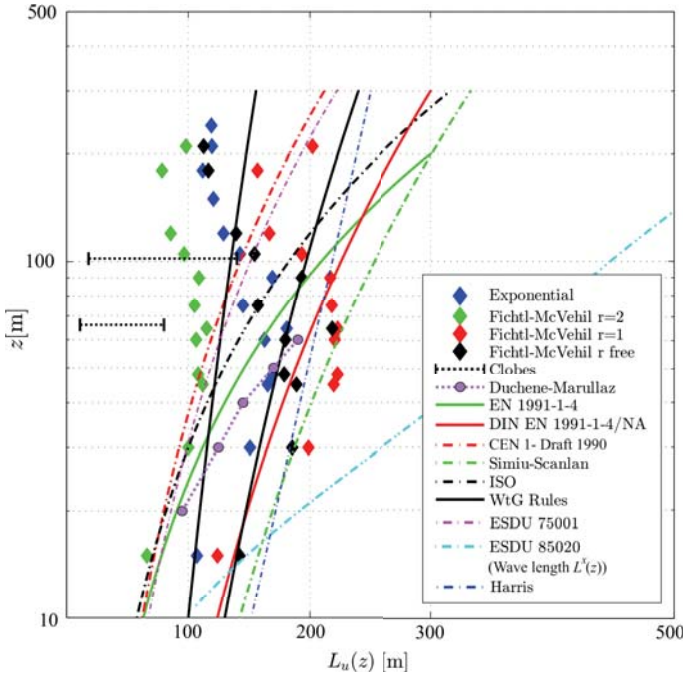

Figure 2.9: Comparison of integral length scales for $z_0 = 0.05$ m

height, the turbulence spectrum has been normalized with the corresponding standard deviation σ_u, the integral length scale L_u and the mean wind speed $\bar{U}$.

2.3.2 Wind structure in disturbed flow

The interference effect of an industrial building on the wind flow is studied by placing scale models of power houses inside the wind tunnel. The disturbances on the flow due the presence of a body are measured at the position where the chimney is supposed to be constructed. A parametric study has been carried out varying the shape of the buildings, the wind direction and the location of the chimney. The building models are made using 6 mm thick plexiglass plates. Figure 2.11 depicts the measuring set-up of the parametric study. It shows the dimensions and shapes of the tested buildings.

The location of the chimney with respect to the building is one part of the parametric study. As explained in the introduction, Ruscheweyh [1997] studied the influence of the presence of a nearby building, but only in terms of the vortex induced vibrations of slender chimneys. Ruscheweyh has shown that the maximum amplitude at the top of the chimney

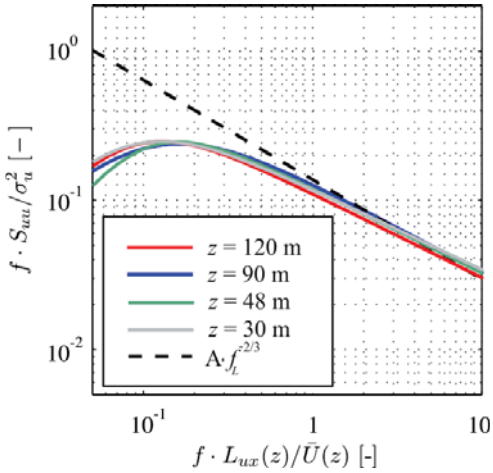

Figure 2.10: fitted S_{uu} for different heights

occurs when the chimney is located at the corner of the building. Hence, the location of the chimney has been altered (middle and corner) and is described by the parameter a_1.

The wind direction θ is also taken into account. Different directions have been studied rotating the models around the position of the measurement axis (chimney's position) using the turntable. When the chimney is located at the corner of the building, 24 wind profiles have been measured every 15 degrees. When the chimney is located in the middle, only 12 measurements are needed due to the symmetry.

The selection of the model scale has to be decided considering the side effects that could negatively affect the quality of the results. The blockage effect produced in the wind tunnel due to the placement of the building has been taken into account. If bodies are introduced inside the wind tunnel, a reduction of the effective cross section perpendicular to the flow is observed. For a continuous medium, temperature and blower efficiency, the reduction of the remained cross section accelerates the flow over and around the model. As stated in WtG and ASCE [1999], if the blockage ratio is lower than 5% with regard to the orientation with the highest blockage, the distortion is negligible. This condition is fulfilled. Nevertheless, the blockage effect is slightly visible in the results and, therefore, it was corrected by shifting the measured wind profiles at $z = 80$ cm high to the undisturbed ones.

Figure 2.12 shows the position of the measurement device behind the rectangular and cubic models. As outlined in Figure 2.11, the head of the Cobra is always located at the measurement axis where the chimney is supposed to be. The placement of the device at

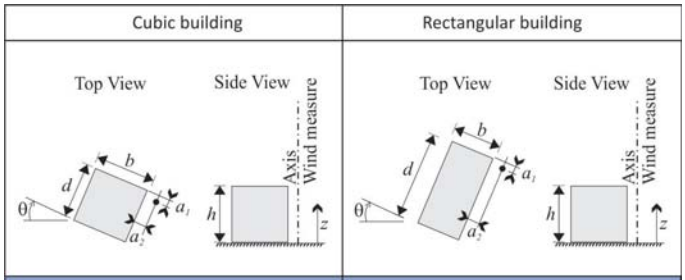

Variable	Modell [cm]	Prototype [m]	Variable	Modell [cm]	Prototype [m]
b	21.2	64	b	15	45
d	21.2	64	d	30	90
h	21.2	64	h	15	45
a_1	2.6 / 10.6	8 / 32	a_1	2.6 / 15	8 / 45
a_2	3	9	a_2	3	9

Figure 2.11: Measuring set-up

the measuring point is done using a laboratory clamp, which is often used to hold test tubes or smaller narrow-mouth flasks. For an effective description of the wind field, 13 measurements have been carried out over the height and their results have been compared with the undisturbed conditions. The measured heights in the wind tunnel are [cm]:

$$z_{measure} = [3\ 5\ 10\ 15\ 20\ 25\ 30\ 35\ 40\ 50\ 60\ 70\ 80]$$

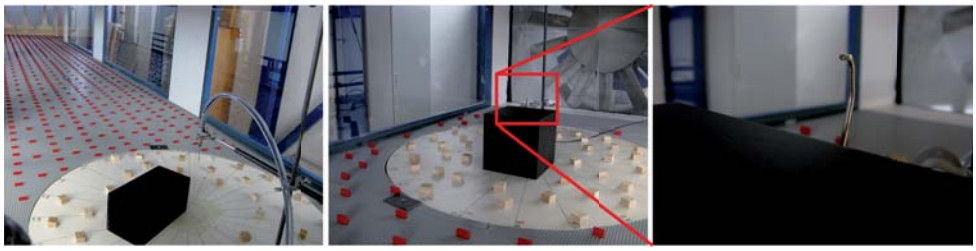

Figure 2.12: Measurements of the wind field at the chimney's position

The mean wind speed profile shows significant variations compared to the undisturbed flow due to the presence of the power house. Figure 2.13(a) depicts the mean wind speed profile with and without the cubic building. The blue markers represent the undisturbed flow as shown in Figure 2.7(a). The green markers correspond to the disturbed flow acting on the chimney. Its performance can be divided into three different zones. Firstly, for a wind angle of $\theta = 15°$ the chimney is located leeward and therefore, a shadow effect occurs, thus reducing the wind speed close to zero up to the height of the building. Secondly, starting from the building's roof, a speed-up of the wind speed occurs. The flow is accelerated and even surpasses the velocity of the undisturbed flow. For critical wind directions, a significant increase up to 10% can be observed at a height 1.5 times the height of the building. Differences between the mean wind speed of the undisturbed flow and the mean wind speed with power house can be observed up to a height of approximately three times the height of the power house. Finally, at high altitudes the interference effect is dissipated, thus returning to the natural flow conditions. These results can be barely compared with other published measurements due the little guidance given in the technical literature related to the speed-ups behind buildings. Ishizaki u. Yoshikawa [1972] carried out two-dimensional wind tunnel tests with laminar flow conditions. The mean wind speed profile is accelerated about 25% at the leeward edge of a flat roof building at a height 1.5 times the height of the building. On the other hand, other 2D studies have been published regarding the flow acceleration due to the presence of obstacles or natural escarpments such as vertical cliffs, which can be vaguely similar to a vertical building (Bowen u. Lindley [1977]). Field results by Bowen [1979] revealed a remarkable acceleration of the flow up to 20% at a height 1.5 times the height of the vertical cliff.

In Figure 2.13(b), the turbulence intensity profile is shown. The building has a strong influence on the wind speed fluctuations near the roof, but differences are observed only up to two times the height of the power house. A similar conclusion was reached by Bowen [1979] using wind tunnel experiments. The huge increase of the turbulence intensity over the top of the building is larger than the changes of the mean wind speed profile. Behind the building, following the expression eq. 1.6, wind velocities close to zero result in extremely large turbulence intensities without applicable considerations.

Figure 2.14(a) compares the turbulence spectrum of the undisturbed and disturbed flow at a height of 105 m and a wind direction $\theta = 15°$. The normalized spectra are plotted and no significant differences between the spectra in undisturbed and disturbed conditions can be observed. However, the measurements are plotted for a normalized frequency using the standard deviation σ_u, integral length scales L_u and mean wind speeds $\bar{U}$ corresponding to each set up. If a different way is used to present the results, the effect of the interference can be identified easily. Figure 2.14(b) also shows the power spectral density functions at different heights when the building is introduced. But in this case, the disturbed spectra

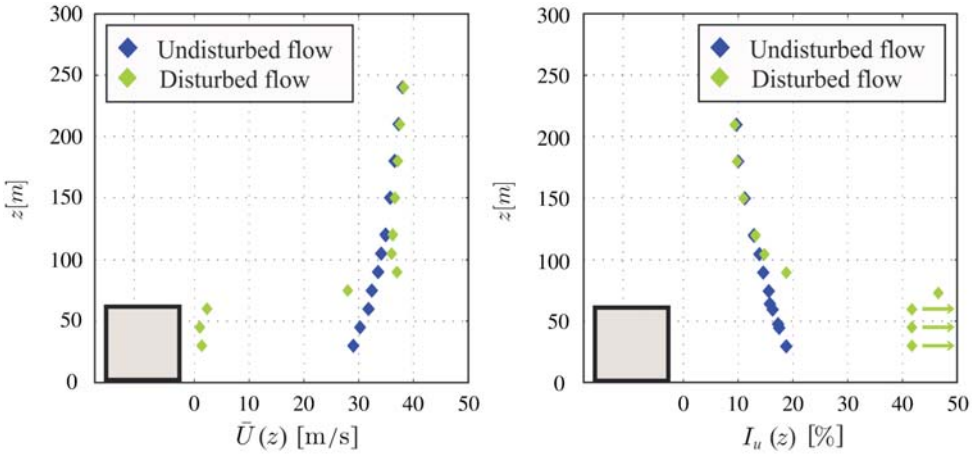

Figure 2.13: Comparison between undisturbed and disturbed flows. Cubic building, chimney located at the corner and $\theta = 15°$

are normalized using the variables of the undisturbed flow. It can be observed that there is a significant increase of gust energy due to interference phenomena. This increase decays when the height increases. Of course, although the integral of the normalized spectra over the normalized frequency is different than the unit, this representation has been used only to highlight the increase of the energy with respect to the frequency.

The increase of the energy of the fluctuating wind process $u(z,t)$ is directly related to the variance σ_u^2 of the fluctuating part of the wind velocity. Therefore, in the presence of disturbed flow, the considerable increase flow pointed out in Figure 2.14(b) can also be shown by plotting the standard deviation σ_u. Figure 2.15 compares σ_u in undisturbed flow and under interference conditions (cubic building, chimney located at the corner and $\theta = 15°$).

For undisturbed flow, the standard deviation of the wind speed decreases uniformly if the height increases. It increases faster at low heights because of the high turbulence provoked by the roughness elements inside the wind tunnel. In disturbed conditions, the standard deviation of the wind speed increases dramatically at heights near to the top of the building (60 meters). For example, at 75 m, the standard deviation increases about two and a half times in comparison with the undisturbed flow. The difference in the standard deviation between disturbed and undisturbed conditions decays when the height increases. Consequently, Figure 2.15 corroborates the observed differences in the turbulence components depicted in Figure 2.13(b) and Figure 2.14(b). For further

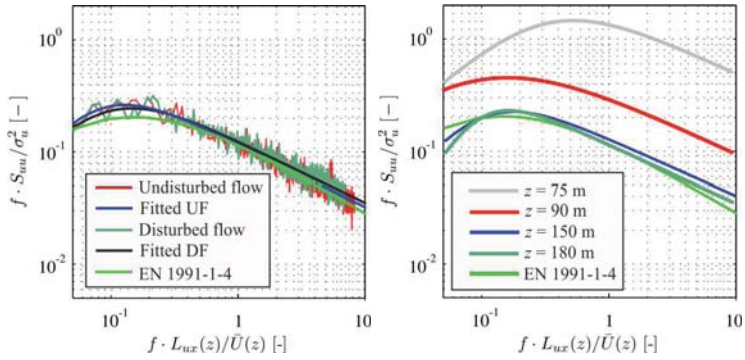

(a) comparison of S_{uu} at $z = 105$ m (b) Normalized spectra using variables from undisturbed flow

Figure 2.14: Examples of S_{uu} for disturbed wind. Cubic building, chimney located at the corner and $\theta = 15°$

details, graphs and results about the measurements of the wind field under disturbed wind conditions for each different configuration, see Clobes u. a. [2012a].

2.4 Mathematical proposal for the disturbed mean wind speed profile

In order to cover the disturbances of the interference effects on the mean wind speed, the mean wind speed profile under disturbed conditions $\bar{U}_d(z)$ will be mathematically defined for an engineering application. The corrected wind speed profile is presented in closed form and it is defined for different building shapes, positions of the chimney and wind directions.

The squared relation between mean wind speed $\bar{U}$ and wind force $\bar{F}$ shows the fundamental relevance of this variable on the structural response of each structure subjected to an external wind action. As shown in Figure 2.13, if the disturbed mean wind speed is accelerated some 10% with respect to the undisturbed case, the acting force increases up to 20 % and has to be taken into account for the final design of the structure.

The increase of the mean wind speed over the roof of the building with respect to the undisturbed flow has been defined in terms of factor $\beta_{\bar{U}}(z, \theta)$:

$$\beta_{\bar{U}}(z, \theta) = \frac{\bar{U}_d(z, \theta)}{\bar{U}_0(z)} \tag{2.21}$$

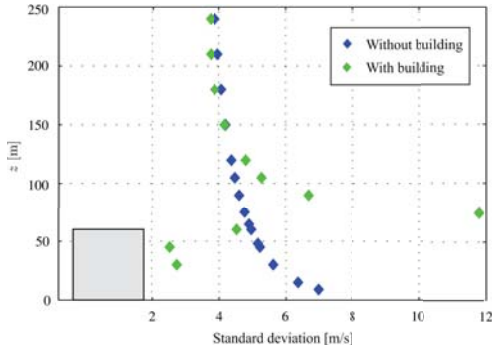

Figure 2.15: Standard deviation of the wind speed $\sigma_u(z)$ for both flow conditions

where $\bar{U}_d(z)$ is the mean wind speed profile obtained from disturbed conditions and $\bar{U}_0(z)$ is the profile obtained from the configuration without building. The blue dots in Figure 2.16 represent the increasing factor $\beta_{\bar{U}}(z, \theta)$ calculated for the cubic building, with the chimney positioned in the corner and a wind direction $\theta = 30°$ and $\theta = 120°$ respectively. The factor is depicted for a normalized height z/h, where z is the height above the ground and h is the height of the building. Due to the tendency of this factor over the height z, it can be linearly approximated without large errors. The blue lines symbolize the assumed linear interpolation.

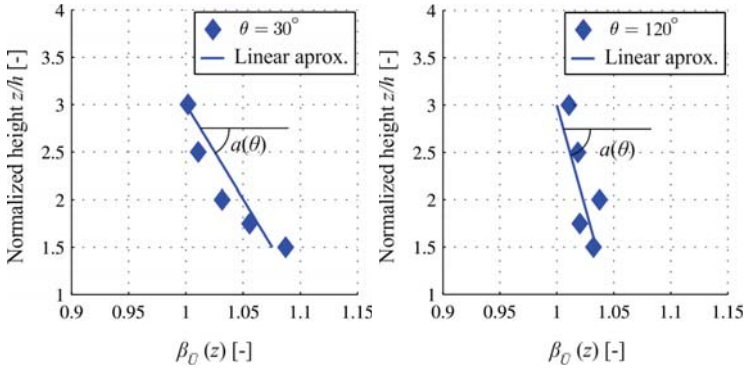

(a) $\beta_{\bar{U}}(z, \theta)$ for $\theta = 30°$ (b) $\beta_{\bar{U}}(z, \theta)$ for $\theta = 120°$

Figure 2.16: $\beta_{\bar{U}}(z, \theta)$ for a cubic building and chimney in the corner Clobes u. a. [2012a]

Table 2.1: Classification of the disturbed mean wind speed $\bar{U}_d(z,\theta)$ along the height z

Section	$\bar{U}_d(z,\theta)$	$\beta_{\bar{U}}(z,\theta)$
$z/h > 3$	$\bar{U}_d(z,\theta) = \beta_{\bar{U}}(z,\theta) \cdot \bar{U}_0(z)$	1
$1.5 < z/h < 3$		$1 + a(\theta) \cdot (z/h - 3)$
$1.25 < z/h < 1.5$		$1 - 1.5 \cdot a(\theta)$
$1 < z/h < 1.25$	Linear approximation between $\bar{U}_d(h,\theta)$ and $\bar{U}_d(1.25 \cdot h,\theta)$	-
$0 < z/h < 1$	$\bar{U}_d(z,\theta) = \beta^* \cdot \bar{U}_d(1.5 \cdot h,\theta)$	-

The analysis of factor $\beta_{\bar{U}}(z,\theta)$ has shown, that the change produced by the disturbed flow on the mean wind speed is observable up to a height of 3 times the height of the building. Up this height, both profiles show an identical shape.

The wind profile in disturbed flow is strongly influenced by the wind direction θ and the position of the chimney with respect to the building. Therefore, factor $\beta_{\bar{U}}(z,\theta)$ has also been defined depending on these variables.

Due to the complex shape of the disturbed profile, the mean wind speed profile can be globally broken up into five different sections over the height, as shown in Table 2.1. The length of the sections is related to the ratio z/h.

The influence of the shape of the building and the chimneys position on the factor $\beta_{\bar{U}}(z,\theta)$ is considered in the variable $a(\theta)$, which represents the slope of the correction factor as shown in Figure 2.16. No big differences have been observed between the cubic and the rectangular power houses. Therefore, the wind direction-dependent variable $a(\theta)$ is defined for two different cases depending on the shape of the adjacent building and the position of the chimney:

Cubic or rectangular building and chimney located at the corner:

$$a(\theta) = -0.03 \cdot \left(1 + \sin\left(\theta + \frac{180^\circ}{\pi}\right)\right) \quad \text{for } 0^\circ < \theta < 360^\circ \tag{2.22}$$

Cubic or rectangular building, chimney located in the middle:

$$a(\theta) = -0.05 \cdot \left(1 - \sin\left(2 \cdot \theta - 3.5 \cdot \frac{180^\circ}{\pi}\right)\right) \quad \text{for } 0^\circ < \theta < 180^\circ \tag{2.23}$$

For heights below $z/h = 1.25$, the disturbed mean wind speed profile $\bar{U}_d(z, \theta)$ does not depend on the position of chimney. Below the height of the power house, $0 < z/h < 1$, a unified solution is difficult to achieve. The problem is local and related to the zero-velocity vortex generated in front of the walls. From an engineering point of view, its importance is not relevant for the design. Nevertheless, a constant correction factor β^* for the height below $z < h$ is also proposed. This factor depends also on the wind direction θ:

$$\bar{U}_d(z, \theta) = \beta^*(\theta) \cdot \bar{U}_d(1.5 \cdot h, \theta) \quad \text{for } z < h \tag{2.24}$$

Table 2.2 summarizes the values of the correction factor $\beta^*(\theta)$.

Table 2.2: Correction factor $\beta^*(\theta)$ for the cubic and rectangular building

$0^\circ - 75^\circ$	90°	$105^\circ - 135^\circ$	$150^\circ - 225^\circ$	$240^\circ - 255^\circ$	$270^\circ - 330^\circ$	345°
0.1	0.5	0.85	0.33	0.85	0.33	0.5

For the first section above the roof of the building, $1 < z/h < 1.25$, the corrected profile follows a linear approximation between the two values calculated at $z = h$ and $z = 1.25 \cdot h$; between $1.25 < z/h < 1.5$, factor $\beta_{\bar{U}}$ remains constant and equal to $\beta_{\bar{U}} = 1 - 1.5 \cdot a(\theta)$.

Figure 2.17 shows the results of the above presented approach. The results are plotted for the configuration of a cubic building and a chimney located at the corner. The wind directions are $\theta = 30^\circ$ and $\theta = 120^\circ$. The blue dots symbolize the mean wind speed profile measured in the wind tunnel for the disturbed conditions. The black line corresponds to the approximated wind speed profile from the undisturbed wind condition as presented in Section 2.3.1. The red line represents the linear correction of the disturbed wind profile $\bar{U}_d(z, \theta)$ according to Table 2.1. The results show a good agreement between the measured data in the wind tunnel and the new approach. Over the building, the error between the new corrected profile and the measured mean wind speed in the wind tunnel using the above presented formulas is less than 5%.

The above presented method to define in a closed form the influence of the interference effect on the mean wind speed profile has several advantages. Due to the excellent agree-

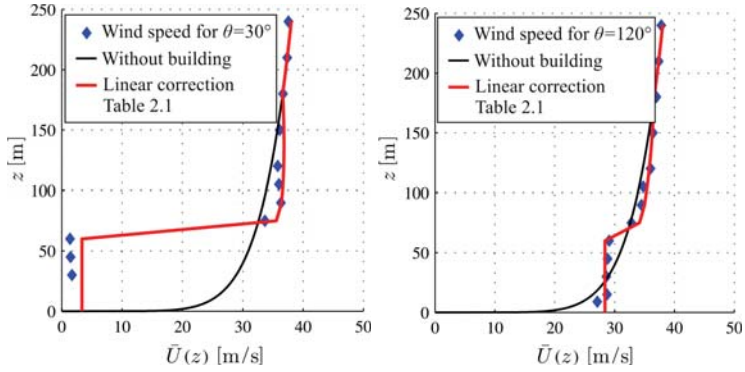

(a) $\bar{U}_d(z,\theta)$ for $\theta = 30$ (b) $\bar{U}_d(z,\theta)$ for $\theta = 120$

Figure 2.17: Corrected wind profiles for disturbed flow for cubic building and chimney in the corner Clobes u. a. [2012a]

ment of the undisturbed wind profile obtained in the wind tunnel with the logarithmic law presented in EN 1991-1-4, factor $\beta_{\bar{U}}(z,\theta)$ can be directly applied as correction factor:

$$\bar{U}_d(z,\theta) = \beta_{\bar{U}}(z,\theta) \cdot \bar{U}_{EC}(z) \tag{2.25}$$

The disturbed profile $\bar{U}_d(z,\theta)$ will be now inserted in the mathematical approach of the gust response factor G_x in order to provide an equivalent expression considering the presence of nearby buildings.

The increase of the wind turbulence $\sigma_u(z)$ over the roof of the building for the disturbed flow, visible for almost all cases, seems to have a random nature without defined tendency. Therefore, due to the efforts to define its behaviour with a logical mathematical formula, it was not possible to present this variable in a closed form. A similar disappointment was also observed with the wind spectrum $S_{uu}(f,z)$.

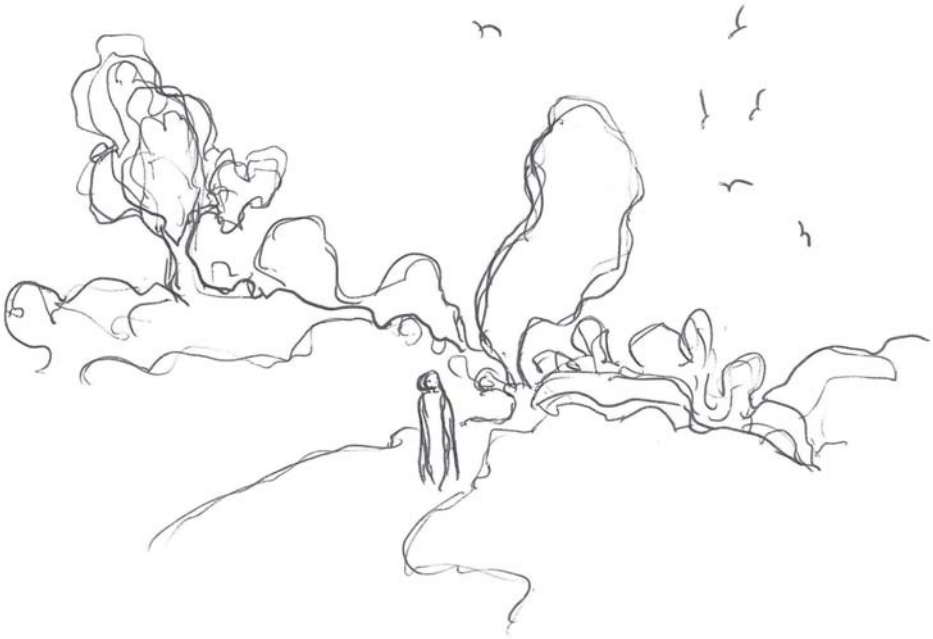

Jose Mari Sasieta. "Paisajes de viento".

3 Simulation of the dynamic response of a slender chimney under interference effect

In this chapter, a brief introduction to the mathematical background about the application of the stochastic vibration theory to buffeting wind loading on structures is given. The mathematical procedure about the gust response factor G_x concept is presented and a comparison with the structural factor $c_s c_d$ defined in EN 1991-1-4 is provided.

The mean wind speed profiles $\bar{U}(z)$ and turbulence spectra $S_{uu}(z, f)$ collected from the wind tunnel experiments under interference conditions are used to simulate the gust buffeting wind loading on a real industrial chimney. The simulation will be carried out in the frequency domain using a self-programmed algorithm in Matlab. The scope of this chapter is to provide in a qualitative manner the effect produced due to the change in the wind field on the dynamic response of the chimney. As simplification, the simulation will be carried out assuming quasi-steady loading process, i.e without contribution of the aerodynamic admittance function $|\chi(f)|^2$, which will be later identified from the HFFB measurements.

The calculation process has been defined using the Finite Element Method FEM technique matching the height of the nodes of the structure with the heights for which the wind field was measured in the wind tunnel. As stated in the introduction, high slender chimneys located in industrial areas are normally supported by the nearby building, reducing the transmitted forces to the foundation having an important economic advantage. For this simulations, the response of a propped 150 m high steel chimney under gust buffeting is simulated. The structural connection is placed for a height of 60 m, which corresponds approximately to the roof's height of the cubic building tested in the wind tunnel, see Figure 2.11. The results show a considerable increase of the bending moment M_y and along-wind force F_x at the supported connection. The difference on the loading between disturbed and undisturbed flow conditions shows a significant wind direction θ dependency.

3.1 The stochastic vibration theory applied to wind loading

The mathematical background regarding the wind-induced vibrations was initially defined by Davenport in the 1960s (Davenport [1961], Davenport [1963] and Davenport [1964]). Due to the difficulty to obtain in a deterministic way the response of a structure under random loading, the information of the response has been reduced to statistical parameters in terms of mean values, standard deviations and spectral density functions.

In wind engineering it is assumed that the wind speed, wind pressures and structural response can be defined as a stationary and ergodic process. Therefore, the actual value of each of these processes $S(t)$ can be separated into a mean component $\bar{S}$ and a zero-mean fluctuating part $s(t)$ as follows:

$$S(t) = \bar{S} + s(t) \tag{3.1}$$

This assumption is used to calculate the standard deviation of the fluctuating response σ_x for a linear system in the frequency domain.

3.1.1 Along-wind response of a SDOF under wind buffeting

Considering a simple mass-spring-damper SDOF system depicted in Figure 3.1 under a time dependent wind force $F(t)$ and with the following equation of motion:

$$m \cdot \ddot{x} + c \cdot \dot{x} + k \cdot x = F(t) \tag{3.2}$$

The total along-wind response $X(t)$ according to eq. 3.1 can be divided into a mean response $\bar{X}$ and a fluctuating component $x(t)$ represented in terms of their standard deviation σ_x, in which the dynamic effects are included:

$$X(t) = \bar{X} + x(t) \tag{3.3}$$

The mean or static response $\bar{X}$ is directly related to the mean wind force $\bar{F}$ acting on the structure:

$$\bar{F} = k \cdot \bar{X} \tag{3.4}$$

where k is the stiffness of the system. The mean wind force $\bar{F}$ acting on a surface A_{ref} is proportional to the dynamic pressure and therefore, proportional to the square of the mean wind speed $\bar{U}$:

$$\bar{F} = \frac{1}{2} \cdot \rho \cdot \bar{U}^2 \cdot A_{ref} \cdot C_D \tag{3.5}$$

where the mean drag coefficient C_D depends on the Reynolds number Re.

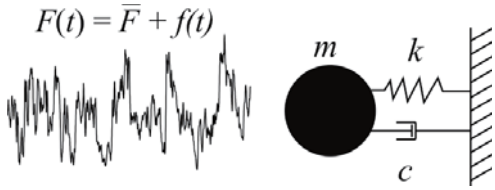

Figure 3.1: SDOF dynamic model of a structure

Regarding the fluctuating component of the response $x(t)$, the quasi-steady theory allows some advantages to reduce the complexity of the calculation. This assumption is the basic assumption of many wind loading codes and standards (Holmes [2007]). It assumes that the fluctuating pressures on a surface of the structure follow the variations in longitudinal wind velocity streams. Transforming the zero-mean fluctuating pressures into zero-mean fluctuating forces $f(t)$ and neglecting the fluctuations of second order, the following expression can be obtained:

$$f(t) \cong C_D \cdot \frac{1}{2} \cdot \rho \cdot A_{ref} \cdot [2 \cdot \bar{U} \cdot u(t)] \tag{3.6}$$

where the quasi-steady relationship $f(t) \propto u(t)$ between fluctuating forces and fluctuating wind component is given. If the root mean square of the fluctuating forces $f(t)$ is to be treated in a statistical way, then:

$$\overline{f(t)^2} = \overline{\left[C_D \cdot \frac{1}{2} \cdot \rho \cdot A_{ref} \cdot [2 \cdot \bar{U} \cdot u(t)] \right]^2} = C_D^2 \cdot \rho^2 \cdot A_{ref}^2 \cdot \bar{U}^2 \cdot \overline{u(t)^2} = 4 \cdot \frac{\bar{F}^2}{\bar{U}^2} \cdot \overline{u(t)^2} \tag{3.7}$$

Due to the equivalence of the mean squared value and the integral of a spectral density, eq. 3.7 can be rewritten in terms of spectral density functions in the frequency domain:

$$\int_0^\infty S_f(f) \cdot df = 4 \cdot \frac{\bar{F}^2}{\bar{U}^2} \cdot \int_0^\infty S_u(f) \cdot df \tag{3.8}$$

In case of larger structures, the action of the fluctuating wind over the surface does not occur simultaneously due to a lack of correlation in space of the acting wind field. The aerodynamic admittance function $|\chi(f)|^2$ takes this effect into account.

$$S_f(f) = 4 \cdot \frac{\bar{F}^2}{\bar{U}^2} \cdot S_u(f) \cdot |\chi(f)|^2 \tag{3.9}$$

If a quasi-steady calculation is going to be carried out, the aerodynamic admittance function $|\chi(f)|^2$ is defined as $|\chi(f)|^2 = 1$. The dynamic response of a linear structure to an external load action is dominated in the frequency domain by the mechanical transfer function $|H(f)|^2$. With this information it is possible to build the spectral density function of the structural deflections $S_x(f)$:

$$S_x(f) = \frac{1}{k^2} \cdot |H(f)|^2 \cdot S_f(f) = \frac{1}{k^2} \cdot |H(f)|^2 \cdot 4 \cdot \frac{\bar{F}^2}{\bar{U}^2} \cdot S_u(f) \cdot |\chi(f)|^2 \tag{3.10}$$

According to the theory of stochastic processes, it can be demonstrated that the integration over the entire frequency axis of the power spectral density function $S_x(f)$ is equal to the variance of the stochastic process σ_x^2:

$$\sigma_x^2 = \int_0^\infty S_x(f) \cdot df \tag{3.11}$$

Combining this latter term σ_x^2 and the mean response $\bar{X}$ calculated in eq. 3.4, the response of the structural system to a stochastic loading is fully described.

The response spectrum $S_x(f)$ defined in eq. 3.10 is usually adjusted dividing it into two different components as shown in Figure 3.2. The background component Q^2 can be defined as the quasi-static response related to the wind spectrum acting on the structure, without dynamic amplification. On the contrary, the resonant component R^2 depends on the mechanical amplification provoked by the fundamental frequency f_0 of the structure.

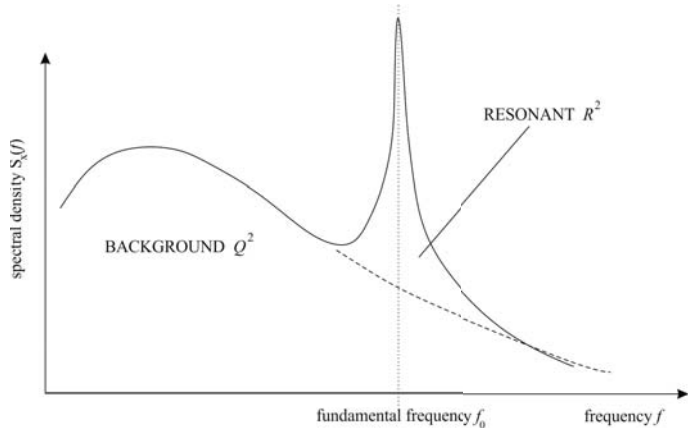

Figure 3.2: Background and resonant components of the response spectrum $S_x(f)$

Multiplying and dividing eq. 3.10 by σ_u^2, and considering the relationship of eq. 3.5, eq. 3.11 becomes:

$$\sigma_x^2 = 4 \cdot \frac{\bar{X}^2 \cdot \sigma_u^2}{\bar{U}^2} \int_0^\infty |H(f)|^2 \cdot |\chi(f)|^2 \cdot \frac{S_u(f)}{\sigma_u^2} \cdot df \tag{3.12}$$

If it is assumed that over the width of the resonant peak on Figure 3.2, the aerodynamic admittance function $|\chi(f)|^2$ and wind spectrum $S_u(f)$ are constant at the values $|\chi(f_0)|^2$ and $S_u(f_0)$ (Holmes [2007]), then:

$$\sigma_x^2 \cong 4 \cdot \frac{\bar{X}^2 \cdot \sigma_u^2}{\bar{U}^2} \cdot [Q^2 + R^2] \tag{3.13}$$

with:

$$Q^2 = \int_0^\infty \frac{S_u(f)}{\sigma_u^2} \cdot |\chi(f)|^2 \cdot df \tag{3.14}$$

$$R^2 = |\chi(f_0)|^2 \cdot \frac{S_u(f_0)}{\sigma_u^2} \int_0^\infty |H(f)|^2 \cdot df \tag{3.15}$$

The integral defined in eq. 3.15 was mathematically adjusted by Hurty u. Rubinstein [1964] by means of the residue theorem, which is equal to $(\pi \cdot f_0/4 \cdot \xi)$, where ξ is the structural damping ratio (Simiu u. Lozier [1975]):

$$R^2 \cong \frac{\pi \cdot f_0}{4 \cdot \xi} \cdot \frac{S_u(f_0)}{\sigma_u^2} \cdot |\chi(f_0)|^2 \tag{3.16}$$

The expression of eq. 3.13 is widely used in the international standards to study the along-wind response of structures. In case of the European standard EN 1991-1-4 the design approach was defined by Solari during the 80's and 90's starting from this equation.

3.1.2 Gust response factor

Starting from the above presented equations, Davenport [1967] uses the mathematical background of the probability distribution of peak values to derive the concept of gust response factor G_x. This factor is commonly used in wind engineering and is proposed in every standard worldwide.

To find the probability distribution of a determined maxima it is necessary to know the combined probability of the mean response and its associated maxima. The distribution of the extreme values has a narrow shape and, if its probability is approximated to its own mean, then the maximum peak response of the system depicted in Figure 3.1 can be written as Davenport [1964]:

$$\hat{X} = \bar{X} + g_x \cdot \sigma_x \tag{3.17}$$

where g_x is known as the peak factor and depends on the expected frequency ν and on the period of observation T in seconds:

$$g_x = \sqrt{2 \cdot \ln(\nu \cdot T)} + \frac{0.577}{\sqrt{2 \cdot \ln(\nu \cdot T)}} \tag{3.18}$$

The concept of a peak factor, developed in order to predict the maximum response of a narrow band process, was originally introduced by Longuet-Higgins [1952]. Davenport upgraded the initial formulations assuming some mathematical conditions as for example the stationarity of the wind process during the time interval T ($T = 600$ sec. for EN

1991-1-4). On the other hand, Rice [1945] introduced the concept of the upcrossing rate of maxima to derive the expected frequency ν in the following terms:

$$\nu = \frac{1}{2\pi} \cdot \frac{\sigma_{\dot{x}}}{\sigma_x} = \frac{\sqrt{\int_0^\infty f^2 \cdot S_x(f) \cdot df}}{\sqrt{\int_0^\infty S_x(f) \cdot df}} \tag{3.19}$$

Factor $\nu \cdot T$ can be interpreted as the number of maxima that occur in a period T. In case of narrow band processes, typical for structures with low natural frequency and small damping, the number of maxima during a unit time coincides with the number of zero-crossing over the same time. Consequently, for narrow band processes the expected frequency can be well approximated with the natural frequency of the system:

$$\nu \cong f_0 \tag{3.20}$$

Then the gust response factor G_x can be defined as the ratio between the expected maximum response of the structure $\hat{X}$ and the mean $\bar{X}$, in a defined time period T:

$$G_x = \frac{\hat{X}}{\bar{X}} = 1 + g_x \cdot \frac{\sigma_x}{\bar{X}} \tag{3.21}$$

Replacing eq. 3.13 in eq. 3.21:

$$G_x = 1 + 2 \cdot g_x \cdot \frac{\sigma_u}{\bar{U}} \cdot \sqrt{Q^2 + R^2} = 1 + 2 \cdot g_x \cdot I_u \cdot \sqrt{Q^2 + R^2} \tag{3.22}$$

The design codes use eq. 3.22 to calculate the maximum along-wind response of structures under wind buffeting. The usual procedure is to calculate G_x for the modal coordinate in the first vibration mode. Then G_x is multiplied by the mean load distribution on the structure. Using this information, responses such as along-wind forces, displacements or bending moments are calculated.

Despite this, some discussions are given in the literature about the efficiency of the application G_x to determine each maximum effect produced by the wind action on the structure Holmes [2009], Zhou u. a. [1999b]. If the gust response factor G_x is calculated for the deflection x of the structure, it is not necessarily identical to the G_{M_y} provoked

by the bending moments or G_{F_x} by the shear forces at any elevation of the structure. As stated by Zhou u. a. [1999a], the constant gust response factor G_x provides excellent results for the determination of the maximal deflection $\hat{X}$ but results in less accurate estimation of the maximal base shear force $\hat{F}_x$. The resonance produced by the wind on the structure depends, among other things, on the inertial mass. Therefore, if a structure has a varying mass distribution over the height, the exact gust response factor G_x changes over the height. Some of these uncertainties are solved from the loading side in EN 1991-1-4 referring its structural factor $c_s c_d$ on the profile of the peak velocity pressure instead of the mean velocity pressure profile (Niemann [2013]).

The Eurocode EN 1991-1-4 defines the structural factor $c_s c_d$ as the combination of the two separated factors c_s and c_d (see eq. 1.21). This factor is used to calculate the along-wind response of a structure in its fundamental mode of vibration. This factor can be described as the ratio:

$$c_s c_d = \frac{\text{maximum response including resonant and correlation effects}}{\text{maximum response due to peak gust loading}}$$

and mathematically as:

$$c_s c_d = \frac{G_x(z_s)}{1 + 7 \cdot I_u(z_s)} \tag{3.23}$$

where z_s is the reference height, located at 60% of the total height of the structure. Factor 7 in the denominator is obtained after consideration of peak factor $g_x = 3.5$ in case of a quasi-static response of a point-like structure for a 1-sec gust (Niemann [2013]). The size factor c_s takes into account the non-simultaneous action of the peak wind pressure over the entire surface of the structure. The effect of gusts on the whole surface reduces the maximum response of the structure.

$$c_s = \frac{1 + 7 \cdot I_u(z_s) \cdot \sqrt{Q^2}}{1 + 7 \cdot I_u(z_s)} \tag{3.24}$$

The dynamic factor c_d considers the dynamic response of the structure in its fundamental mode due to the action of the wind turbulence. Flexible structures tend to amplify the

response at their natural frequencies, so that both effects compensate each other Cook [2007].

$$c_d = \frac{1 + 2 \cdot g_x \cdot I_u(z_s) \cdot \sqrt{Q^2 + R^2}}{1 + 7 \cdot I_u(z_s) \cdot \sqrt{Q^2}} \tag{3.25}$$

If the value of c_d is greater than one, it indicates a significant resonant response of the structure.

The application of eq. 3.22 or eq. 1.21 has to be carried out carefully due to the difference between mean velocity pressure and q_m peak velocity pressure q_p associated to the mean wind speed and the gust peak velocity respectively. The static maximum force F_w can be calculated applying both factors:

$$\begin{aligned} F_w &= G_x \cdot C_D \cdot q_m(z_s) \cdot A_{ref} \\ F_w &= c_s c_d \cdot C_D \cdot q_p(z_e) \cdot A_{ref} \end{aligned} \tag{3.26}$$

where z_e is the defined reference height that always corresponds to the height of the structure H. The other reference height $z_s = 0.6 \cdot H$ is only applicable for the determination of $c_s c_d$ or G_x. As stated by Cook [2007], the use of z_s for the calculation of the peak pressures q_p provokes a serious underestimation of design wind loads.

For a more detailed overview about the implementation of the gust response factor G_x in the international standards, see Kwon u. Kareem [2013]. The along-wind loading formulation in the eight major standards is compared, taking into account the assumptions and simplifications carried out for its development.

3.1.3 Application of the FEM technique in the along-wind response of a MDOF system

The above presented mathematical formulation for the determination of the response of a SDOF system to a stochastic stationary wind action has to be implemented in the finite element method. As explained in Peil [1993], there are different methodologies to solve this type of calculations using the Finite Element Method FEM, but in this case the chosen method is the direct transfer formulation in the frequency domain. The main condition to use this methodology is the assumption of a linear system.

The transformation of the SDOF system explained in the previous section into a multi degree of freedom system MDOF requires the extension of the formulation to a matrix

based representation. The concept of a multi degree of freedom system MDOF is shown in Figure 3.3. The stationary wind force acting on the whole structure is transformed into a finite number of stochastic forces acting at the different nodes as depicted in Figure 3.3(a). The schematic view of the node-elements interaction is depicted in Figure 3.3(b). This explanation assumes n total nodes distributed over the entire height of the structure.

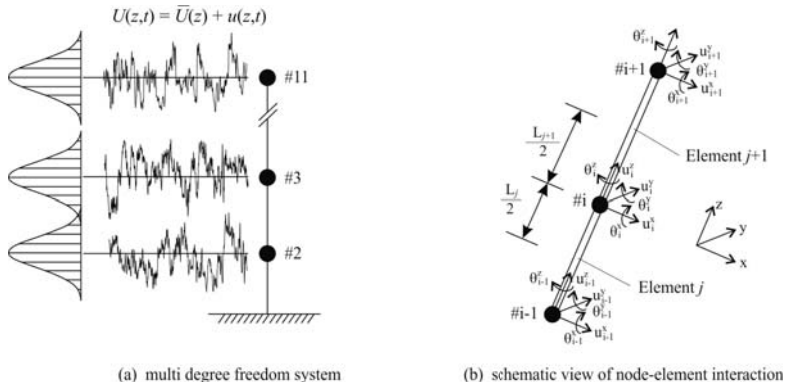

Figure 3.3: MDOF system considered in the calculation (Peil [1993])(a) and node-element decription (b)

The static mean force applied on an arbitrary node i is defined by adding the mean wind force $\bar{F}_{wind_i}$ to the corresponding dead weight of the half lengths $L_j/2$ and $L_{j+1}/2$ of the connected elements j and $j+1$, see Figure 3.3(b)

$$\bar{F}_{wind_i} = \frac{\rho}{2} \cdot \bar{U}(z_i)^2 \cdot C_{D_i} \cdot \frac{L_j + L_{j+1}}{2} \cdot D_i \tag{3.27}$$

Regarding the dynamic part of the calculation, the diagonal matrix $\mathbf{S}_{ff}$ contains n power spectral density functions $S_{ff_i}(z_i, f)$ containing the fluctuating loading process in wind direction. Modifying eq. 3.8 to a MDOF system, $S_{ff_i}(z_i, f)$ is defined as:

$$S_{ff_i}(z_i, f) = 4 \cdot \frac{\bar{F}_{wind_i}}{\bar{U}(z_i)} \cdot S_{uu_i}(z_i, f) \cdot |\chi(z_i, f)|^2 \tag{3.28}$$

The cross-correlated spectral density matrix $\mathbf{S_{ff}}(f)$ can be obtained expanding the terms from the diagonal $S_{ff_i}(z_i, f)$ to the other terms of the matrix using the coherence function $\gamma_{ij}(f)$ defined in eq. 1.13:

$$S_{ff_iff_j} = \sqrt{S_{ff_i}(P_i, f) \cdot S_{ff_j}(P_j, f)} \cdot \gamma_{ij}(f) \tag{3.29}$$

If the nodes are separated only in the vertical direction, which is typical for line-like structures such as chimneys, only the z component is considered in the application of the coherence function. The response in the frequency domain of a MDOF system, is obtained applying the following equation:

$$\mathbf{x}(f) = \mathbf{H}(f) \cdot \mathbf{f}(f) \tag{3.30}$$

If $\mathbf{f}(f)$ is a vector representing a stationary random wind force process characterized by a spectral density matrix $\mathbf{S}_{ff}$, then it is possible to obtain the following relationship Clough u. Penzien [1993]; the own complex conjugate of eq. 3.30 is:

$$\mathbf{x}(f)^* = \mathbf{H}(f)^* \cdot \mathbf{f}(f)^* \tag{3.31}$$

and the corresponding transpose:

$$\mathbf{x}(f)^{*T} = \mathbf{f}(f)^{*T} \cdot \mathbf{H}(f)^{*T} \tag{3.32}$$

multiplying eq. 3.30 and eq. 3.32:

$$\left[\mathbf{x}(f) \cdot \mathbf{x}(f)^{*T}\right] = \mathbf{H}(f) \cdot \left[\mathbf{f}(f) \cdot \mathbf{f}(f)^{*T}\right] \cdot \mathbf{H}(f)^{*T} \tag{3.33}$$

If both sides of equation (6.45) are multiplied by 1/T and taken limits as $T \to \infty$ then:

$$\mathbf{S_{xx}}(f) = \mathbf{H}(f) \cdot \mathbf{S_{ff}}(f) \cdot \mathbf{H}(f)^{*T} \tag{3.34}$$

where $\mathbf{H}(f)^{*T}$ represents the transpose of the complex conjugate of the transfer function $\mathbf{H}(f)$.

3.2 Simulation of a 150 m steel propped chimney subjected to interference effect

In order to verify the influence of the interference effect on the structural response of an industrial chimney, a 150 m high steel propped chimney is calculated. The calculation is carried out assuming a quasi-steady wind flow. The finite element method is applied and the wind data obtained from the wind tunnel tests have been used as wind loading input.

3.2.1 Structural characteristics of the chimney

Figure 3.4 shows the structural properties of the considered model and the partition in different elements used for the calculation. The propped chimney is connected at the roof of a 60 meters imaginary nearby building (for example a power plant) and it is divided into 10 beam elements of different lengths. Due to the high slenderness of the structure, the shear deformation can be neglected as compared to the bending effect on the deformations. At each node, 6 degrees of freedom have been considered (three displacements and three rotations). The chimney has a constant width of 2.5 m over its entire height. The thickness of the circular steel tubes varies over the height. After a modal analysis, the natural frequencies of the modelled chimney are obtained, being $f_0 = 0.25$ Hz and $f_1 = 1.53$ Hz.

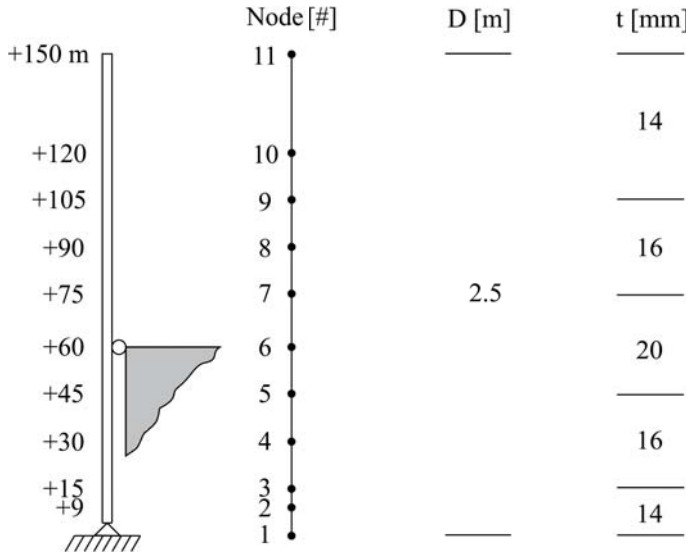

Figure 3.4: Structural properties of the propped chimney

For the structural damping, a logarithmic decrement of $\Lambda = 0.02$ is selected. This arbitrary damping value includes the material and assembly damping components. The mechanical damping matrix $\mathbf{D}_{mech}$ is calculated using the classical Rayleigh damping, where $\mathbf{D}_{mech}$ is a linear combination of the mass matrix $\mathbf{M}$ and stiffness matrix $\mathbf{K}$:

$$\mathbf{D}_{mech} = \alpha \cdot \mathbf{D} + \beta \cdot \mathbf{K} \tag{3.35}$$

Assuming the same damping for the first and second natural frequencies, the α and β coefficients can be mathematically obtained as follows:

$$\alpha = \frac{2 \cdot \Lambda \cdot (f_1 - f_0) \cdot f_0 \cdot f_1}{(f_1^2 - f_0^2)} \tag{3.36}$$

$$\beta = \frac{\Lambda \cdot (f_1 - f_0)}{2 \cdot \pi^2 (f_1^2 - f_0^2)} \tag{3.37}$$

Figure 3.5(a) depicts the course of the logarithmic decrement Λ with the frequency. The red dots represent the crossing points between the Rayleigh proposal and the natural frequencies.

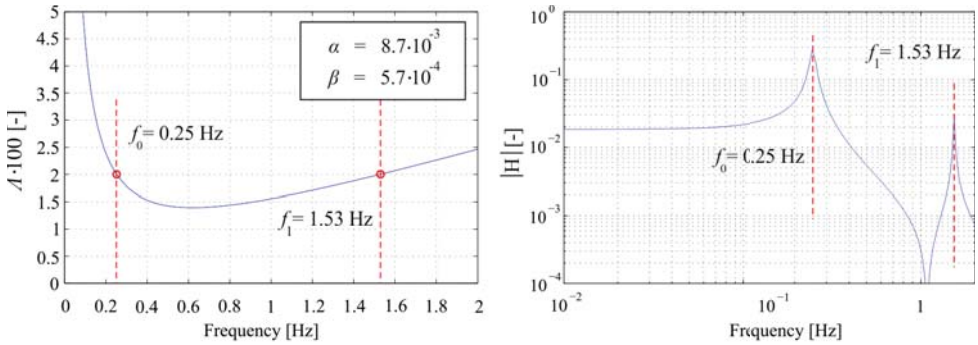

(a) definition of Λ using the Rayleigh method (b) transfer function at node #11

Figure 3.5: Rayleigh method for the determination of Λ (a) and mechanical transfer function at node #11

The aerodynamic damping $\mathbf{D}_{aero}$ is also considered in the calculation. The total load acting on a structure depends on the wind speed. Nevertheless, the velocity of the struc-

ture due to the deflections produced by the wind $\dot{\delta}_{def}$ reduces the total force. This physical effect can be defined as the aerodynamic damping:

$$F_{tot} = \frac{1}{2} \cdot \rho \cdot C_D \cdot A_{ref} \cdot (\bar{U} + u - \dot{\delta}_{def})^2 \tag{3.38}$$

As explained in Dyrbye u. Hansen [1997], in many occasions the aerodynamic damping is often of the same order of magnitude as the structural damping. Its effect increases when the wind speed increases and also if the mass ratio of the structure decreases. Therefore, it gives significant response reductions for light structures such as steel chimneys or lattice towers. If the total load is split into the three velocity components, eq. 3.39 it can be rewritten as:

$$F_{tot} = F_{mean}(\bar{U}) + F_{fluct}(u) - F_{aero}(\dot{\delta}_{def}) \tag{3.39}$$

The last term produces a negative force acting as a brake of the system. From eq. 3.38 the aerodynamic damping can be determined as follow:

$$F_{aero} = \rho \cdot C_D \cdot A_{ref} \cdot \bar{U} \cdot \dot{\delta}_{def} = 2 \cdot \frac{\bar{F}}{\bar{U}} \cdot \dot{\delta}_{def} \tag{3.40}$$

This damping is introduced in the damping matrix using a diagonal matrix (Clobes [2008]). Its effect is taken into account in wind direction at the eleven nodes of the chimney. Fluctuations in across-wind direction are not considered during the calculation.

$$\mathbf{D}_{aero} = diag\left(2 \cdot \frac{\bar{F}(z_1)}{\bar{U}(z_1)}, ..., 2 \cdot \frac{\bar{F}(z_{11})}{\bar{U}(z_{11})}\right) \tag{3.41}$$

Finally, the total damping matrix $\mathbf{D}$ is calculated as follows:

$$\mathbf{D} = \mathbf{D}_{mech} + \mathbf{D}_{aero} \tag{3.42}$$

The complex mechanical transfer matrix of the system $\mathbf{H}(f)$ depends on the mass matrix $\mathbf{M}$, the damping matrix $\mathbf{D}$ and the stiffness matrix $\mathbf{K}$. This function is defined in the frequency domain as:

$$\mathbf{H}(f) = \left(-(2\pi \cdot f)^2 \cdot \mathbf{M} + i \cdot (2\pi \cdot f) \cdot \mathbf{D} + \mathbf{K}\right)^{-1} \tag{3.43}$$

where f is the frequency. The response function $\mathbf{H}(f)$ relates the output of the system with the input forces in the frequency domain. Figure 3.5(b) depicts the reasoning of the complex function for the tip of the chimney (node #11). It can be observed that the two peaks coincide with the two first natural frequencies of the system.

3.2.2 Wind loading data from wind tunnel

The coordinates of the nodes displayed in Figure 3.4 are selected to coincide exactly with the measuring points in the wind tunnel. For this reason, the wind data obtained from the wind tunnel experiments can be directly transferred as wind loading on the nodes by taking into account the scale parameters.

The mean wind speed profiles $\bar{U}(z)$ obtained from the tests have been directly inserted in the FEM program as the mean wind speed to calculate the mean wind force $\bar{F}(z_i)$ at each node i. The wind under the structural support (from nodes #1 up to #6) has not been considered, focusing the wind load only on the cantilevered part of the chimney.

As stated above, the nodes of the system have been defined in the same Z axis, considering the structure as a line-like structure. This assumption reduces eq. 1.13 of the coherence in vertical direction only:

$$\gamma_{ij}(f) = exp\left(\frac{-2 \cdot f \cdot C_z \cdot \Delta_z}{\bar{U}_i + \bar{U}_j}\right) \tag{3.44}$$

Due to the absence of a second Cobra Probe at the moment of the experiments, it was not possible to define an own coherence function in the wind tunnel. Nevertheless, a $C_z = 11.5$ decay coefficient has been assigned for the simulation. This value coincides with the vertical decay coefficient given in EN 1991-1-4.

As explained in the introduction, the aim of these calculations is to demonstrate qualitatively the influence of a disturbed flow due to the presence of a nearby building on the dynamic response of a propped chimney. The real reduction of the effective wind loading due to the lack of correlation of the wind pressures over the chimney's surface has not been considered. Nevertheless, this effect, represented in the standards as the aerodynamic admittance function $|\chi(f)|^2$, will be consider for the new design approach.

3.3 Results of the simulations

A selection of the results provided by the parametric study can be found in the following section. For a better overview, the results have been divided into the two different building

shapes. While the maximum displacement of the chimney $\hat{x}$ has been calculated at the tip of the chimney (node #11) applying eq. 3.17, for the calculation of the maximum bending moment $\hat{M}_y$ and maximum lateral force $\hat{F}_x$ the following expressions have been used:

$$\hat{M}_y = \bar{M}_y + g_{M_y} \cdot \sigma_{M_y} \qquad \hat{F}_x = \bar{F}_x + g_{F_x} \cdot \sigma_{F_x} \tag{3.45}$$

where g_{M_y} and g_{F_x} are the peak factors which correspond to the stochastic processes $S_{M_yM_y}$ and $S_{F_xF_x}$ associated to the internal forces $\mathbf{S}_{el_j}$ of the element j assigned at the height of the support (node #6) and solved as follows:

$$\mathbf{S}_{el_j} = \mathbf{K}_{el_j} \cdot \mathbf{S}_{xx_{el_j}} \cdot \mathbf{K}_{el_j}^T \tag{3.46}$$

where $\mathbf{K}_{el_j}$ is the stiffness matrix of the beam element j. To appreciate the influence of the wind direction θ, the results have been plotted in polar coordinates. The representation of the results is given in terms of a percentage with regard to the simulation of the undisturbed flow. It should be pointed out that, for the experiments for which the chimney is simulated in the middle (see variable a_1 in Figure 2.11), the wind direction θ has been varied up to 180° due to the symmetry conditions. In that way, the results obtained for $180° < \theta < 360°$ have been mirrored.

For a complete overview of the results provided by the simulation, see Clobes u. a. [2012a].

3.3.1 Cubic building

Due to the vortex separation on the corner of the building, the increase on the turbulence grade has been shown in Figure 2.14 and Figure 2.15 for any wind direction. Figure 3.6 summarizes the influence of the interference effect depending on the wind direction.

For a better description of the position of the chimney, position 1 is defined for the chimney located in the corner and position 2 for the middle (see Figure 2.11). In Figure 3.6(a) Figure 3.6(b), the deformations for all wind directions are shown. In the case of position 1 a sharp maximum value is located for an angle of $\theta = 15°$ with an increase of 13%. This is 5% more than its neighbouring angles $\theta = 0°$ and $\theta = 30°$. For position 2, Figure 3.6(b) shows four peaks at $\theta = 15°$, 45°, 90° and 165° with increases between 6% and 9%. The minima on this plot are at $\theta = 30°$,60°,120° and 180° with values between 2% and 4%.

In Figure 3.6(c) and Figure 3.6(d), the results for the maximum bending moment M_y at the support are depicted. The increase varies for position 1 from -2% to 12% and, for position 2, from 4 to 11%.

Finally, Figure 3.6(e) and Figure 3.6(f) show the increase of the lateral force F_x. In case of position 1, the results are shown in Figure 3.6(e). The differences vary from a 3% decrease at $\theta = 210°$ to 20% of increase at $\theta = 15°$. For the position 2, Figure 3.6(f), it fluctuates from a minimum of 2% at $\theta = 60°$ to a maximum of 14% at $\theta = 15°$ and $\theta = 90°$.

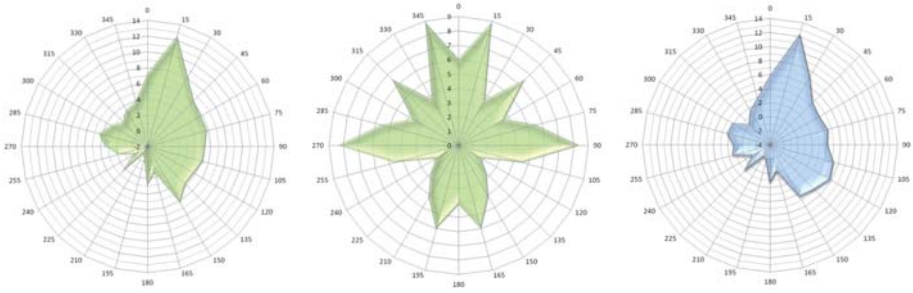

(a) Tip displacement. Position 1 (b) Tip displacement. Position 2 (c) Moment M_y. Position 1

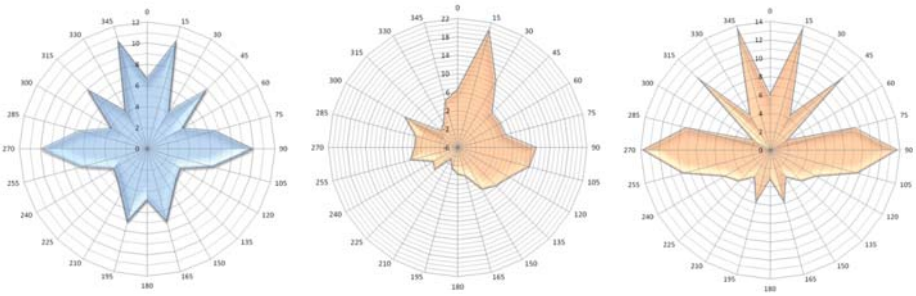

(d) Moment M_y. Position 2 (e) Lateral force F_x. Position 1 (f) Lateral force F_x. Position 2

Figure 3.6: [%] of changes for the cubic building depending on the wind direction θ

3.3.2 Rectangular building

Regarding these two types of buildings, the results do not produce spectacular results. In the case of the rectangular building, it is important to note that due to blockage problems during the wind tunnel tests, the selected height of the model was 15 cm, see Figure 2.11. That means that the nearby building has a height of 45 m in full scale. The ratio between

the cantilevered lenght $H^*$of the chimney (105 m) and the height of building h (45 m) seems to have an influence on the increase of the moments and forces at the support. This suspicion will be later confirmed in the new design approach for propped chimneys proposed in the following sections. The physical argument lies in the effective height over the building for which the perturbance of the flow remains. If the chimney is slender enough, the higher the ratio H^*/h, the lower the influence of the wind perturbation on the resulting forces.

For the rectangular building, the relative increase of displacements of the top of the chimney, bending moments and lateral forces are lower than those presented by the cubic building due to the reason given above. For a rectangular building, the results regarding the bending moment M_y at the support are shown in Figure 3.7(a). An increase of about 5% can be observed for a wind direction of $\theta = 30°$.

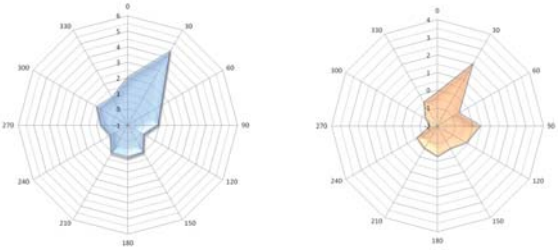

(a) Bending moment M_y. (b) Lateral force F_x

Figure 3.7: [%] of changes for the rectangular building shape depending on the wind direction θ for position 1

4 High frequency force balance measurements

The results of the numerical simulations are calculated using the quasi-steady theory for the aerodynamic wind loading. In quasi-steady theory, it is assumed that the wind forces are proportional to the pressure of the incoming flow. In reality, that assumption is not fulfilled and the aerodynamic admittance function should be taken into account.

In this chapter, dynamic measurements on a chimney model using the HFFB technique are shown. A carbon fiber cylinder has been used to simulate the dynamic response of an industrial chimney to wind buffeting. The main goal of the tests is the experimental identification of the aerodynamic admittance function $|\chi(f)|^2$ of the chimney. It is also necessary to know, if the interference effect provokes important changes in the aerodynamic admittance function having an influence on the design methodology of this kind of structures.

Before the measurements were carried out, some important aspects have been taken into account. In case of performing aerodynamic or aeroelastic measurements with circular bodies, the drag coefficient C_D is a parameter that has to be adjusted to the full scale situation if the buffeting wind loading will be studied. Therefore, an equivalence of C_D between full scale and wind tunnel is necessary despite the large differences in the Reynolds number between wind tunnel and full scale situations.

In the following chapter a short introduction to the physical concept of the aerodynamic admittance function is provided. Different formulations proposed in the literature during the last decades for the mathematical description of $|\chi(f)|^2$ are given and compared. As shown, this function can be identified from full scale measurements, as well as from wind tunnel experiments.

The procedure for the empirical determination of the aerodynamic admittance function under interference conditions will be described. For this purpose, the set of experiments carried out in the BLWT using the stiff chimney model and presented in Section 4.2 have been evaluated.

4.1 Searching for a wind flow equivalence

The aim of the wind tunnel experiments described here is the simulation of the atmospheric wind forces acting on industrial chimneys. For a comprehensive study, it is necessary to pay attention to some physical characteristics of the flow which should be taken into account during the simulation. The air density ρ is the mass per volume unit of the atmospheric air. Its value decreases with increasing altitude and depends on the temperature and humidity. The value recommended in the Eurocode 1 is 1.25 kg/m^3. The kinematic viscosity ν^* is the ratio of the dynamic viscosity μ and the density of the fluid ρ. It can be considered as the mass that relates the inertial forces to viscous forces. In case of air, a value of $\nu^* = 15 \cdot 10^{-6}$ m^2/s can be assumed.

The performance of fluids is normally described as laminar or turbulent. For the former, the movement of the fluid particles follows a straight trajectory. However, in a turbulent flow, an exchange of fluid particles between fluid lines occurs. This chaos provokes an alteration on the velocity of the flow. For the evaluation of the flow characteristics, some specific values are used in fluid dynamics. One of them is the Reynolds number Re, which relates the inertial forces to the internal viscous forces of a fluid. Therefore, the laminar conditions occur at low Reynolds numbers, where viscous forces are dominant with a constant fluid motion. On the other hand, a turbulent flow is generated at high Reynolds numbers producing a chaotic movement of particles. A fluid moving across a circular body, such as a chimney, can be described in terms of the Reynolds number using the following expression

$$\mathrm{Re} = \frac{D_{ext} \cdot \bar{U}}{\nu^*} \tag{4.1}$$

where D_{ext} is the external diameter of the body and $\bar{U}$ the velocity of the fluid. The Reynolds number is also a fundamental parameter to describe the distribution of the wind pressure over the surface of the body. Therefore, for dynamic force measurements in a wind tunnel, the real performance of the flow over the surface of the model has to be correctly imitated.

4.1.1 Reynolds number effect

In the same way as the atmospheric wind behaves on the surface of the Earth, a small boundary layer appears on the surface of the body due the frictional forces. Both the flow conditions and the roughness of the body influence the development of the boundary layer on the surface. Although initially the boundary layer is laminar, a transformation into a turbulent boundary layer can occur along the body's surface. If the roughness

grade is high, this transformation occurs faster. While for sharp edge bodies the flow-body separation takes place always at the edges, in the case of rounded aerodynamic geometries, a variable separation point appears. When the boundary layer travels along the circular body, an adverse pressure gradient acts on the boundary layer and helps the initial frictional forces to reduce their relative speed almost to zero, see Figure 4.1. The separation point is defined as the point between the forward and backward flow, where the shear stress is equal to zero. The air flow becomes detached from the surface of the cylinder in form of vortices, and if the separation follows is stable, a Kàrmàn vortex street may be generated.

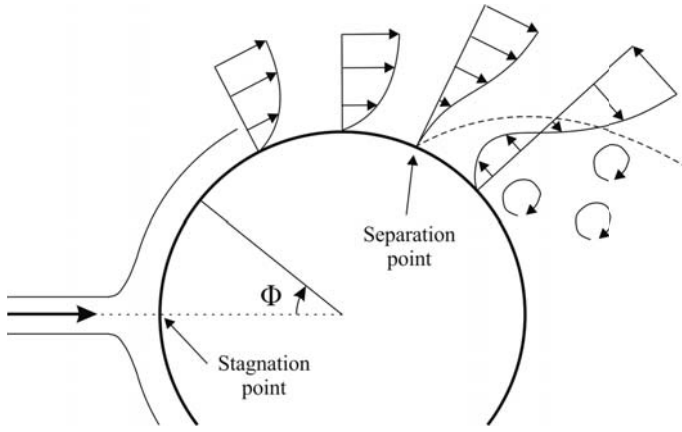

Figure 4.1: Flow separation point on a circular body

The flow separation point has a huge importance for the drag coefficient C_D of the body, increasing or decreasing its value due to the pressure differences between front and rear parts (Wagner [2010]). Therefore, the drag coefficient C_D is independent of the Reynolds number if the edges are sharp and strongly dependent if the edges are only slightly rounded.

According to Sockel [1984] and Dyrbye u. Hansen [1997], in case of a laminar incident flow on a smooth circular surface, four principal regimes of evolving flow can be identified, depending on the Reynolds number Re :

- Laminar regime: For a low Reynolds number (Re $<$ 200), the flow field remains laminar without any alteration of the flow lines. There is no separation point an there is no pressure drag due to pressure differences between the front and back side of the cylinder. The cylinder experiences only viscous drag due to the air friction.

- Subcritical regime: When the Reynolds number increases (Re up to 10^5), the boundary layer flow is still laminar and separates at about 80° from the stagnation point. Pairs of vortices are formed in the wake. Therefore, a vortex shedding appears and the streamwise length of the vortices increases linearly with the Reynolds number. This is a typical range in case of small diameters D_{ext} or low incident wind velocities $\bar{U}$. The drag coefficient in this range is characterized by $C_D = 1.2$.

- Supercritical regime: Between the critical Reynolds number $\mathrm{Re}_{crit} = 3 \cdot 10^5$ and Re $= 3 \cdot 10^6$. The critical Reynolds number can be defined as the value at which the boundary layer changes from laminar to turbulent (Niemann u. Hölscher [1990]). A separation point appears on the windward side being it in laminar conditions, but only for a short distance, as the flow then land again on the surface. Behind this, the separation points are located on the leeward side and the turbulent wake becomes much narrower. The drag coefficient C_D can drop to 0.22.

- Ultracritical regime: Also know as transcritical or postcritical regime. Above Re $> 3 \cdot 10^6$, the boundary layer flow at the cylinder surface is fully turbulent and the separation point varies between 100° and 110° from the stagnation point. The Kàrmàn vortices reappear and the wake is wider than the supercritical range but narrower than the subcritical regime. The drag coefficient increases again up to a typical range of $0.5 < C_D < 0.9$. Full scale chimneys are normally located in this range.

Due to the above presented differences, the influence of the Reynolds number on a round model is relevant for wind-tunnel tests. Normally, the kinematic viscosity ν^* is the same in the full scale and during the wind tunnel test. If the wind force acts on a 150 m high and 6 m wide chimney, the transformation of scale in the wind tunnel, according to the eq. 4.1, a geometrical scale of $\lambda_L = 1 : 300$ and a reference wind speed inside the wind tunnel of $\bar{U} \approx 12.5$ m/s, the obtained value is about $\mathrm{Re}_{\text{wind tunnel}} \approx 1.6 \cdot 10^4$. Comparing this value with the full scale situation, where at 150 m heigh a wind speed of 39 m/s is calculated, the Reynolds number increases up to $\mathrm{Re}_{\text{full scale}} \approx 1.6 \cdot 10^7$. This huge difference between both Reynolds numbers can be solved if the blower of the wind tunnel produces a wind speed of 10,000 m/s, which is out of question. Consequently, it should be accepted that the Reynolds model law cannot be fulfilled inside a wind tunnel due to the scale effects. Therefore, the only solution is to simulate flow features which imitate the turbulent boundary layer at high Reynolds numbers by adding roughness on the model's surface.

4.1.2 Determination of the drag coefficient

The aim of the experiments is graphically described in Figure 4.2. The flow condition represented in point A for a smooth cylinder and smooth flow is equivalent to the point B, which correspond to a rough cylinder with turbulent flow but for much lower Reynolds number.

In the following subsection an experimental set is presented with the aim of figuring out what type of roughness is the most appropriate in simulating at low Re values the same mean and fluctuating forces observed on a smooth 6 m wide chimney in the ultracritical regime. An equivalent definition is given in the right part of Figure 4.2 according to Niemann u. Hölscher [1990].

According to the guidance given in ESDU 80025 for the determination of the drag coefficient of a circular cylindrical structure, a calculation of a two-dimensional cylinder drag coefficient C_{D0} for laminar flow conditions is necessary at first. End effects, which induce a three dimensional flow at the tip could appear and hence, the cylinder should be tested placing it between end plates, minimizing this effect.

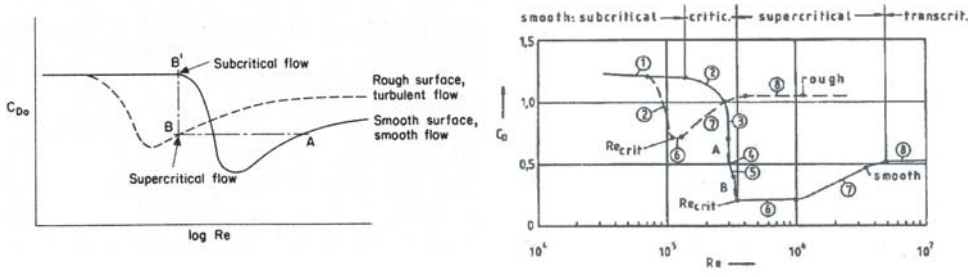

Figure 4.2: Aim of the simulation after ESDU 80025 and Niemann u. Hölscher [1990]

The method of ESDU is based on tables and figures, and it is useful for the calculation of mean forces induced by the flow around a cylindrical structure of circular cross-section. The determination of C_{D0} depends not only on the Reynolds numbers and surface roughness but also on the cylinder inclination in relation to the flow direction or turbulence grade of the incoming flow.

Table 4.1 shows the process for the determination of C_{D0}. The effective Reynolds number ($\mathrm{Re}_{eq} = \lambda_R \cdot \lambda_t \cdot \mathrm{Re}$) incorporates the influence of the surface roughness (λ_R) and the turbulence of the incoming flow (λ_t). The calculated flow conditions correspond to a 6 m wide and 150 m height uncoated steel ($\epsilon = 3 \cdot 10^{-3}$) chimney for a gusty wind of 38

Table 4.1: Determination of the mean drag coefficient C_{D0} of a two-dimensional cylinder ESDU 80025

ϵ	ϵ/D_{ext}	λ_R	λ_t	Re_{eq}	C_{D0}
$3 \cdot 10^{-3}$	$5 \cdot 10^{-4}$	1.27	1	$2.032 \cdot 10^{7}$	$0.72 < C_{D0} < 0.84$

m/s at chimney's tip. As expected, the obtained drag coefficient shows more sensitivity to the surface roughness than to the turbulence grade flow. ESDU doesn't give a fixed drag, but a range and it will be used as target value for the wind tunnel simulations.

For the determination of the two dimensional drag coefficient C_{D0}, wind tunnel tests under laminar flow have been carried out. For this purpose, the roughness elements and vortex generators installed in the wind tunnel for the simulation of the atmospheric boundary layer were removed. Figure 4.3 depicts the mean wind speed and turbulence intensity profile for laminar conditions at test section 2 along the model's height. Although there is an absence of roughness elements, a intern boundary layer appears.

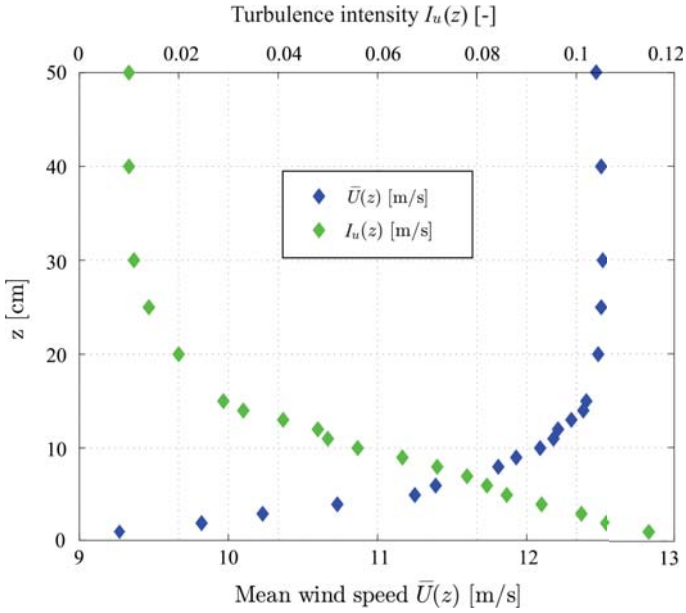

Figure 4.3: Mean wind speed and turbulence intensity for simulated laminar flow conditions

The height of the laminar boundary layer is much lower than the turbulent one; nonetheless, it should be taken into account for the calculation. For a precise calculation of the drag coefficient, a large number of measuring points have been considered along the the boundary layer. The convergence of the mean wind speed profile is faster than for the turbulence intensity (≈ 15 cm vs. ≈ 30 cm).

Figure 4.4(a) depicts schematically the measurement process for the determination of the drag force F_x acting on the chimney. The cylinder is made of carbon fiber and it is rigidly connected to the high frequency force balance. The model has a length of 500 mm with a diameter of 20 mm. The duration of each measurement was 120 seconds after completion of the transient period of acceleration of the flow. Even for laminar flow conditions, the fluctuations of the wind are not as significant as a turbulent flow, thus a sampling rate $2,000$ Hz was chosen. Although the ratio H/D of the model is 25 and it could be considered as sufficiently large for a two dimensional model according to ESDU 80025, the three dimensional flow around the tip has been blocked using an end plate simulating an infinity slenderness, see Figure 4.4(b).

The formulation for the calculation of C_{D0} is represented in eq. 4.2. It can be obtained from the measurements of the mean drag force $\bar{F}_x$ in wind direction, as well as from the mean bending moment $\bar{M}_y$:

$$
\begin{aligned}
C_{D0} &= \frac{\bar{F}_x}{\frac{\rho}{2} \cdot \sum_{i=1}^{n} \bar{U}^2(z_i) \cdot D \cdot L_i} \\
C_{D0} &= \frac{\bar{M}_y}{\frac{\rho}{2} \cdot \sum_{i=1}^{n} \bar{U}^2(z_i) \cdot z_i \cdot D \cdot L_i}
\end{aligned}
\tag{4.2}
$$

where L_i is the length of the element associated to the mean wind speed value $\bar{U}^2(z_i)$ measured with the Cobra Probe at height z_i. It is important to note, that z_i has to be considered from the geometrical middle of the piezo transducers of the HFFB. The value of ρ was individually calculated during the wind tunnel tests.

A large number of wind tunnel simulations have been carried out for the determination of the drag coefficient of the chimney. The starting point of the investigation is the calculation of the nominal value C_{D0} in smooth conditions. In a next step, following the recommendations given in the literature, the roughness of the model's surface has been varied. For this purpose, two types of external roughness have been added to the surface: randomly distributed roughness and one-dimensional orderly roughness (spanwise ribs

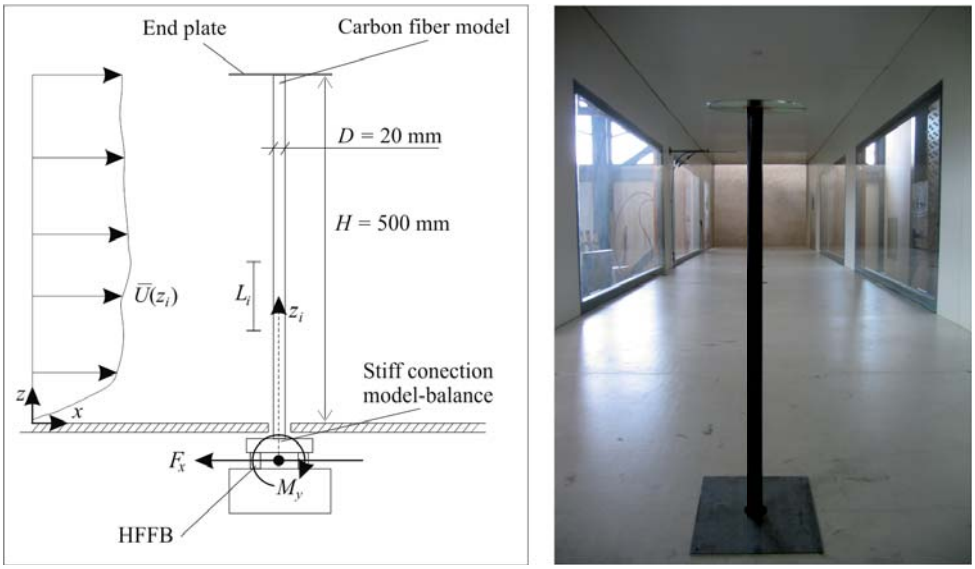

Figure 4.4: Schematic view of the measurement procedure (a) and simulation of the two dimensional conditions for the smooth cylinder (b)

made of brass). Table 4.2 presents a compilation of wind tunnel tests presented in the literature for the determination of the drag coefficient C_{D0} for low turbulence conditions. The results obtained for the current work are listed at the bottom of the table. The table is divided in five variables: Re, the external diameter of the model used D_{ext}, the roughness ratio k_s/D_{ext} where k_s is defined as the roughness height, the rib ratio k_r/D_{ext} where k_r is the diameter of the rib and Φ is the angle in degrees with respect to the stagnation point (see Figure 4.1).

Barre u. Barnaud [1995] present a set of wind tunnel experiments for high and medium Reynolds numbers dividing the study in two different wind tunnels. The climatic wind tunnel accelerates the wind speed up to 80 m/s producing large Reynolds numbers. Using a 800 mm wide cylinder, drag coefficients of $C_{D0} = 0.53$ and $C_{D0} = 0.76$ have been measured for smooth and rough surface, respectively. On a second step, the atmospheric wind tunnel is used reducing the model's diameter to 140 mm. The flow turbulence is 1% and the mean wind speed varies between $\bar{U} = 13$ and 25 m/s. Rough patches are put along the cylinder with a 15° step. For a roughness ratio of $k_s/D_{ext} = 3.5 \cdot 10^{-3}$ a drag coefficient of 0.76 is obtained.

Batham [1973] carried out wind tunnel experiments to calculate the mean and fluctuating pressure distributions on long circular cylinders. Measurements were tested for two different Reynolds number, having a smooth and rough surfaces. The mean drag coefficient was determined by integration of the mean pressure distribution. A large reduction of C_{D0} is observed for low Reynolds number adding 0.5 mm diameter sand particles over the surface. Other experiments in turbulent flow were also reported in the paper, but they are not included in Table 4.2.

The dimensions of the model presented by Buresti [1981] are in quite concordance with the external diameter D_{ext} used in the current study. The aim of this work is to assess the influence of the surface roughness on the transitions between the different ranges. Interesting observations are made varying the model's diameter and surface roughness. The grade of turbulence obtained in the atmospheric wind tunnel of the University of Pisa for laminar flow conditions ($I_u = 0.9\%$) is equivalent to that of the TU Braunschweig. The variation of the C_{D0} are located in the range observed in the current work.

Eaddy u. Melbourne [2011] present a set of wind tunnel tests at the Monash University aimed at increasing the knowledge of drag forces experienced by a smooth and rough two-dimensional circular cylinders with varying turbulence. From the set of experiments, those with low turbulence ($I_u = 4\%$) are summarized on Table 4.2. The dimensions of the models are considerably larger ($D_{ext} = 400 - 630$ mm) generating higher Reynolds numbers. Contrary to the other results presented, the increase of the roughness makes the drag coefficient larger due to the high Reynolds range where the experiments are located (transition super- to ultracritical regime). At sufficient high Re, the drag coefficient C_{D0} becomes independent of Reynolds, depending only on the roughness ratio.

Ribeiro [1991] presents within the frame of an experimental program the results of a parametric study to determine the influence of different roughness types on the wind forces acting on a circular body at low Reynolds numbers. For this purpose, he changes the surface roughness using sand paper, wire screen and span wise ribs. The circular cylinder has a constant diameter of 147 mm, obtaining a constant Reynolds number of $\mathrm{Re} = 3.8 \cdot 10^5$ after verifying of the simulation of the ultracritical regime. The turbulence intensity during the test is constant, defined with a value $I_u = 0.5\%$. Four different roughness heights are tested for each roughness configuration. The author concludes that the use of spanwise ribs produces the best results for the simulation of the ultracritical conditions. These localized roughness types are uniformly distributed every 15° around the perimeter of the model. Despite this, he noted that for simulations with turbulent flow this conclusion could be contrariwise due to the high dependency of the ribs on the angle of incidence. Therefore, from his point of view, the use of constant roughness is the best practical solution in such cases.

Schümmer [2003] presents in her Master's thesis a comprehensive research project about the simulation of ultracritical regime flow characteristics around circular bodies varying both turbulence and roughness simultaneously. On Table 4.2 are the results only for low turbulence summarized ($I_u \approx 5\%$). The experiments are carried out in the atmospheric boundary layer of the RWTH Aachen using a 110 mm wide plexiglas cylinder. The drag coefficients using spanwise ribs drop more than for uniform roughness.

Finally, Spaethe u. Trätner [1992] present a research project aimed at answering the uncertainties about the reasons behind the crash of a 150 m high steel chimney in the power plant of Boxberg. Althought the principal goal is to simulate the vortex shedding in cylinders in groups, unique cylindrical models are tested in the wind tunnel and their drag coefficient is calculated for ultracritical flow conditions. Two different diameters are used together with a 15 mm wide uniform roughness (but in this case located at $\Phi = 54°$). Ribs are also tested here. The latter produces the lowest drag coefficients.

Table 4.2: Compilation of drag coefficients C_{D0} from low turbulence wind tunnel tests (D_{ext} in [mm])

Author	Re	D_{ext}	k_s/D_{ext}	$k_r/D_{ext}(\Phi°)$	C_{D0}
Barre u. Barnaud [1995]	$3.6 \cdot 10^6$	800	smooth	no ribs	0.53
	$3.6 \cdot 10^6$	800	$1 \cdot 10^{-4}$	no ribs	0.76
	$1.21 - 2.33 \cdot 10^5$	140	$3.5 \cdot 10^{-3}$ (each 15°)	no ribs	0.74
Batham [1973]	$1.11 \cdot 10^5$	230	smooth	no ribs	1.17
	$2.39 \cdot 10^5$	230	smooth	no ribs	0.78
	$1.11 \cdot 10^5$	230	$2.17 \cdot 10^{-3}$	no ribs	0.72
	$2.35 \cdot 10^5$	230	$2.17 \cdot 10^{-3}$	no ribs	0.71
Buresti [1981]	$0.48 - 1.9 \cdot 10^5$	61	$1.77 \cdot 10^{-3}$	no ribs	1.20-0.72
	$0.48 - 1.9 \cdot 10^5$	61	$2.97 \cdot 10^{-3}$	no ribs	1.15-0.67
	$0.48 - 1.9 \cdot 10^5$	61	$4.10 \cdot 10^{-3}$	no ribs	1.08-0.72
	$0.48 - 1.9 \cdot 10^5$	61	$6.89 \cdot 10^{-3}$	no ribs	1.05-0.85
	$2.5 - 8.5 \cdot 10^4$	34	$5.32 \cdot 10^{-3}$	no ribs	1.18-0.85
	$2.5 - 8.5 \cdot 10^4$	34	$7.35 \cdot 10^{-3}$	no ribs	1.17-0.93

Table 4.2: Compilation of drag coefficients C_{D0} from low turbulence wind tunnel tests (D_{ext} in [mm])

Author	Re	D_{ext}	k_s/D_{ext}	$k_r/D_{ext}(\Phi°)$	C_{D0}
	$2.5 - 8.5 \cdot 10^4$	34	$1.23 \cdot 10^{-2}$	no ribs	1.17-1.00
Eaddy u. Melbourne [2011]	$2 - 9 \cdot 10^5$	400	smooth	no ribs	0.28-0.52
	$2 - 9 \cdot 10^5$	400	$0.8 \cdot 10^{-3}$	no ribs	0.65-0.96
	$2 - 9 \cdot 10^5$	400	$2 \cdot 10^{-3}$	no ribs	0.88-1.04
	$4.5 - 13.6 \cdot 10^5$	630	smooth	no ribs	0.40-0.56
	$4.5 - 13.6 \cdot 10^5$	630	$0.8 \cdot 10^{-3}$	no ribs	0.92-1.02
	$4.5 - 13.6 \cdot 10^5$	630	$2 \cdot 10^{-3}$	no ribs	1.08-1.12
Ribeiro [1991]	$3.8 \cdot 10^5$	147	$1.8 \cdot 10^{-3}$	no ribs	0.87
	$3.8 \cdot 10^5$	147	$4.14 \cdot 10^{-3}$	no ribs	0.94
	$3.8 \cdot 10^5$	147	$6.99 \cdot 10^{-3}$	no ribs	0.97
	$3.8 \cdot 10^5$	147	$1.12 \cdot 10^{-2}$	no ribs	0.99
	$3.8 \cdot 10^5$	147	smooth	$2.3 \cdot 10^{-3}$ (wire mesh)	0.96
	$3.8 \cdot 10^5$	147	smooth	$4.1 \cdot 10^{-3}$ (wire mesh)	0.99
	$3.8 \cdot 10^5$	147	smooth	$7.0 \cdot 10^{-3}$ (wire mesh)	1.03
	$3.8 \cdot 10^5$	147	smooth	$1.22 \cdot 10^{-2}$ (wire mesh)	1.09
	$3.8 \cdot 10^5$	147	smooth	$2.05 \cdot 10^{-3}$ (each 15°)	0.78
	$3.8 \cdot 10^5$	147	smooth	$4.11 \cdot 10^{-3}$ (each 15°)	0.81
	$3.8 \cdot 10^5$	147	smooth	$6.85 \cdot 10^{-3}$ (each 15°)	0.86

Table 4.2: Compilation of drag coefficients C_{D0} from low turbulence wind tunnel tests (D_{ext} in [mm])

Author	Re	D_{ext}	k_s/D_{ext}	$k_r/D_{ext}(\Phi°)$	C_{D0}
	$3.8 \cdot 10^5$	147	smooth	$1.23 \cdot 10^{-2}$ (each 15°)	0.94
Schümmer [2003]	$3.74 - 7.41 \cdot 10^4$	110	smooth	no ribs	0.84-0.8 0
	$3.74 - 7.41 \cdot 10^4$	110	sandblasted	no ribs	0.82-0.74
	$3.74 - 7.41 \cdot 10^4$	110	$2.30 \cdot 10^{-4}$	no ribs	0.93-0.67
	$3.74 - 7.41 \cdot 10^4$	110	$2.88 \cdot 10^{-4}$	no ribs	0.80-0.79
	$3.74 - 7.41 \cdot 10^4$	110	$3.85 \cdot 10^{-4}$	no ribs	0.78-0.85
	$3.74 - 7.41 \cdot 10^4$	110	smooth	$4.54 \cdot 10^{-3}$ (each 22.5°)	0.76-0.71
	$3.74 - 7.41 \cdot 10^4$	110	smooth	$9.09 \cdot 10^{-3}$ (each 22.5°)	0.70-0.85
	$3.74 - 7.41 \cdot 10^4$	110	smooth	$9.09 \cdot 10^{-3}$ (each 11.25°)	0.74-0.80
	$3.74 - 7.41 \cdot 10^4$	110	smooth	$9.09 \cdot 10^{-3}$ (each 7.5°)	0.75-0.74
	$3.74 - 7.41 \cdot 10^4$	110	smooth	$4.54 \cdot 10^{-3}$ (each 65°)	0.75-0.74
Spaethe u. Trätner [1992]	$1.04 - 5.37 \cdot 10^5$	127.6	smooth	no ribs	$1.2 - 0.43$
	$1.04 \cdot 10^5$	127.6	$2.3 \cdot 10^{-3}$	no ribs	1.02
	$8.2 \cdot 10^4$	110	smooth	0.022 (n.d.)	$0.55 - 0.45$
Aizpurua Aldasoro	$1.66 \cdot 10^4$	20	smooth	no ribs	1.06
	$1.7 \cdot 10^4$	20.5	$12.5 \cdot 10^{-3}$	no ribs	1.08
	$1.73 \cdot 10^4$	20.8	$20 \cdot 10^{-3}$	no ribs	1.15
	$1.75 \cdot 10^4$	21	$25 \cdot 10^{-3}$	no ribs	1.04
	$1.8 \cdot 10^4$	21.6	$40 \cdot 10^{-3}$	no ribs	1.08

Table 4.2: Compilation of drag coefficients C_{D0} from low turbulence wind tunnel tests (D_{ext} in [mm])

Author	Re	D_{ext}	k_s/D_{ext}	$k_r/D_{ext}(\Phi°)$	C_{D0}
	$1.8 \cdot 10^4$	21.7	$42.5 \cdot 10^{-3}$	no ribs	1.12
	$1.91 \cdot 10^4$	23	$75 \cdot 10^{-3}$	no ribs	0.79
	$1.66 \cdot 10^4$	20	smooth	$25 \cdot 10^{-3}(50°)$	0.85
	$1.66 \cdot 10^4$	20	smooth	$4 \cdot 10^{-3}(65°)$	1.25

The starting value was $C_{D0} = 1.06$, lightly under the value of 1.2 given in the Eurocode at low Reynolds numbers but in concordance with the results presented by Wieselsberger u. Betz [1923], Fage u. Warsap [1929] and Schewe [1983] on smooth cylinders for the same Reynolds range (not presented on Table 4.2). It has been noted that there are problems to obtain from the literature drag coefficients of smooth cylinders at Reynolds numbers around 10^4. After this first step, several grades of roughness were systematically added on the surface of the carbon fiber model. The roughness materials used in this experimental set are of diverse origins, such as sand-, wrapping- or corrugated papers. Note that the increase of roughness provokes an increase of the model's diameter, which influences the Reynolds number. The results show a fluctuation of the drag coefficient for an increasing grade of the roughness without defined trend. Despite this, the configuration with the roughness ratio $k_s/D_{ext} = 75 \cdot 10^{-3}$ induces a steep drop on the drag value up to 0.79, which coincides very well with the target range obtained using ESDU 80025 (see Table 4.1). Figure 4.5(a) shows this last roughness configuration in form of corrugated paper. Besides uniform roughness, discrete spanwise ribs situated in a longitudinal way along the model where also used. For a 0.5 mm thick brass wire situated at $\Phi = 50°$, see Figure 4.5(b), a significant reduction of C_{D0} up to 0.85 was observed.

The above presented results are only an approximation of the reality due to the idealization of flow and boundary conditions. A steel chimney situated in the outskirts of a city should not be only considered as a two dimensional cylinder under uniform laminar flow. The chimney has a finite length and that's why end effects occur, thus changing the overall drag coefficient. Hence an atmospheric boundary layer could not be considered as a uniform constant flow acting on the cylinder and therefore, the influence of the shear flow has to be also taken into account.

As explained in ESDU 81017, the drag coefficient is larger when the free end of the chimney is not closed. However, the effect of the efflux from the open end is to decrease the drag coefficient up to one in case of a closed end. This counterbalance increases with the slenderness of the body. Therefore, for a 150 m height and 6 m wide chimney and

(a) selected roughness - corrugated paper (b) two spanwise ribs - brass

Figure 4.5: The selected paper (a) and two 0.5 mm diameter spanwise ribs (b)

Table 4.3: Determination of the mean drag coefficient C_D of a finite cylinder in shear flow ESDU 81017

C_{D0}	H/D_{ext}	f_H	f_S	C_D
$0.72 < C_{D0} < 0.84$	25	0.97	1	$0.70 < C_D < 0.82$

a ratio $H/D_{ext} = 25$, the end effect is quite small ($f_H = 0.97$) compared with a short stack. In a similar way, the influence of the wind gradient produced by the atmospheric boundary layer on the drag coefficient is negligible for structures with a high grade of slenderness ($f_S = 1$). For these new conditions, ESDU proposes a drag coefficient C_D defined as $C_D = f_H \cdot f_S \cdot C_{D0}$.

The last calculations are useful to check what range of drag coefficient should be selected as target values for a simulation in the wind tunnel. Although the influence of the end effect and velocity gradient is quite small for slender structures, a light reduction of the range has been produced regarding the ideal C_{D0}. The target drag coefficient is located between $0.70 < C_D < 0.82$. As explained above, the roughness type which has produced the lowest drag coefficient for two-dimensional conditions and laminar flow has been used for this second experimental set (see Figure 4.5(a)). The DVD used as end plate has been removed returning to a real situation. The turbulence generators and roughness elements have been inserted once again, simulating a terrain category II with the wind field characteristic described in Figure 2.7. The new value of drag coefficient registers a slightly modification up to $C_D = 0.81$ which coincides with the range proposed by ESDU and shown in Table 4.3.

The concluding remarks regarding the study about the simulation of a drag coefficient of the ultracritical regime at low Reynolds numbers has some interesting points. The first

one is the successfully identification of a roughness type (see Figure 4.5(a)), which allows the simulation of a mean force on a 500 mm height and 20 mm model equivalent to a 150 m height and 6 m wide uncoated steel chimney obtaining the given range of C_D by ESDU. In a first step, the drag coefficient calculated for a two-dimensional smooth cylinder in a subcritical regime coincides with the results given in the literature for equivalent low Reynolds numbers. The reduction of the drag adding roughness and ribs has shown a random performance without clear trends. It was not possible to find a roughness type to reduce the drag coefficient in the same scale as in the literature $(0.4 - 0.7)$. The small diameter of the model could be responsible for this, increasing the overall effect of the air viscosity on the simulated flow conditions. Buresti [1981] demonstrates this conjecture showing the difficulty, in case of small diameter models, to reduce in a large grade the drag coefficient up to full scale values.

This work includes also two new innovations regarding the actual literature. The first is the use of the HFFB technique to the identification of drag coefficients, obtaining its value using a integration of the mean wind speed profile along the height of the model. The majority of the works presented in the literature calculate C_D integrating the pressure values obtained with uniform distributed pressure tabs around the perimeter.

As stated in the introduction, in case of gust buffeting loading simulation, the drag coefficient is the principal parameter that has to be adjusted to the full scale situation. Other parameters as the separation point, pressure coefficients etc. are normally checked to validate the fulfilled simulation of the ultracritical regime flow characteristics at low Reynolds numbers. Unfortunately, due to geometrical limitations, the flow characteristics around the circular body can not be totally checked. One disadvantage of the small diameter of the model is the impossibility to introduce pressure tabs around the cylinder to determine the distribution of pressures and separation points around model's perimeter. This fact left some unanswered questions about the correct simulation of the fluctuating pressures in the ultracritical regime, but the obtained value of drag coefficient suggest a good tendency on the flow simulation. For all the above presented experiments, the influence of the Mach number or the integral length scale has not been considered.

Contrary to wind tunnel tests, full-scale measurements of drag coefficients are given in SPP [1981]. There, a large number of measurements carried out in real circular buildings and high masts are presented. The equivalence of the simulated drag coefficients in the wind tunnel are in this publication validated.

4.2 Study of the buffeting loading using HFFB

4.2.1 Measuring set-up

In order to determine the aerodynamic admittance function $|\chi(f)|^2$ under interference effect conditions, the same parametric study as shown in Figure 2.11 has been carried out. The along-wind force component F_x and bending moment M_y have been measured for each scenario.

Figure 4.6: HFFB experiments without interference effect (a) and considering a cubic building (b)

Figure 4.6 shows two different configurations of experiments. The left picture corresponds to the experiment in which the chimney alone was tested. In this experiment the absence of perturbation due to the presence of a nearby building has been established. On the other hand, Figure 4.6(b) depicts the configuration considering a cubic building, with the chimney located in the middle and wind direction $\theta = 0°$.

As explained in the previous section about the introduction to the high frequency force balance, the wind tunnel blower is activated five seconds after starting the data acquisition. After 20 seconds of flow acceleration, the stationary conditions are reached and remain stable for about 90 seconds. Finally, the blower is switched-off and the data acquisition stopped after the wind movement disappears inside the wind tunnel. Figure 4.7(a) shows an example of the data acquisition. The four vertical forces F_{zi} and the along-wind components F_{xi} are displayed as raw data. It includes the drift correction made to evaluate the data. The differences between both figures can be noted at the end of the acquisition process, for which the slope correction is carried out.

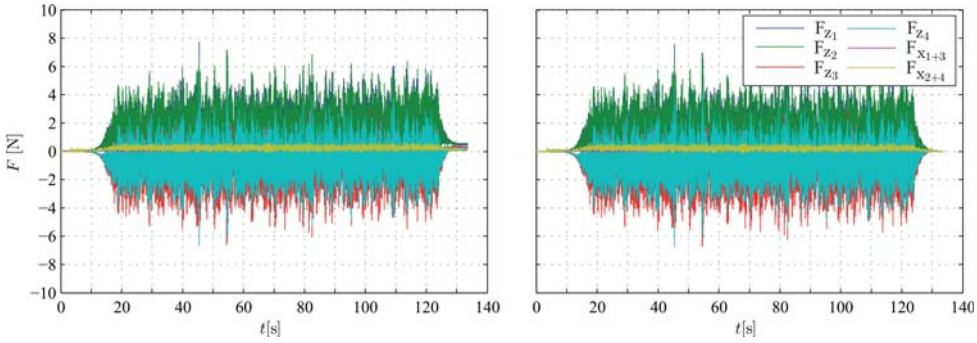

(a) Raw data before and after drift correction

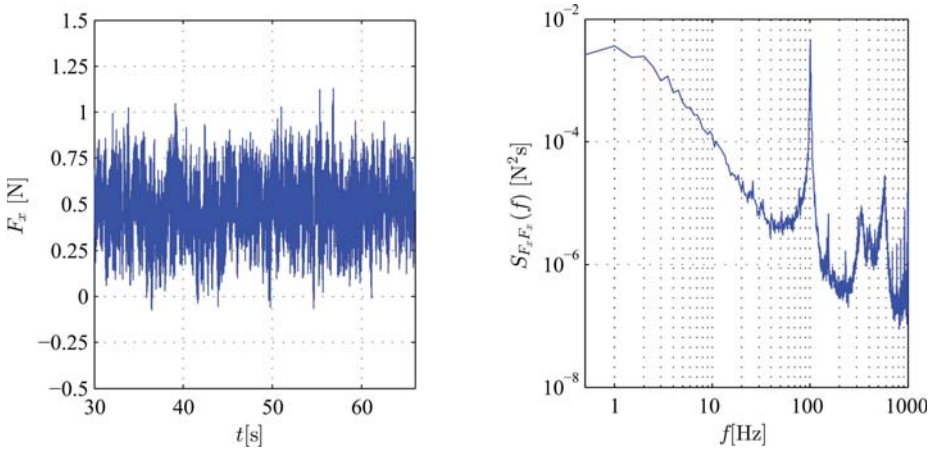

(b) Time series of F_x and its spectral density function S_{FxFx}

Figure 4.7: Set of data acquired using the HFFB

For the corrected data, a time window of 36 seconds from the stationary wind situation is selected to simulate a one hour long storm due to a $\lambda_T = 1:100$ time scale inside the wind tunnel. Figure 4.7(b) shows the time series of the along-wind force F_x. The plot corresponds to the configuration without building. Due to the shadowing effect produced by the building on the chimney, for the majority of wind angles θ, the mean force and moment are lower than the configuration without building. Nevertheless, there are some angles in which an opposite effect appears. For wind angles between $90° \leq \theta \leq 135°$ and $225° \leq \theta \leq 270°$ the mean forces and moments are higher than those without building. An important point is that the standard deviations of the measured force σ_{Fx} and moment σ_{My} are always higher than the configuration without building. The reason for that effect

can be related to the vortex shedding produced by the nearby building, thus affecting the chimney's response. Even for the situation with the chimney located windward, the presence of the building seems to modify the load field acting on the chimney. This last effect was also corroborated in the previously presented wind field measurements provided by the Cobra Probe. In addition, Figure 4.7(b) shows the power spectral density function of the along-wind forces $S_{FxFx}(f)$. It is calculated applying the same formula as in eq. 2.3. Due to the consideration of $F_x(t)$ as stationary ergodic processes, the power spectral density function can be obtained averaging the spectra calculated for short time windows of the same process. Finding a compromise between smoothing amplitudes and frequency resolution, a total of 4,000 samples of each time series have been considered for each selected time window having a 80 % overlap. This solution provides a frequency resolution of 0.5 Hz. It is important to note that this compromise has also been maintained during the calculation of $S_{uu}(z, f)$ because a future interaction between both spectra is necessary for the identification of the aerodynamic admittance function $|\chi(f)|^2$. The results are plotted in a logarithmic axis and the natural frequency of the chimney model f_0 can be clearly identified for $f_0 \approx 100$ Hz.

4.2.2 Mechanical characteristics of model and balance

In order to carry out HFFB measurements successfully, it is necessary to obtain the mechanical transfer function $|H(f)|^2_{m+b}$ of the balance and aerodynamic model simultaneously. The classical representation of this function in case of a SDOF system is:

$$|H(f)|^2 = \left[\left(1 - \left(\frac{f}{f_0} \right)^2 \right)^2 + 4 \cdot \xi^2 \cdot \left(\frac{f}{f_0} \right)^2 \right]^{-1} \tag{4.3}$$

where f_0 is the fundamental frequency of the system and ξ is the damping ratio ($\xi = \Lambda/2\pi$). For the identification of these variables, two different techniques have been used: the impact hammer technique and the pluck test.

The hammer technique is used to replicate a known impact to a structure. This impact produces an impulse with a very short duration. This causes a constant amplitude in the frequency domain and ideally provokes the excitation of all vibration modes of the structure. Actually, the impact produced by the hammer is not infinitely short in time by reducing the bandwidth, but during the strike duration, where the impact force of the

hammer and the resulting forces on the structure are recorded. Therefore, the transfer function is obtained as follows:

$$|H(f)| = \frac{|\breve{F}_{output}(f)|}{|\breve{F}_{input}(f)|} \tag{4.4}$$

where $\breve{F}_{input}$ and $\breve{F}_{output}$ are the one-sided spectra of amplitudes measured by the impact hammer and the HFFB, respectively. The spectrum of the amplitudes of the impulse signal or input is calculated as the modulus of the Fourier Transformation of the load $F_{hammer}(t)$ provided by the impact in wind direction x using the hammer:

$$|\breve{F}_{input}(f)| = 2 \cdot \sqrt{Re(\mathcal{F}(F_{hammer}(t)))^2 + Im(\mathcal{F}(F_{hammer}(t)))^2} \tag{4.5}$$

On the contrary, the spectrum of amplitudes of the response or output can be determined in a similar way using $F_x(t)$ in the HFFB as measured force:

$$|\breve{F}_{output}(f)| = 2 \cdot \sqrt{Re(\mathcal{F}(F_x(t)))^2 + Im(\mathcal{F}(F_x(t)))^2} \tag{4.6}$$

To excite different bandwidths, the hammer uses different types of materials for the impact point with different damping characteristics. The type of head can selected among the following: rubber, nylon and steel.

Figure 4.8: Impulse on the chimney

The fundamental frequency of the structure is located at the maximum of $|H(f)|$ for small damping cases. For the determination of the damping ratio ξ different proposals

are given in the literature. Clough u. Penzien [1993] propose a simple method to obtain ξ from the maximum value of the mechanical transfer function $|H(f)|_{max}$:

$$\xi \cong \frac{|H(f=0)|}{2 \cdot |H(f)|_{max}} \tag{4.7}$$

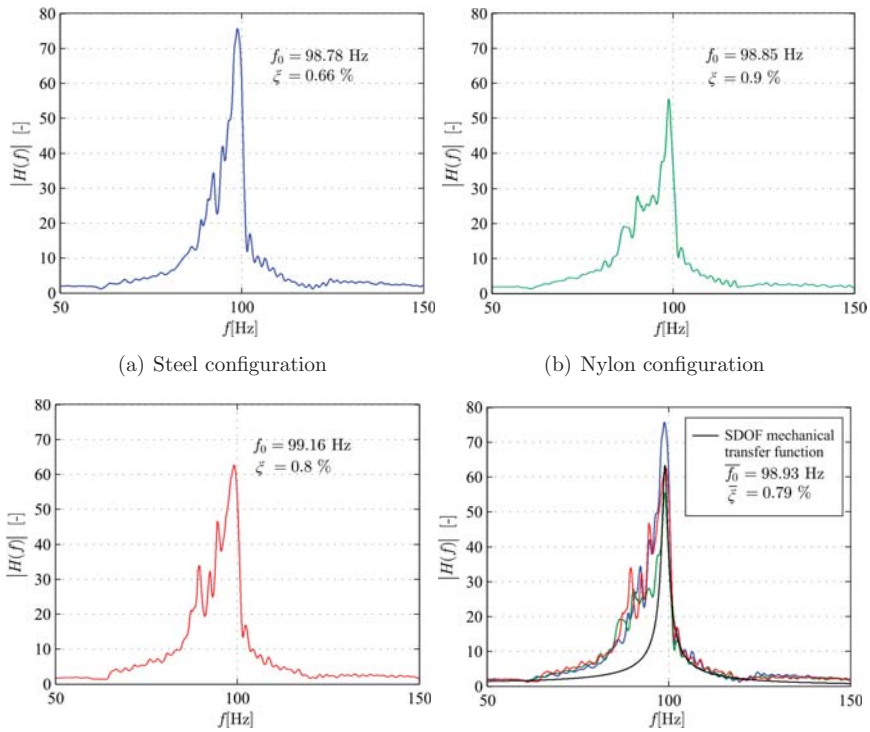

(a) Steel configuration

(b) Nylon configuration

(c) Rubber configuration

(d) Comparison with mean values

Figure 4.9: Mechanical transfer functions obtained from the impulse hammer

Figure 4.9 shows the results provided by the impulse hammer testing. The obtained fundamental frequency f_0 does not vary too much. On the contrary, the damping ratio ξ suffers a large variation and eq. 4.7 does not seem to be applicable for this work. Figure 4.9(d) compares the three types of materials with the classical formulation given in eq. 4.3 selecting the mean frequency and damping ratio of the three types of head.

The performance of the mean curve fits well with the decaying part from the fundamental frequency, but the ascent range does not fit with the experimental results.

In pluck tests, normally the fundamental frequency f_0 is excited. In this case, the following expression can be also applied to determine ξ (Clough u. Penzien [1993]):

$$\xi \cong \frac{f_2 - f_1}{f_2 + f_1} \tag{4.8}$$

This expression is an approximated solution to the half-power or band-width method whereby the damping ratio ξ is determined from the frequencies at which the response amplitude $|H(f)|$ is reduced to the level $1/\sqrt{2}$ times its maximum value $|H(f)|_{max}$. The frequencies f_1 and f_2 represent the frequencies at which the amplitudes of response equal $1/\sqrt{2}$ times the peak amplitude. In this case, a normalization of the transfer function with $|H(f = 0)|$ is not necessary.

Figure 4.10(a) shows the time series of the measured signal $M_y(t)$ after the deflection of the tip of the chimney for a time window of 2 seconds. Figure 4.10(b) shows the transfer function of the mechanical system. In absence of external forces, the assumption of a stiff model yields to consider the measured bending moment $M_y(t)$ proportional to the base rotation $\phi(t)$. the empirical determination of $|H(f)|$ obtained from the spectrum of amplitudes $|\hat{M}_y(f)|$ as follows:

$$|\hat{M}_y(f)| = |H(f)| \cdot M_{y,0} \tag{4.9}$$

The reference static value $M_{y,0}$ has been obtained after extrapolation of $|\hat{M}_y(f)|$ up to $f = 0$ Hz. Applying eq. 4.8, a damping ratio of $\xi = 0.37\%$ is obtained. The fundamental frequency is located at $f_0 = 100.67$ Hz. The green line represents the analytical solution SDOF system after eq. 4.3 using the identified values of f_0 and ξ. The width of the peak from the pluck tests is larger than the width obtained using eq. 4.3. Therefore, for the same half-power, the peak for a SDOF system is smaller than the real one.

The fundamental frequency of the chimney can be easily identified, but the obtained damping ratio of $\xi = 0.37\%$ seems to be not sufficient to apply eq. 4.3 without large errors. Due to the high sensitivity of this kind of tests to other parameters such as the time window, maximum initial deflection, sample rate etc., a large number of measurements has been carried out to adjust the values of f_0 and ξ as solidly as possible. A fundamental frequency of $f_0 = 100.8$ Hz of the chimney model has been found. To show the following results applying the classical mechanical transfer function $|H(f)|$, a $\xi = 0.8\%$ is used.

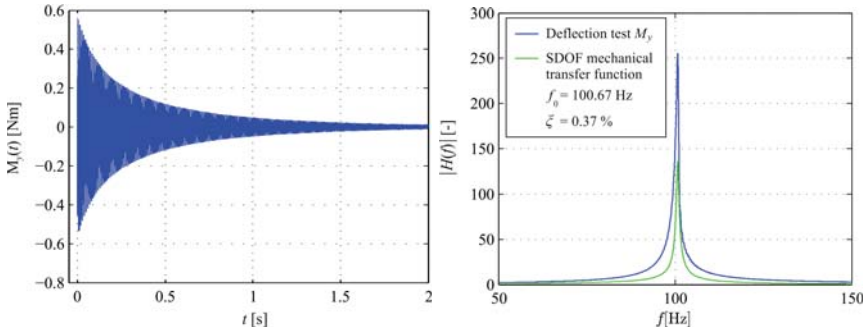

(a) Time serie $M_y(t)$ (b) Mechanical transfer function from $M_y(t)$

Figure 4.10: Mechanical transfer functions obtained from pluck test

4.3 Identification of the aerodynamic admittance function using the HFFB technique

The theoretical concept of the aerodynamic admittance function was initially introduced by Davenport [1962] to calculate analytically the response of a structure under gusty wind. This function can be physically defined as the step responsible for transforming the turbulence characteristics of the incoming flow into the resultant wind load over the structure. Davenport used the early studies made by Morison u. a. [1950] about the drag force of a flow:

$$F(t) = \frac{\rho}{2} \cdot A \cdot C_D \cdot u_{rel}^2(t) + \rho \cdot B^3 \cdot C_M \cdot \dot{u}_{rel}(t) \tag{4.10}$$

The semi-empirical equation is divided in two terms. The first describes the drag force proportional to the square of the instantaneous wind speed. The second describes the inertial force associated with the acceleration of the fluid. The coefficient C_M is named inertial coefficient and depends on the virtual air mass.

4.3.1 Frequency-dependent models for description of the aerodynamic admittance function

The relationship between wind speed and force expressed in eq. 4.10 in the time domain can be also expressed in the frequency domain in terms on power spectral density functions:

$$|\chi(f)|^2 = \frac{S_{ff}(f)}{(\rho \cdot A \cdot C_F \cdot \bar{U})^2 \cdot S_{uu}(f)} = 1 + \left(\frac{C_M(f)}{C_F(f)} \cdot 2\pi\right)^2 \cdot \left(\frac{f \cdot d}{\bar{U}}\right)^2 \tag{4.11}$$

If $C_M = C_F$ do not depend on the frequency f, then $|\chi(f)|^2$ would increase with increasing frequency, but experiments made by Davenport [1961] show the opposite. If a quasi-steady relationship between wind turbulence and wind pressures is assumed, the space correlation of the wind pressure is then identical to the space correlation of the wind turbulence. As stated in Newberry u. a. [1973], full scale measurements on building facades have shown that this assumption is not always true. In case of structures that cannot be considered as point-like structures, the reduced spatial correlation of the wind pressures over the surface has to be taken into account.

Vickery [1965] introduced the *lattice plate theory* to cover mathematically the lack of correlation of the eddies over a surface. The main idea is to divide the entire surface A into a finite number of surface elements dA, in which the wind fluctuations are perfectly correlated. Using the coherence function $\gamma_{ij}(f)$, it is possible to obtain a reduction factor $1/A^2 \int\int \gamma_{ij}(f) \cdot dA_1 \cdot dA_2$. Multiplying eq. 4.11 by this factor, the inertial effects and the correlation of the turbulent wind field is fully covered (Behrens [2004]).

In addition to this, Vickery carried out a parametric study in the wind tunnel to determine the aerodynamic admittance function experimentally. For this purpose, the fluctuating drag forces on a combination of plates and prisms with low aspect ratio are determined. He transferred the results obtained on bluff bodies to real lattice structures and proposed a relationship between $S_{uu}(f)$ and $S_{ff}(f)$ that depends on the dimension of the body D. As conclusion, Vickery proposed the following empirical formula:

$$|\chi(f)|^2 = \left(\frac{1}{1 + \left(\frac{2 \cdot f \cdot D}{U}\right)^{4/3}}\right)^2 \tag{4.12}$$

Vellozzi u. Cohen [1968] presented a mathematical expression for the determination of $|\chi(f)|^2$ which takes into account the lack of correlation of the pressures in the three directions of the space:

$$
\begin{aligned}
|\chi(f)|^2 &= R_x \cdot R_y \cdot R_z \\
|\chi(f)|^2 &= \left(\frac{1}{\zeta} - \frac{1}{2 \cdot \zeta^2}(1 - e^{-2\zeta})\right) \cdot \left(\frac{1}{\gamma} - \frac{1}{2 \cdot \gamma^2}(1 - e^{-2\gamma})\right) \cdot \left(\frac{1}{\mu} - \frac{1}{2 \cdot \mu^2}(1 - e^{-2\mu})\right)
\end{aligned}
\tag{4.13}
$$

where the coefficients ζ, γ and μ are the correlation factors which depend on the decay coefficients obtained from full scale measurements. The correlation factors in along-wind, across-wind and vertical direction are defined as follows, respectively:

$$
\begin{aligned}
\zeta &= \frac{3.85 \cdot f \cdot \Delta x}{\bar{U}^*} \\
\gamma &= \frac{11.5 \cdot f \cdot \Delta y}{\bar{U}^*} \\
\mu &= \frac{3.85 \cdot f \cdot \Delta z}{\bar{U}^*} \\
\bar{U}^* &= \frac{1}{H} \cdot \int_0^H \bar{U}(z) \cdot dz
\end{aligned}
\tag{4.14}
$$

The expression of eq. 4.13 is quite similar as compared to those given in EN 1991-1-4. Applying the equations of Diederich [1956], the integration of the coherence function $\gamma_{ij}(f)$ over the whole structure can be analytically solved if the lattice plate theory is applied (Verboom [2010]). The solution to the integration of the coherence function in each space direction yields to the same function as eq. 4.13.

Simiu [1973] modified the along-wind correlation presented by Vellozi and Cohen providing a new refined expression. It takes into account the small correlation of the wind pressures between the windward and leeward faces of a building observed in full scale measurements:

$$
R_x = \frac{C_w^2 + 2 \cdot C_w \cdot C_l \cdot N(f) + C_l^2}{(C_w + C_l)^2} \tag{4.15}
$$

where C_w and C_l are the drag force coefficients for the windward and leeward sides respectively ($C_D = C_w + C_l$) and $N(f)$ the frequency-dependent correlation component between both faces of the building.

Another mathematical formulation of $|\chi(f)|^2$ was given by Hölscher [1993]. Wind tunnel measurements were carried out on small cylinders measuring the pressure over the rounded surface. An empirical formulation for $|\chi(f)|^2$ was proposed:

$$|\chi(f)|^2 = \frac{\beta}{\left(1 + \left(\gamma \cdot \frac{f \cdot D}{\bar{U}}\right)^2\right)^{\frac{\delta}{6}}} \tag{4.16}$$

This simple and flexible formulation defines the aerodynamic admittance function in terms of three adjustable factors β, γ and δ.

The Eurocode 1 applies a quasy-steady formulation equivalent to the solution proposed by Vellozzi and Cohen considering the frequency-dependent coherence function of the wind turbulence over the whole structure:

$$|\chi(f)|^2_{EC1} = R_y \cdot R_z = \left(\frac{1}{\eta_B} - \frac{1}{2 \cdot \eta_B^2}(1 - e^{-2\eta_B})\right) \cdot \left(\frac{1}{\eta_H} - \frac{1}{2 \cdot \eta_H^2}(1 - e^{-2\eta_H})\right) \tag{4.17}$$

where the nondimensional factors η_B and η_H cover the lack of correlation in acrosswind and vertical directions calculated at the reference height $z_s = 0.6 \cdot H$:

$$\begin{aligned} \eta_B &= \frac{K_y \cdot C_y \cdot f \cdot B}{\bar{U}(z_s)} = \frac{0.4 \cdot 11.5 \cdot f \cdot B}{\bar{U}(z_s)} \\ \eta_H &= \frac{K_z \cdot C_z \cdot f \cdot H}{\bar{U}(z_s)} = \frac{0.4 \cdot 11.5 \cdot f \cdot H}{\bar{U}(z_s)} \end{aligned} \tag{4.18}$$

The factors K_y and K_z included in the numerators, reduce the influence of the decay coefficients C_y and C_z on each direction of the wind turbulence. The origin of this reduction is justified by the mathematical approach for the determination of the gust response factor presented by Solari in a comprehensive work in Solari [1988a] and preciser reasoned in Section 5.2.

The formulation of Eurocode 1 does not take into account the lack of pressure correlation in the along-wind direction. Similarly, Vickery [1963] shows that disregarding the

longitudinal correlation, the results provided by the analytical solutions and wind tunnel tests are quite similar.

4.3.2 Modal analysis and assumptions

A stated in previous chapters, the application of the aerodynamic tests using a HFFB helps to determine the aerodynamic forces acting on a geometrical model of a real structure. If the model is aerodynamic, i.e. stiff model, the resultant aerodynamic forces depend on the geometrical shape. In the current work, starting from these aerodynamic forces, the aerodynamic admittance function will be identified. For this, some mathematical assumptions should be made.

In structural dynamics, the modal method is commonly used to reduce the mathematical complexity in the solution of a system with many degrees of freedom. The modal analysis reduces these coupled equations of motion to a set of uncoupled modal equations. Each of the modal equations are solved to obtain the modal contribution to the real response of the structure:

$$m_j^* \cdot \ddot{\xi}_j(t) + c_j^* \cdot \dot{\xi}_j(t) + k_j^* \cdot \xi_j(t) = w_j^*(t) \tag{4.19}$$

where m_j^*, c_j^*, k_j^* and $w_j^*(t)$ are the generalized mass, damping, stiffness and force in the mode j of the structure and are defined as follows:

$$\begin{aligned} m_j^* &= \int_0^H \psi_j^2(z) \cdot m(z) \cdot dz \\ c_j^* &= 2 \cdot \zeta \cdot \omega_j \cdot m_j^* \\ k_j^* &= 2 \cdot \pi \cdot f_j^2 \cdot m_j^* \\ w_j^* &= \int_0^H \psi_j(z) \cdot p_{ext}(z) \cdot dz \end{aligned} \tag{4.20}$$

The total real response of the structure $x(z,t)$ is determined as the addition of each modal contribution $\xi_j(t)$ with the corresponding mode of vibration $\psi_j(z)$.

$$x(z,t) = \sum_j \psi_j(z) \cdot \xi_j(t) \tag{4.21}$$

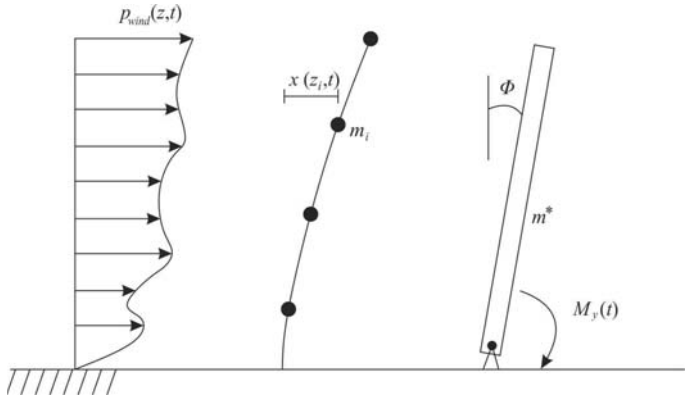

Figure 4.11: Correspondence between systems (Boggs [1991])

The solution for the generalized coordinate amplitude at the mode j may be written as (Boggs u. Peterka [1989]):

$$\xi_j(t) = \frac{1}{k^*} \cdot |H(f)| \cdot w^*(t) \tag{4.22}$$

And when the loading is random, the solution is:

$$S_{\xi\xi}(f) = \frac{1}{k^{*2}} \cdot |H(f)|^2 \cdot S_{w^*w^*}(f) \tag{4.23}$$

The main goal of the HFFB technique is the experimental determination of the generalized external loads w^* acting on the real structure. For this purpose, two main assumptions should be made: first, the model in the wind tunnel should be enough stiff to avoid aerodynamic damping or aeroelastic effects; second, if the mode of vibration of the real structure can be approximated to a linear one, the external load w^* acting on the real structure is equivalent to the aerodynamic base moments measured at the model's base in the wind tunnel.

$$w^*(t) = \int_0^H \psi(z) \cdot p_{wind}(z,t) \cdot dz = \int_0^H \frac{z}{H} \cdot p_{wind}(z,t) \cdot dz = M_y(t) \tag{4.24}$$

That means that, if the mode shape of the real building is linear, the external base moment $M_y(t)$ is equal to the generalized force $w^*(t)$. The entire process is depicted in

Figure 4.11. The external wind force produces a deformation of the real building and if a linear mode shape is considered, an equivalent SDOF rotational system can be defined for which an external base moment force is applied. It yields to the following equation of motion in terms of the rotation ϕ:

$$\ddot{\phi}_y(t) + 2 \cdot \xi \cdot \omega_0 \cdot \dot{\phi}_y(t) + \omega_0^2 \cdot \phi_y(t) = \frac{M_y(t)}{m^*} \tag{4.25}$$

It is important to note that the external base moment $M_y(t)$ produced by the aerodynamic forces and directly measured by the balance should be filtered with the mechanical transfer function of the model+balance system. The desired power spectral density S_{MyMy} may be distorted from a resonant amplification produced by the model+balance system. To avoid this problem, it is necessary to carry out accurate measurements of frequency and damping of the system to be sure that the range of interest is not influenced. Boggs [1991] cite three different ways of addressing this complication: filtering the measured signal with the transfer function of model+balance system, increasing extremely the damping of the model to prevent resonant peaks or making the fundamental frequency of the model much greater than the range interest. After determination of the aerodynamic base moment S_{MyMy}, the response of the real building can be computed according to eq. 4.23 if the transfer function of the real structure $|H(f)|^2$ is previously known. In many occasions, the selection of the mode shape is under discussion. Tschanz [1982] admits that the use of a linear mode shape is quite acceptable. Using the assumptions of Vickery [1970], an error between 1% and 3% is observed. On the contrary, Boggs u. Peterka [1989] criticize this assumption and warn for the need a mode shape correction if the shape of the real building becomes more irregular. Other impressions about mode shape corrections can be found in Tse u. a. [2009].

In the current work, the HFFB technique will be used to determine the aerodynamic admittance function $|\chi(f)|^2$ under interference conditions. Assuming a linear mode shape of the real structure, eq. 3.9 can be modified in modal way obtaining the following relationship Zhou u. Kareem [2003]:

$$S_{M_y M_y}(f) = 4 \cdot \frac{\bar{M}_y^2}{\bar{U}^2} \cdot |\Phi(f)|^2 \cdot S_{uu}(f) \tag{4.26}$$

$S_{M_y M_y}(f)$ is the one sided power spectral density function of the measured time series $M_y(t)$. In addition, $\bar{M}_y$ is the mean bending moment of the measured signal at the base of the chimney and $S_{uu}(f)$ is the power spectral density function of the along-wind turbulence. The function $|\Phi(f)|^2$ represents the total transfer function including

the combined effect of the mechanical transfer function of the model+balance system $|H(f)|^2_{m+b}$ and the aerodynamic admittance function $|\chi(f)|^2$. Under consideration of the separated influence of both components of $|\Phi(f)|^2$, eq. 4.26 is used to the define the aerodynamic admittance function $|\chi(f)|^2$ as follows:

$$|\chi(f)|^2 = \frac{\bar{U}^2}{4 \cdot \bar{M}_y^2} \cdot \frac{S_{M_y M_y}(f)/|H(f)|^2_{m+b}}{S_{uu}(f)} \tag{4.27}$$

As explained previously, in order to avoid dynamic amplification of the balance and model, the power spectra density of the aerodynamic forces $S_{M_y M_y}(f)$ should be filtered with $|H(f)|^2_{m+b}$ which has been previously determined in Section 4.2.2. The mean wind speed $\bar{U}$ and the power spectral density function $S_{uu}(f)$ are usually defined for a reference height z_s. The European EN 1991-1-4 and the North American ASCE 7-05 use a reference height of $z_s = 0.6 \cdot H$ for their procedures aimed at obtaining the gust response factor. On the contrary, other codes such as the Australian AS/NZS 1170.2:2011 or Japanese AIJ use $z_s = H$. In the wind field measurements carried out in the wind tunnel without building Section 2.3.1, an excellent agreement to the Eurocode proposals has been observed for the mean wind speed $\bar{U}$, turbulence intensity I_u and integral length scale L_u. Therefore, the reference height for the identification of $|\chi(f)|^2$ is selected at a height of $z_s = 0.6 \cdot 50 = 30$ cm as in the European standard.

Contrary to multilevel pressure models, stiff aerodynamic models are not conceived to measure the external wind load $p_{wind}(z,t)$ over the height of the structure to determine the generalized load $w^*(t)$. But this method is much more cheaper and faster than the aeroelastic set-ups, in which the structural parameters of the model should be scaled to the real situation. Here, only a stiff model of the structure is necessary.

4.3.3 Identification of the aerodynamic admittance

Figure 4.12 depicts the first results obtained for the identification of the aerodynamic admittance function $|\chi(f)|^2$ without the nearby building.

Figure 4.12(a) summarized in a same picture the filtered signals of the power spectral density functions $S_{M_y M_y}(f)$ with the SDOF mechanical transfer function $|H(f)|$, as well as both functions separately. The use of the classical transfer function defined in eq. 4.3 seems to dilute the resonant peak as the green line shows. A upper frequency of 100 Hz has been selected to analyze the data. Higher frequency are not useful due to the filtration obtained at this range. Figure 4.12(b) shows the aerodynamic admittance function. The curve is normalized with the frequency $f \cdot D/\bar{U}_{z_s}$, where D is the diameter of the chimney's model. The red line represents the mathematical expression of $|\chi(f)|^2$ proposed in the

Eurocode 1 and defined in eq. 4.17. The green line is the empirical formula determined by Vickery, see eq. 4.12. The black line approximates the results obtained from the wind tunnel tests according to the approach of Hölscher and fitting the β, γ and δ factors in Matlab.

The results show a bad agreement of $|\chi(f)|^2$ between the curves given in the literature and the obtained measurements. For high frequencies, the aerodynamic admittance function changes its trajectory from a decaying tendency to a rising one. The application of eq. 4.3 produces only good results for the pre-resonant range of frequencies. The given formula for the mechanical transfer function of a SDOF system cannot be successfully applied due to its divergence to the measured transfer function, especially in case of the post-resonant frequency range.

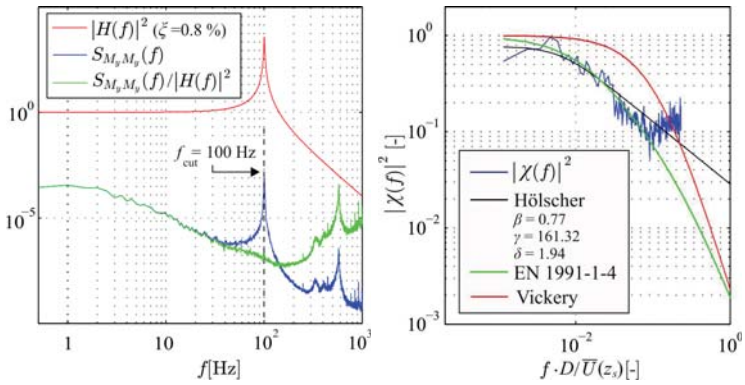

(a) Filtering of $S_{M_yM_y}(f)$ (b) Aerodynamic admittance function $|\chi(f)|^2$

Figure 4.12: Results provided by the classical mechanical transfer function

To avoid the above presented inconveniences, the measured mechanical transfer function $|H(f)|$ from pluck tests with lightly modifications at very low frequencies have been used. It describes in a more precise way the dynamic performance of the chimney's model. Figure 4.13(a) depicts the filtering process of $M_y(t)$ from the configuration without building using the real mechanical transfer function $|H(f)|$. Now the resonant peak can be successfully removed.

From these filtered signals, the corresponding $|\chi(f)|^2$ are calculated using eq. 4.27 and the result is depicted in Figure 4.13(b). The obtained aerodynamic admittance functions fit very well the proposal of Eurocode 1, see eq. 4.17 and therefore, the above presented approach used to identify $|\chi(f)|^2$ is validated.

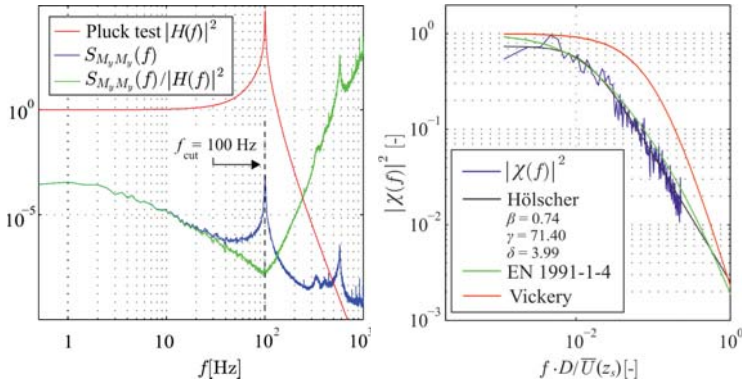

(a) Filtering of $S_{M_y M_y}(f)$

(b) Aerodynamic admittance function $|\chi(f)|^2$

Figure 4.13: Results provided by the measured mechanical transfer function

4.3.4 Verification of absence of vortex shedding

The Strouhal number St is the characteristic parameter to describe an oscillating flow mechanism. This nondimensional number is directly related to the frequency of the vortex shedding f_v. It can be calculated for rounded shapes as well as sharp-edges or rectangular cross-sections. The mathematical relation of the parameters can be described in the following terms:

$$St = \frac{f_v \cdot D_{ext}}{\bar{U}} \tag{4.28}$$

In order to corroborate the absence of vortex shedding in the above presented results, the power spectral density functions of the lateral F_y and longitudinal forces F_x have been calculated to determine f_v. In addition, it has been carried out at five different wind speeds. Figure 4.14 shows the spectra of both forces for two different wind speeds. The left figure is obtained for a wind speed of 6 m/s and several peaks can be observed. The fundamental frequency of the model is easy to observe at around $f_0 = 100$ Hz. The red line of the lateral forces shows also intermediate peaks, specially with a previous wide peak at around 50 Hz associated to the vortex shedding. Due to the non exact symmetry of the flow-chimney interaction inside the wind tunnel, the same peak can be also observed in the along-wind direction depicted in blue. A vortex shedding frequency of $f_v = 50$ Hz

yields to a Strouhal number of $St = 0.188$, which is a typical value associated to circular geometries.

The right figure shows the same spectra obtained at 12 m/s coinciding with the reference wind speed used for the wind tunnel experiments. In this case, the peak associated with the vortex shedding is merged with the fundamental frequency of the model in lock-in range, while in the longitudinal component none traces associated with vortex shedding can be observed. An equivalent performance to the longitudinal component was observed for the vertical forces. The absence of intermediate peaks at 12 m/s before the fundamental frequency in the horizontal and vertical force spectra makes a perfect filtering of the measured signal possible as shown in Figure 4.13(a).

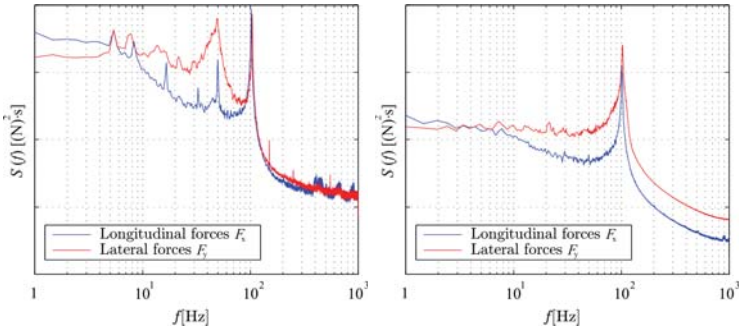

(a) 6 m/s (b) 12 m/s

Figure 4.14: Power spectral density functions of the lateral and horizontal wind forces

4.4 Influence of the interference effect on the aerodynamic admittance function

For the implementation of eq. 4.27 under interference conditions, the variables $\bar{U}$ and $S_{uu}(f)$ have been defined from the undisturbed condition calculated at the reference height of $z_s = 30$ cm. Consequently, the black-box nature of the transfer process between incoming wind and structural response helps to the define an aerodynamic admittance function which is used to relate the undisturbed incoming flow with the obtained wind forces due to the disturbed flow. This idea was also cited by Behrens [2004] who defined the aerodynamic admittance function as an input-output transfer matrix between the incoming wind flow process and the stochastic wind force process acting on the structure.

Due to the large number of experiments carried out in this parametric study, including the combinations of different factors with other aerodynamic admittance functions given in the literature, only the results regarding the cubic building are shown.

Figure 4.15(a) shows, using the formula of Hölscher, the approximated curves of $|\chi(f)|^2$ calculated for the case of a cubic building and chimney located in the corner (position 1). The curves are plotted for each wind direction θ together with the proposal given in EN 1991-1-4. At very low frequencies, the aerodynamic admittance function does not coincide always with the ideal value of $|\chi(f \rightarrow 0)|^2 = 1$ meaning an ideal energy transfer of wind turbulence to wind pressure. The reasons for this can be related with the disturbances of the system and the complexity of the wind tunnel tests. Hölscher [1993] as well does not show in his experiments an ideal transfer of energy at low frequencies. He reasoned that the relationship $|\chi(f \rightarrow 0)|^2 = 1$ observed by Vickery are related with the simplicity of his wind tunnel set-up. That the wind data and wind force have been not measured simultaneously can be one of the experimental uncertainties that yield to this fact. Another uncertainties related with the energy transfer as the influence of the lateral turbulence, the ratio L_u/D or the flow characteristics around the model's surface have been not considered in this study. Full scale measurements presented by Behrens [2004] diverge also from an ideal energy transfer at low frequencies.

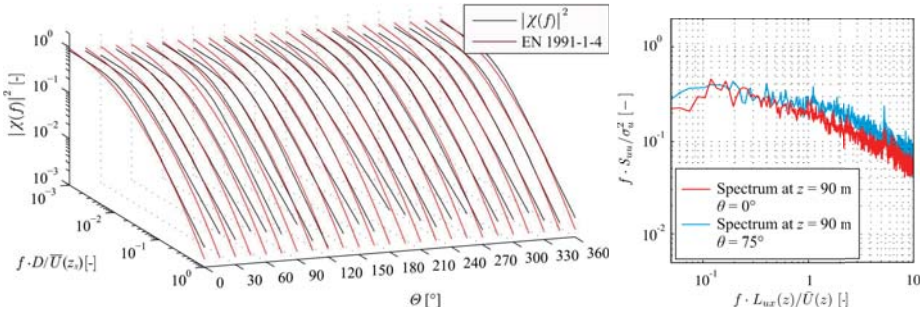

(a) Aerodynamic admittance functions (b) Wind spectrum comparison

Figure 4.15: Cubic building and chimney located in the corner

For medium and high frequency ranges, the results provided by the parametric study show a similar behaviour of the aerodynamic admittance functions for each wind direction θ. Nevertheless, some exceptions appear for specific wind directions increasing the aerodynamic admittance function. Figure 4.15(b) shows the differences observed in the wind spectrum between $\theta = 0°$ and $\theta = 75°$. This increase influences also the aerodynamic moments presented in the numerator of eq. 4.27 (the power spectral density function $S_{uu}(f)$ presented in the denominator is constant from the undisturbed flow condition). For the

other building type, a similar behaviour has been observed. In the next chapter, the gust response factor under interference conditions will be studied modifying the mathematical background of Solari. Therefore, for each different configuration studied, the increase of energy observed in the aerodynamic admittance function will be individually considered.

Jose Mari Sasieta. "Paisajes de viento".

5 Gust buffeting design for disturbed flow

In order to asses the influence produced by the interference effect on the dynamic response of a chimney, the measurements carried out for the disturbed wind flow condition will be analysed in detail. The results of the dynamic response of a propped chimney provided by the quasi-steady simulations presented in Section 3.3 have shown in a qualitatively manner the effect produced by a disturbed flow. Starting from the corrected wind speed profile $\bar{U}_d(z)$ presented in Section 2.4, and the conclusions obtained in the previous chapter, the gust response factor of an industrial chimney will be studied.

Using the mathematical background of the approach of Solari, the gust response factor G_x is modified to include the perturbations produced by the interference effect on the dynamic response of the chimney. The modification of the approach has been carried out for two different static configurations of the chimney.

Firstly, a cantilever model of an industrial chimney has been considered. The gust response factor has been determined depending on the shape of the adjacent building and the position of the chimney. In order to evaluate the influence of the height of structure H with respect to the height of the nearby building h, 5 combinations of the ratio H^*/h have been considered (being H^* the remainder cantilever length above the building $H^* = H - h$). In addition, 6 different fundamental frequencies f_0 and 3 damping ratios ξ of the chimney have also been included in the parametric study. Secondly, the gust response factor G_x of a propped chimney connected to the adjacent building has been also determined solving the main restriction of the procedure.

As result of this parametric study, an increasing factor IF_{Gx} of the gust response factor G_x is proposed. IF_{Gx} is defined depending on the height of the chimney H, the height of the nearby building h, the position of the chimney with respect to the building, fundamental frequency f_0 and damping ratios ξ of the industrial chimney and static configuration of the chimney.

5.1 Along-wind response including disturbed flow

The main goal of the current investigation is to provide the engineers with a method to calculate the maximum structural response for buffeting wind loading when a chimney has to be built in an industrial area. For the determination of the peak response of the structure $\hat{X}_d$ under disturbed flow conditions the following steps should be made:

The gust response factor G_x relates the mean with the maximum response of a structure. In case of undisturbed wind conditions, the relation is defined as:

$$\hat{X}_0 = G_{x,0} \cdot \bar{X}_0 \tag{5.1}$$

In case of disturbed flow, the relation changes to:

$$\hat{X}_d = G_{x,d} \cdot \bar{X}_d \tag{5.2}$$

Multiplying and diving the latter equation by $G_{x,0}$, the maximum response of the chimney under interference effects $\hat{X}_d$ can be calculated according to the following expression:

$$\hat{X}_d = IF_{G_x} \cdot G_{x,0} \cdot \bar{X}_d \tag{5.3}$$

where:

- IF_{G_x} is the increasing factor defined as the ratio $IF_{G_x} = G_{x,d}/G_{x,0}$
- $G_{x,d}$ is the gust response factor including the interference effect
- $G_{x,0}$ is the gust response factor from the undisturbed wind flow conditions
- $\bar{X}_d$ is the mean response of the structure calculated for a disturbed mean wind speed according to eq. 2.25 for the most disadvantage wind direction θ

In order to compute numerically the increasing factor IF_{G_x}, the influence of the disturbed wind flow on the dynamic response of the chimney has been considered comparing the gust response factor G_x for both flow conditions. The reference undisturbed gust response factor $G_{x,0}$ has been calculated from the undisturbed wind flow. On the contrary, the disturbed factor $G_{x,d}$ is obtained from the measured disturbed flow.

The increasing factor IF_{G_x} fully covers the dynamic amplification produced by the interference effect on the chimney. It is expected that the gust response factor decreases when the height of the structure H also increases, thus diluting the participation of the

disturbed flow on the chimney. The increasing factor IF_{G_x} has been studied for different structural combinations, varying the height H, the fundamental frequency f_0 and the damping ratio ξ.

5.2 Mathematical background of Solari's approach

Starting from previous investigations made by Simiu (Simiu [1973] and Simiu u. Lozier [1975]), Solari developed in closed-form a design approach for the gust response factor G_x (Solari [1993b]). Before this approach was published, the along-wind response of structures subjected to gust buffeting was calculated using graphs (Davenport [1967], Vellozzi u. Cohen [1968] and Simiu [1980]) or computer programs as in Simiu u. Lozier [1975]. The closed-form solution was analytically defined using the mathematical advantages of the equivalent wind spectrum technique (EWST) (Solari [1988b] and Solari [1988a]).

The general mathematical treatment of the along-wind response of structures under gust buffeting was presented in Section 3.1.1. Solari follows the early studies of Davenport including mathematical innovations and updates provided by full scale measurements.

The approach was entirely defined in the frequency domain and was solved using the modal technique. If the contributions of the second and higher modes of vibration can be considered as negligible, the mean static response of structure can be defined in terms of the fundamental mode of vibration $\psi_0(z)$ as follows:

$$\bar{X}(z) = \frac{\psi_0(z)}{k_0^2} \cdot \bar{F}_0 = \frac{\rho \cdot B \cdot H \cdot C_D \cdot \bar{U}^2(z_s)}{m_0 \cdot (2 \cdot \pi \cdot f_0)^2} \cdot \frac{K_a}{2} \cdot \psi_0(z) \tag{5.4}$$

where f_0 is the fundamental frequency of the structure, m_0 the modal mass in the fundamental mode, ρ the density of the air, B and H are the width and height of the structure respectively, C_D the drag coefficient, z_s the reference height of the structure ($z_s = 0.6 \cdot H$) and K_a a non-dimensional quantity that takes into account the variation over the height z of the mean wind speed profile $\bar{U}(z)$ with the fundamental mode shape of structure $\psi_0(z)$:

$$K_a = \frac{1}{H \cdot \bar{U}^2(z_s)} \cdot \int_0^H \bar{U}^2(z) \cdot \psi_0(z) \cdot dz \tag{5.5}$$

Regarding the fluctuating component of the response of the structure $S_x(z, f)$, an equivalent expression to eq. 3.10 is given:

$$S_x(z,f) = \frac{1}{m_0^2 \cdot (2 \cdot \pi \cdot f_0)^4} \cdot \frac{S_{f_0}(f)}{\left(1 - \frac{f^2}{f_0^2}\right)^2 + 4 \cdot \xi^2 \cdot \frac{f^2}{f_0^2}} \cdot \psi_0(z)^2 \tag{5.6}$$

where ξ is the damping ratio and $S_{f_0}(f)$ is the power spectral density function of the first fluctuating modal force. This last variable was defined by Solari as follows:

$$S_{f_0}(f) = \left[\rho \cdot B \cdot H \cdot C_D \cdot \bar{U}(z_s) \cdot \sigma_u(z_s) \cdot K_b\right]^2 \cdot S^*_{u-eq}(f) \tag{5.7}$$

where K_b is another non-dimensional quantity that takes into account the variation over the height z of the mean wind speed profile $\bar{U}(z)$ and standard deviation of the wind turbulence $\sigma_u(z)$ with the fundamental mode shape of structure $\psi_0(z)$:

$$K_b = \frac{1}{H \cdot \bar{U}(z_s) \cdot \sigma_u(z_s)} \cdot \int_0^H \bar{U}(z) \cdot \sigma_u(z) \cdot \psi_0(z) \cdot dz \tag{5.8}$$

The EWST technique was introduced by Solari to define the equivalent wind spectrum $S^*_{u-eq}(f)$. Instead of the classical wind configuration, the equivalent wind structure is defined as a stochastic stationary Gaussian process characterized by a mean velocity profile $\bar{U}(z)$ on which an equivalent turbulent fluctuation $u^*_{eq}(t)$ is superimposed, perfectly coherent in space (Solari [1988a]):

$$U_{eq}(z,t) = \bar{U}(z) + \sigma_u(z) \cdot u^*_{eq}(t) \tag{5.9}$$

The non-dimensional stochatic stationary Gaussian process is identified in the frequency domain trough its PSDF $S^*_{u-eq}(f)$. Assuming a perfect correlation of the wind pressures between the windward and leeward faces of structure, $S^*_{u-eq}(f)$ is defined as follows:

$$S^*_{u-eq}(f) = \frac{S_u(z_s, f)}{\sigma_u^2(z_s)} \cdot R_y(K_y, z_s) \cdot R_z(K_z, z_s) \tag{5.10}$$

where $S_u(z_s, f)$ is the classical power spectrum of turbulence (Solari [1990] and Solari [1993a]), $R_y(K_y, z_s)$ and $R_z(K_z, z_s)$ are the aerodynamic admittance functions described in eq. 4.17. Factors K_y and K_z depend on the mode shape and incoming wind profile and

their aim is to correct the numerical deviations of this technique. Note that eq. 5.10 is entirely computed at z_s. As stated in Verboom [2010], the definition of a reference height z_s was defined by Solari [1982] as a mathematical trick to solve the double integral of the modal cross-correlated spectral function $S_{ff_i ff_j}(f)$ over the entire height of the structure to obtain the standard deviation of the fluctuating response $\sigma_x(z)$. An identical solution can be easily represented with the functions $f(z)$ and $g(z)$ applying the fundamental theorem of the integrals:

$$\int_0^H f(z) \cdot g(z) \cdot dz = f(z_s) \int_0^H g(z) \cdot dz \tag{5.11}$$

where z_s is a height located between 0 and H. This mathematical trick can be applied if and only if $g(z)$ is continuous and without changing sign on the open interval $0 < z < H$. Solari demonstrated that if a logarithmic wind profile $\bar{U}(z)$ is used and a linear mode shape $\psi_0(z)$ is selected, then the reference height is $z_s \cong 0.6 \cdot H$. This mathematical step is responsible for the prohibition of the application of the calculation procedure of the structural factor $c_s c_d$ in case of buildings with changing sign in its fundamental mode of vibration $\psi_0(z)$ and graphically depicted in Figure 1.9.

Applying now eq. 3.11 in eq. 5.6, it is possible to obtain the standard deviation of fluctuating response $\sigma_x(z)$ in terms of a background component Q_0^2 defined over the entire frequency range f and a resonant component R_x^2 defined at the fundamental frequency f_0:

$$\sigma_x(z) = \frac{\rho \cdot B \cdot H \cdot C_D \cdot \bar{U}^2(z_s)}{m_0 \cdot (2 \cdot \pi \cdot f_0)^2} \cdot I_u(z_s) \cdot K_b \cdot \sqrt{Q_0^2 + R_x^2} \cdot \psi_0(z) \tag{5.12}$$

where $I_u(z_s)$ is the turbulence intensity evaluated at the reference height z_s. The background and resonant components are now evaluated similarly to eq. 3.14 and eq. 3.15:

$$\begin{aligned} Q_0^2 &= \int_0^\infty S^*_{u-eq}(f) \cdot df \\ R_x^2 &= \frac{\pi \cdot f_0}{4 \cdot \xi} \cdot S^*_{u-eq}(f_0) \end{aligned} \tag{5.13}$$

Finally, the gust response factor G_x can be obtained applying eq. 3.21:

$$G_x = 1 + 2 \cdot g_x \cdot I_u(z_s) \cdot \frac{K_b}{K_a} \cdot \sqrt{Q_0^2 + R_x^2} \tag{5.14}$$

This equation shows that applying the modal coordinates and introducing the EWST to describe explicitly $S^*_{u-eq}(f)$, a generalized gust response factor G_x can be deduced for the structure without consideration of the height z.

5.3 Increasing factor of the gust response

5.3.1 Cantilevered chimney

In order to consider the consequences of the interference effect on a chimney located in front of an industrial chimney, the formulation provided by Solari has been modified introducing the results presented in the current work. The following mathematical approach has been carried for a cubic building, but the results can be applied on safe side for all building shapes.

For the application of eq. 5.14, the standard deviation I_u obtained from the wind tunnel tests has been calculated at the reference height z_s. This height is defined in a similar way as in the Eurocode:

$$z_s = 0.6 \cdot H = 0.6 \cdot (H^* - h) \tag{5.15}$$

where H is the height of the chimney, h the height of the building and H^* the length of the chimney above the building. As stated in Section 4.4, the admittance function $|\chi(f)|^2$ does not suffer remarkable changes in shape due to the disturbed flow. Using this conclusion, the same equivalent spectrum $S^*_{u-eq}(f)$ as the one given by Solari has been used to calculate the background Q_0^2 and resonant components R_x^2. In addition, numerical calculations have shown that the variation of the ratio $S_u(z_s, f)/\sigma_u^2(z_s)$ presented in eq. 5.10 changes negligibly with respect to the undisturbed flow condition. An equivalent effect has been observed in Figure 2.14(a). Nevertheless, the increase of energy observed for some situations of $|\chi(f)|^2$, is here individually covered with the factor $\sigma_d^2(z_s)/\sigma_u^2(z_s)$.

Factors K_a and K_b are strongly dependent on the disturbed wind flow. Factor K_a has been calculated using the modified expression of the mean wind speed $\bar{U}_d(z, \theta)$ given in Section 2.4 as follows:

$$K_a(\theta) = \frac{1}{H \cdot \bar{U}_d(z_s, \theta)^2} \cdot \int_0^H \bar{U}_d(z, \theta)^2 \cdot \psi_0(z) dz \tag{5.16}$$

where $\psi_0(z)$ is the fundamental mode shape as depicted in Figure 5.1:

$$\psi_0(z) = \left(\frac{z}{H^* + h}\right)^{1.6} \tag{5.17}$$

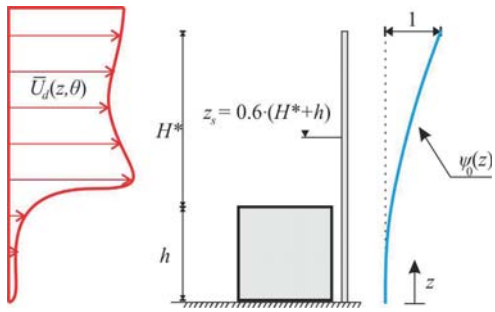

Figure 5.1: Considered mode shape for a free-standing cantilevered chimney

A mode shape with an exponent value of 1.6 represents fairly a real mode of a cantilevered structure (Solari [1982]). In a parallel way, factor K_b is influenced also by the disturbed turbulence characterized by the standard deviation $\sigma_u(z,\theta)$ and shown in Figure 2.15 for a wind direction of $\theta = 15°$ in case of a cubic building and a chimney located in the corner.

$$K_b(\theta) = \frac{1}{H \cdot \bar{U}_d(z_s,\theta) \cdot \sigma_u(z_s,\theta)} \cdot \int_0^H \bar{U}_d(z,\theta) \cdot \sigma_u(z,\theta) \cdot \psi_0(z) dz \tag{5.18}$$

In order to cover the large number of combinations of real industrial chimneys, 5 different ratios H^*/h have been considered. In addition, 6 different fundamental frequencies f_0 and 3 damping ratios ξ of the chimney have been included in the parametric study:

$$\begin{aligned} &H^*/h[-] = [0.5\ 1\ 1.5\ 2\ 2.5] \\ &f_0[Hz] = [0.1\ 0.2\ 0.25\ 0.5\ 0.75\ 1] \\ &\xi[\%] = [1\ 3\ 5] \end{aligned} \tag{5.19}$$

The wind direction θ is a fundamental variable to stipulate the disturbed gust response factor G_x. When the ratio H^*/h varies, the reference height z_s, for which the majority of variables are referenced, also changes. Therefore, the most adverse situation can vary with

a different wind direction θ. To make the reader the effect of this complex phenomenon observed during the calculation process clear, Figure 5.2 shows the changes of G_x with θ for three different ratios H^*/h, cubic building and a chimney positioned in the middle of the building.

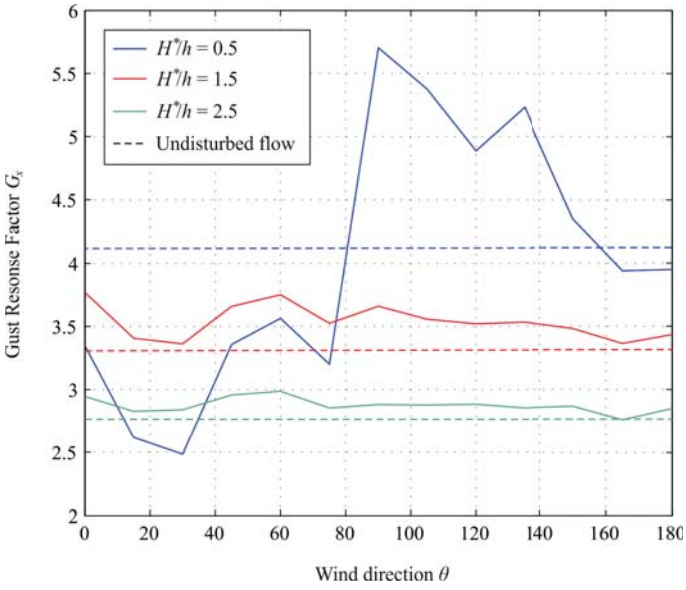

Figure 5.2: Variation of $G_x(\theta)$ for different ratios H^*/h for position2

The results showed in Figure 5.2 have been plotted for a fundamental frequency $f_0 = 0.1$ Hz and a damping ratio $\xi = 1$ %. It can be observed how the gust response factor fluctuates over θ, being also lower than the configuration without building. The lowest ratio H^*/h provides the largest variations of G_x. This effect is related to the assignment of the reference height, being in this case $z_s = 54$ m and situated below the nearby building, and therefore governed by large turbulences. In this case, the most adverse wind direction is $\theta = 90°$. It should be pointed out, that due to the statical configuration of the chimney depicted in Figure 5.1, the wind velocities below the roof of the building are also integrated over the mode shape. Therefore, observing the continuous blue line, it can be noted how if the chimney is located windward ($\theta > 90°$) the gust response factors are always higher than if the chimney is situated leeward ($\theta < 90°$), for which the shadowing produced by the building appears. For the other ratios H^*/h, this conclusion cannot be directly extrapolated, because of their reference heights above the building and dependent on the increase of turbulence produced by the vortex shedding on the building's corners. In the

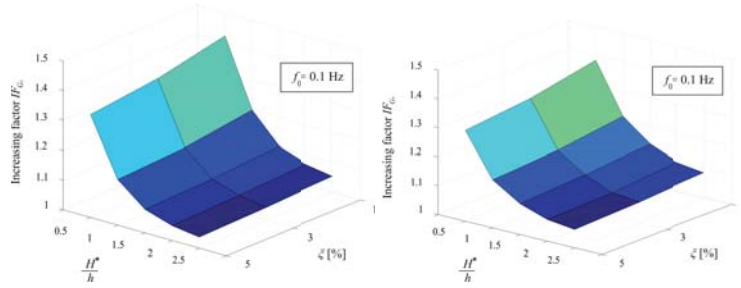

(a) Position 1 (b) Position 2

Figure 5.3: Increasing factor IF_{G_x} for varying ratio H^*/h and damping ratio ξ

definition of IF_{G_x}, the most adverse wind direction θ has been individually included as reference value for each different configuration.

Figure 5.3 shows the variation of IF_{G_x} with H^*/h and the damping ratio ξ for a chimney with a fundamental frequency of $f_0 = 0.1$ Hz. Figure 5.3(a) is plotted for the chimney located in the corner and Figure 5.3(b) for the chimney located in the middle. Both surfaces show a similar performance, but position 1 shows a lightly higher maximum and a faster decay. When the ratio H^*/h increases, the differences on the gust response factor G_x between the disturbed and undisturbed wind configurations tend to disappear. This is a logical performance due to the extension of the surface in which the disturbed wind acts and elevating the reference height z_s up to altitudes in which the wind is undisturbed.

In order to provide designers and engineers with a calculation method for the gust response factor G_x considering the dynamic amplification produced by the interference effect, a closed-form solution to the increasing factor IF_{G_x} has been determined:

$$IF_{G_x} = 1.05 + a(f_0, \xi) \cdot e^{\left(-b(\xi) \cdot \frac{H^*}{h}\right)} \quad \text{for } \frac{H^*}{h} \geq 0.5 \tag{5.20}$$

where a and b are coefficients which depend on the ratio H^*/h, fundamental frequency f_0 and damping ratio ξ. The factors are solution to the non-linear dependence of IF_{G_x} on the above presented variables. Therefore, a simplified numerical approximation has been obtained using Matlab. The coefficients a show a non-linear behaviour with respect

to the fundamental frequency f_0 and damping ratio ξ. On the other hand, factor b can be linearly approximated as function of ξ only:

$$\begin{aligned} a(f_0, \xi) &= k_1^c + k_2^c \cdot \xi + k_3^c \cdot f_0 + k_4^c \cdot \xi^2 + k_5^c \cdot \xi \cdot f_0 \\ b(\xi) &= 10 \cdot \xi + k_6^c \end{aligned} \tag{5.21}$$

where k_i^c are constants that depend on the location of the chimney with respect to the building:

Table 5.1: Factors k_i^c for a cantilevered chimney

	k_1^c	k_2^c	k_3^c	k_4^c	k_5^c	k_6^c
Corner	0.96	-0.42	-0.45	6.25	4.3	1.8
Middle	0.63	-0.03	-0.31	0	3	1.2

Figure 5.4 depicts the increasing factor IF_{G_x} according to eq. 5.20 calculated for a free-standing chimney as shown in Figure 5.1 with a damping ratio of $\xi = 1\%$. The example represents the influence of the interference effect on a very flexible and stiff chimney with fundamental frequencies of $f_0 = 0.1$ Hz and $f_0 = 1$ Hz respectively.

The analytical solution for IF_{G_x} provided by eq. 5.20 fits very well with the numerical results shown in Figure 5.3 after modification of the mathematical approach proposed by Solari in order to consider the dynamic amplification caused on an industrial chimney by the interference effect produced by an adjacent building.

Strictly speaking, eq. 5.20 has been determined for ratios $H^*/h \geq 0.5$. Intuitively, it can be supposed that for ratios $H^*/h < 0.5$ the gust response factor tends to reduce its value, but the high turbulences measured along the height of the chimney if it is situated windward does not support this idea. Therefore, additional wind tunnel tests at low heights are necessary to study this phenomenon in a more precise manner. Computer fluid dynamics can be a useful tool to corroborate experimental tests carried out in a boundary layer wind tunnel.

Due to this lack of information and with the aim of maintaining the current work on the safe side, a constant value of IF_{G_x} has been proposed for ratios $H^*/h < 0.5$.

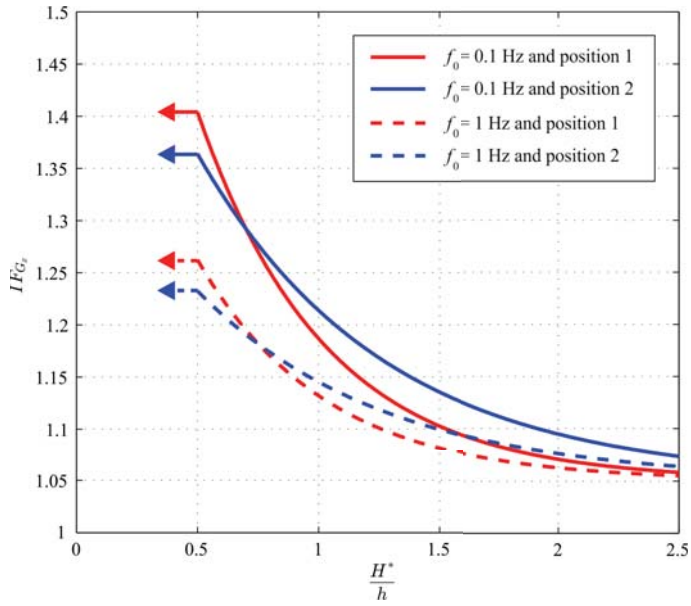

Figure 5.4: Increasing factor IF_{G_x} for two different chimneys with damping ratio of $\xi = 1\%$

5.3.2 Propped chimney

As stated above, the application of the procedure to determine the structural factor $c_s c_d$ according EN 1991-1-4 does not allow a changing sign in the fundamental mode of vibration. Therefore, the statical change produced by an intermediate connection on the chimney prevents its application.

For this study, the condition of the non-changing sign in the mode shape has been maintained. Figure 5.5 shows the considered mode shape $\psi_0(z)$:

$$\psi_0(z) = \begin{cases} 0 & z < h \\ \dfrac{z-h}{H^*} & h \leq z \leq h + H^* \end{cases} \tag{5.22}$$

The error included in this approximation is negligible and, actually, the mode shape below the support acts counterweighting the displacements of the cantilevered length H^*. In addition, very low chimneys, for which the incidence of the wind on the lower part of

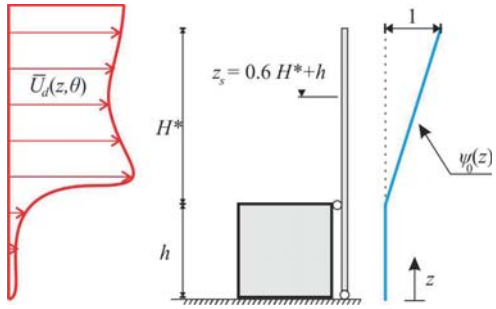

Figure 5.5: Considered mode shape for a propped chimney

the mode shape is more important, are usually not supported. In this case, the reference height z_s will only be considered for the cantilevered part of the structure:

$$z_s = 0.6 \cdot H^* + h \tag{5.23}$$

The numerical procedure is also carried out searching for the most unsafe wind direction θ. Factors K_a and K_b have also been modified to include the change in the mode shape $\psi_0(z)$:

$$K_a(\theta) = \frac{1}{H^* \cdot \bar{U}_d(z_s,\theta)^2} \cdot \int_h^{h+H^*} \bar{U}_d(z,\theta)^2 \cdot \psi_0(z) dz \tag{5.24}$$

$$K_b(\theta) = \frac{1}{H^* \cdot \bar{U}_d(z_s,\theta) \cdot \sigma_u(z_s,\theta)} \cdot \int_h^{h+H^*} \bar{U}_d(z,\theta) \cdot \sigma_u(z,\theta) \cdot \psi_0(z) dz \tag{5.25}$$

The assumption of a zero mode shape up to the roof of the building allows for the application of Solari's approach. Therefore, contrary to the previous section, the wind flow below the roof is neglected for the calculation integrating the wind forces over the cantilever length H^* only.

For this statical configuration, the same parametric study as in the previous section has been carried out. The number of considered variables is given in eq. 5.19 and the consideration of the most adverse situation depending on the wind direction θ has also been taken into account.

Obviously, in case of the propped chimney, it is evident that the undisturbed configuration cannot exist, because a lateral support of the chimney provokes always a disturbed flow through the "connection" building. This evidence has not be taken into account for the calculation. Therefore, strictly speaking, IF_{G_x} compares the effect produced by the disturbed and undisturbed for a structure with a mode shape as depicted in Figure 5.5.

The factor IF_{G_x} for propped chimneys has been analytically determined in the same way as for cantilever structures and therefore, eq. 5.20 can be also applied. For this static case, the constant $a(f_0, \xi)$ follows the same form as in eq. 5.21 but using different factors k_i^p while the constant $b(\xi)$ changes sightly:

$$b(\xi) = 12.5 \cdot \xi + k_6^p \tag{5.26}$$

Similarly to the cantilevered configuration,the coefficients k_i^p defined for a propped structure depend on the location of the propped chimney with respect to the building:

Table 5.2: Factors k_i^p for a propped chimney

	k_1^p	k_2^p	k_3^p	k_4^p	k_5^p	k_6^p
Corner	3.47	-0.43	-1.26	6.25	5.3	3.5
Middle	2.9	-0.77	-1.04	12.5	2.5	2.6

Figure 5.6 shows the results of IF_{G_x} calculated for a propped chimney with damping ratio $\xi = 1\%$. Contrary to Figure 5.4, the effect of the disturbed flow with a discontinuous mode shape concentrates its influence only on the cantilever length H^*. Therefore, the large increase of turbulence observed above the roof of the building is especially important with this statical configuration. An extreme increase of the gust response factor has been observed for the position 2 and wind direction $\theta = 60°$. In this case, for a ratio $H^*/h = 0.5$, the reference height is located at an altitude with extreme high turbulence grade produced by the vortex shedding at the sharp edges. For this unique sum of coincidences, the gust response factor G_x can be 75 % larger as in case of an undisturbed flow.

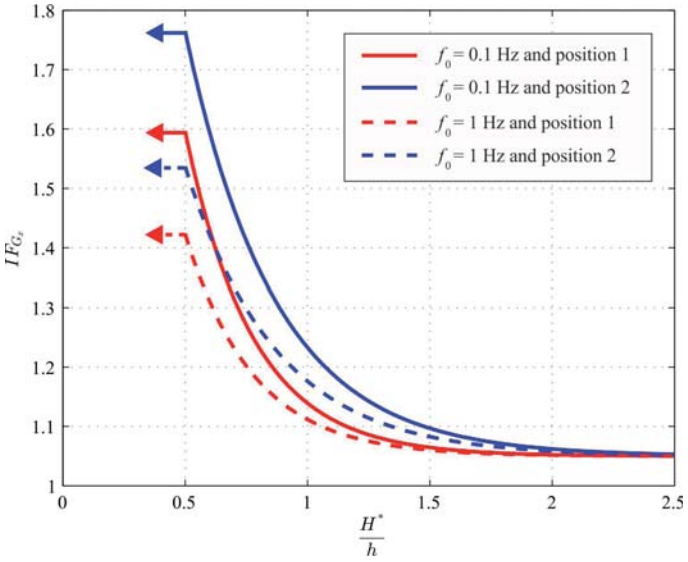

Figure 5.6: Increasing factor IF_{G_x} for two different chimneys with damping ratio of $\xi = 1\%$

5.4 Application of the new design approach

The proposals given in the codes for the calculation of the maximum response of a structure under gust buffeting do not take into account the possibility of appearance of a disturbed wind flow due to the presence of a nearby building. To avoid this lack of information, a new method of calculation has been defined. The new buffeting design method of industrial chimneys includes an increasing factor of the gust response factor IF_{G_x} and can be easily calculated depending on the position of the chimney, on the ratio H^*/h, on the fundamental frequency of chimney f_0 and on the damping ratio ξ.

As stated in the introduction of the current work, the gust factor of structures with a changing sign in its fundamental mode shape $\psi_0(z)$ cannot be calculated. To solve this problem, the gust response factor of a propped chimney has been calculated modifying the structural mode shape implemented in Solari's approach. The increasing factor IF_{G_x} has been defined including this static change and influence of the interference effect.

The undisturbed wind field obtained from the wind tunnel tests and presented in Section 2.3.1 fits good with the proposal of a terrain category II according to DIN EN

1991-1-4/NA. Consequently, the gust response factor $G_{x,0}$ in undisturbed flow conditions can be accepted as the nominal $G_{x,EC}$ obtained applying the code.

The maximum response of an industrial chimney can be now easily computed multiplying the increasing factor IF_{G_x} by the reference $G_{x,0}$ and the mean disturbed response $\bar{X}_d$, as shown eq. 5.3. In case of a propped chimney, the reference gust response factor $G_{x,0}$ must be calculated by a cantilevered chimney of height H^* placed on top of a very stiff building of height h, see Figure 5.7.

For a cantilevered chimney of height H, the reference gust response factor $G_{x,0}$ should be calculated according to the code using a reference height of $z_s = 0.6 \cdot H$, see left picture of Figure 5.7. On the contrary, in case of a propped connection of the chimney, the previous consideration has to be changed and a chimney of height H^* placed on top of the stiff building of height h has to be supposed. In consequence, as shown in the right picture of Figure 5.7, the reference height has to be defined as $z_s = 0.6 \cdot H + h$:

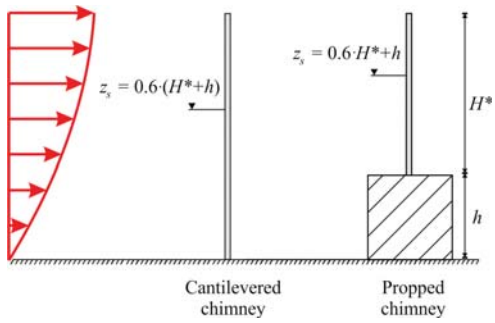

Figure 5.7: Structural definitions for which the reference G_x has to be calculated

It should be pointed out, that all these investigations cannot be strictly applied in case of rooftop antennas. The variable position of these structures on the roof of the buildings make this case of study complex being the wind field characteristics over a building's roof different than those presented in the current work. The analytical expression of IF_{G_x} given in eq. 5.20 tends asymptotically to the value of 1.05, remaining a safe-sided nominal increase of 5% of the gust response factor G_x due to presence of the nearby building.

As explained in Section 5.2, the reference height z_s defined by Solari depends mainly on the mean wind speed profile $\bar{U}(z)$ and fundamental mode shape of the structure $\psi_0(z)$. Strictly speaking, the value of z_s has to be calculated individually for each different configuration of the parametric study. Nevertheless, numerical verifications have shown that the position of the reference height varies between the 52% and 65% of the height of the structure. The modification of this parameter depending on the incoming flow

characteristics was also supposed by Cook [2007], seeking in this case an expert advice. The improvement of the results obtained with the exact estimation of z_s is very low, and in order to avoid more complications, the 60 % proposed by Solari has been maintained.

The maximum response of the chimney under interference conditions $\hat{X}_d$ has been computed from the gust response factor method developed by Solari. The structural factor $c_s c_d$ used in the Eurocode is a modification of the latter and the mathematical background is identical. Nevertheless, the European approach uses the reference height z_s for the determination of $c_s c_d$, but this factor is associated with the peak wind force $\hat{F}(H)$ calculated at the top of the building and not with the mean wind force $\bar{F}(z_s)$ at the reference height. Therefore, strictly speaking, the maximum response under interference conditions should not be computed from the structural factor $c_s c_d$, but more precise from eq. 5.3.

The above presented proposal has been studied using a constant height of $h = 60$ m for the nearby industrial building. Principally, the ratio H^*/h can be applied for each height h but in case of very small buildings, with roofs near to the zero-plane displacement z_d, see Figure 1.1, the influence of the interference effect up to 3 times the height of the building h could not occur and therefore, the above presented method is not directly applicable. To answer this question exacter, more wind tunnel tests or CFD simulations are necessary.

6 Influence of realistic wind shapes on the buffeting response of chimneys

In order to refine the data provided by the European standard, Clobes u. a. [2011a] analysed full scale, long term data of the natural wind field measured on a 344 m high guyed telecommunication mast located in Gartow (northern Germany). Making use of the large dimensions of the mast, wind measurements have been carried out over the entire height of the structure during more than 20 years. After evaluation of the raw data, Willecke [2013] observed that mean wind speed profiles $\bar{U}(z)$ in moderate wind speed conditions differ from the commonly used logarithmic wind profile presented in the Eurocode. A further step was made and the wind profiles were grouped in six different mean wind speed classes c, each of them with its own occurrence frequency H^c. Using this information, an analysis of vortex excitation of steel chimneys was carried out by Clobes u. a. [2011b]. The application of realistic wind profiles leads to a significant reduction in the estimation of fatigue damages compared to the current recommendations of the Eurocode.

Starting from these useful conclusions, the current work will answer an equivalent question but for gust wind buffeting loading. Therefore, not only the mean wind speed profile should be considered. The turbulence grade of the oncoming flow, represented by $\sigma_u(z)$, plays a fundamental role in the final result. Therefore, the long-term wind data from Gartow is used again to refine the wind turbulence characteristics under moderate wind conditions.

The buffeting response of steel chimneys is analysed using the Monte-Carlo technique. For this purpose, a large number of synthetic wind profiles has been generated based on the provided statistical model including the six different wind profile classes. A $\sigma_u(z)$ value has been individually assigned to each generated wind profile depending on its wind class c and mean wind speed value at $z = 156$ m. Using these profiles, the buffeting response of a 150 m high steel chimney has been separately calculated in the frequency domain using the finite element technique.

The consideration of realistic profile classes can be beneficial in a buffeting fatigue analysis, especially if a slender vertical structure is considered. Different mean wind speed profile classes include variations on the wind field acting on the structure: the mean wind force $\bar{F}(z)$, the coherence function $\gamma_{ij}(f)$ and, therefore, the aerodynamic admittance

function $|\chi(f)|^2$ are directly related to the shape of the mean wind speed $\bar{U}(z)$. Changes in the gradient form of the speed profile induce changes on the above presented functions, and consequently, on the response of the structure.

6.1 Brief description of the analysis of full scale measurements

The main contribution for this chapter was previously made by Willecke and Clobes, and published on several occasions (Clobes u. a. [2011a], Clobes u. a. [2011b]) and Willecke [2013]. Firstly, the mast Gartow and the measurement methodology are described. The classification of the mean wind speed profiles from the conditioned data is carried out using the neural network technique. The classification of the mean wind speed profiles in six different classes c is possible due to a previous training of the network. The result of the classification shows large variations of the occurrence frequency H^c of each wind profile class.

6.1.1 The 344 m high telecommunication mast Gartow

Since 1989 the Institute of Steel Structures of the Technische Universität Braunschweig operates a wind monitoring system located on the 344 m guyed mast Gartow II (northern Germany). This mast, built for telecommunication aims, has a steel cross section of 4 m by 4 m and it is guyed at four different heights. Measurements of wind speed and wind direction are carried out along its 17 anemometers and 12 wind vanes.

Figure 6.1 shows the guyed mast and its schematic draw. It depicts the position over the entire height of the anemometers, wind vanes and temperature sensors. The mast is located in a rural area in northern Germany, which corresponds to a terrain category between II and III according to the terrain classification proposed in EN 1991-1-4, and in a wind zone with a basic wind speed of $U_b = 25$ m/s. Until 2007, only the mean wind speed and standard deviation, as well as maximum and minimum values have been recorded. For the current study, data from 1989 to 2005 have been used.

A total of about 70,000 wind profiles have been measured. Some of the data contain systematic or technical errors and must be corrected. Topographic effects are also taken into account. The direction sectors used cover the main wind direction, thus the statistical representativeness of the data is not adulterated. After conditioning the raw data, 16,400 wind speed profiles remain for classification. Figure 1.7(a) shows a selection of mean wind speed profiles measured with the 17 anemometers. Low, moderate and high winds can be identified. A high scatter of mean wind speed profiles shapes can be observed.

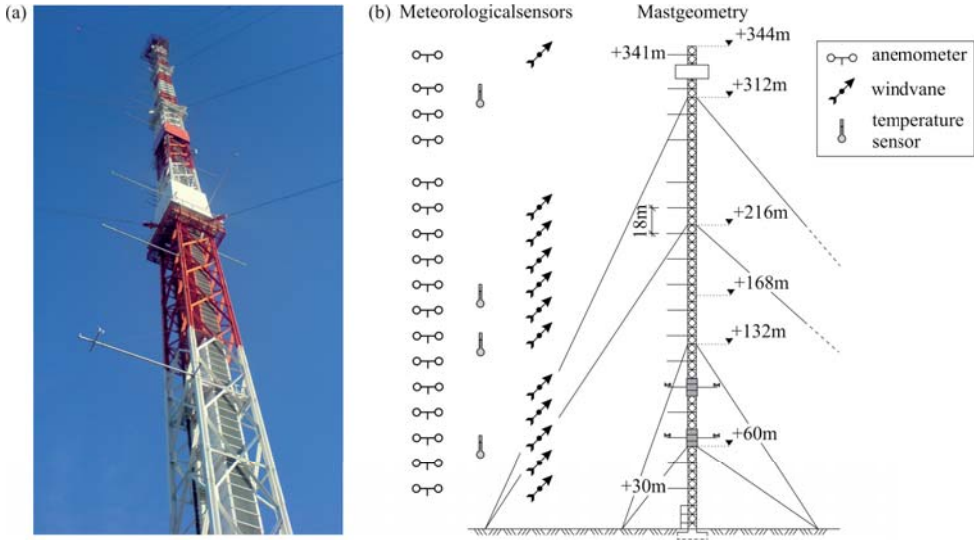

Figure 6.1: Mast Gartow II (Clobes u. a. [2011a])

6.1.2 Classification using the neural network technique

In order to quantify the influence of different wind speed profile classes on the vortex excitation, Willecke [2013] classified the long-term full scale wind profile data according to predefined characteristic profile classes. For this purpose, a trained neural network is used to classify intelligently the large number of samples. It consists of interconnected layers made up of neurons which are fully connected. An arbitrary mean wind speed profile is introduced in the network using the neurons of the input layer (each neuron correspond to each measuring level of the mast). On the output side, six neurons are defined, representing the six characteristic wind profile classes c shown in Figure 1.7(b) normalized from 0 to 1. The predefined form of the classes is decided on the basis of visual inspection of the measured wind speed profiles. The sum of the six output values is the unit and the neuron with the highest value decides the wind class of the introduced profile.

For the efficient performance of this technique, the neural network has to be previously trained. During this process, the unknown parameters of the network (weights and bias) are iteratively adjusted minimizing the error between the calculated output and the ideal output. Synthetic profiles adjusted to the six characterized forms are used as training inputs.

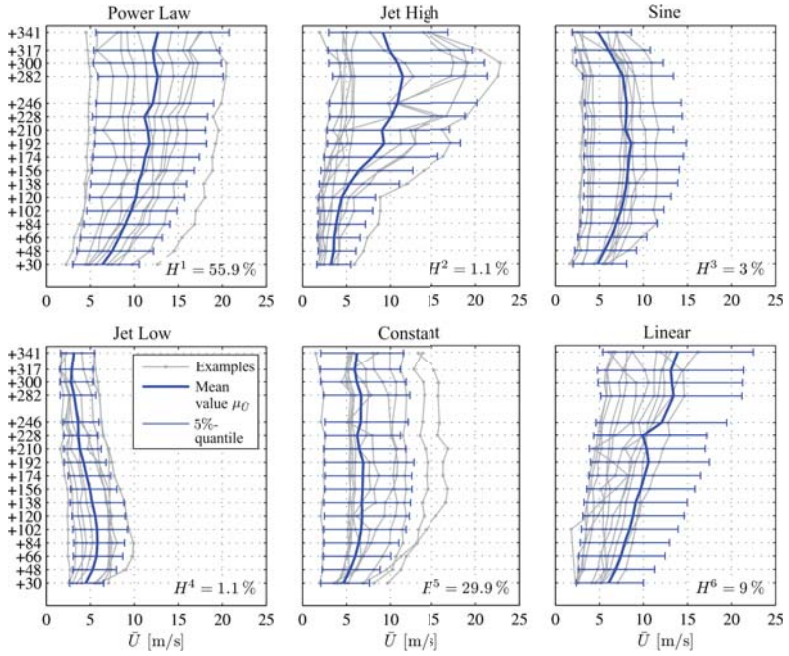

Figure 6.2: Classification results (Willecke [2013])

The results of the classification are shown in Figure 6.2 and the occurrence frequency of each class H^c is displayed in the bottom right corner of each subfigure. The blue line shows the mean value of the total mean wind profiles of each class. The grey lines represent different examples of each class and the blue bars symbolize the range of the results in terms of 5%-quintiles. The power law class profile is the most frequent wind profile class due to its occurrence frequency of 55.9%. Constant mean wind profiles are normally used for vortex excitation analysis and it has an occurrence frequency H^c of 29.9%. The observation of the jet profiles is extremely unlikely and therefore, their occurrence ratios are very low. Due to the presence of different wind classes and the large inside a wind class over the height z, the input wind field has to be covered using statistical tools.

6.1.3 Frequency distribution of the mean wind speed

In wind engineering the frequency distribution of the mean wind speed $\bar{U}$ is well described using the Weibull distribution presented in eq. 1.22. The long-term measurements at mast Gartow have shown a distribution of the mean wind speed that can be well described using

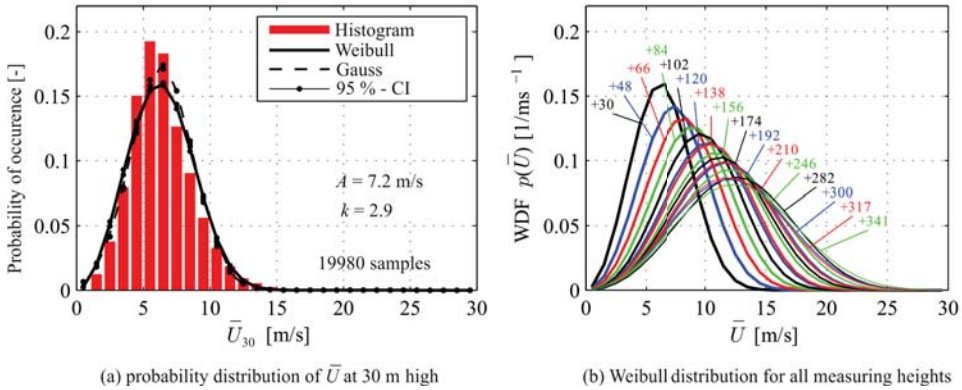

Figure 6.3: Probability distribution of the mean wind speed for power law classes (Willecke [2013])

the Weibull function. Figure 6.3(a) depicts the histogram of the mean wind speed $\bar{U}$ at 30 m high. The solid line represents the maximum likelihood of the Weibull distribution.

Nevertheless, large variations in the two parameters k and A have been observed between heights and wind directions. Figure 6.3(b) shows the Weibull distribution of $\bar{U}(z)$ for all the measuring heights, where the continuous change of the distribution shape is evident. For increasing height, the occurrence of higher wind speeds increases changing the scale parameter A.

However, according to Wieringa [1989], for $k > 3$ the characteristics of a Weibull distribution are equivalent to those of a Gaussian distribution. This fact is also illustrated in Figure 6.3(a). The approximated Weibull distribution at $z = 30$ m has a high shape parameter ($k \cong 2.9$) and can be well reconstructed using a Gaussian distribution. The consequence of a high shape parameter is the modification of the distribution form tending to a symmetric shape around the mode.

The parameters k and A obtained in Gartow and those given in EN 1991-1-4 should be carefully compared. The wind data presented in the standard is normally obtained for a normalized height of 10 m without wind characterization, which is lower than the lowest measuring height in Gartow (30 m). EN 1991-1-4 proposes a constant value of the shape parameter of $k = 2$ over the height, which is considerably lower than the value obtained from the measurements for the power law class at 30 m height. Regarding the scale parameter A, the obtained value also deviates from the definition given in EN 1991-1-4, which is based on the strong wind logarithmic profile law ($A(z) = \bar{U}(z)/5$).

The assumption of Gaussian statistics to describe the wind field at site Gartow has a set of advantages for modeling the statistical properties of the different wind classes. The Gaussian distribution allows for defining in a simpler manner the model for multivariate stochastic processes. Only the mean value μ and variance σ are necessary to cover the statistical description entirely.

Thus, each wind profile class c can be statistically represented with a mean vector $\boldsymbol{\mu}_{\bar{U}}^{c}$ and covariance matrix $\mathbf{COV}_{\bar{U}}^{c}$ The latter represents the statistical correlation of the mean wind speeds between different heights:

$$\begin{aligned} \boldsymbol{\mu}_{\bar{U}}^{c} &= \begin{bmatrix} \mu_{\bar{U}_{z1}} \\ \vdots \\ \mu_{\bar{U}_{z16}} \end{bmatrix} \\ \mathbf{COV}_{\bar{U}}^{c} &= \begin{bmatrix} \sigma_{\bar{U}_{z1}}^{2} & \cdots & \sigma_{\bar{U}_{z1}} \cdot \sigma_{\bar{U}_{z16}} \\ \vdots & \vdots & \vdots \\ \sigma_{\bar{U}_{z16}} \cdot \sigma_{\bar{U}_{z1}} & \cdots & \sigma_{\bar{U}_{z16}}^{2} \end{bmatrix} \end{aligned} \tag{6.1}$$

Figure 6.4 depicts a graphical explanation of the statistical model developed by Willecke. It can be observed how the mean vector $\boldsymbol{\mu}_{\bar{U}}^{c}$ and the relationships of standard deviations between different heights are used to build the covariance matrix $\mathbf{COV}_{\bar{U}}^{c}$. To avoid misunderstandings, it should be noted that the elements inside the covariance matrix are related to the standard deviation of the mean wind speed $\sigma_{\bar{U}}$ and not to standard deviation of the wind turbulence σ_u commonly used in wind engineering.

6.1.4 Distribution of the turbulence component

In addition to the statistical classification of the mean wind speed profiles, a definition of the wind turbulence is needed for a refined analysis of structures under buffeting wind loading. Willecke considered a constant value of σ_u over the height for each wind speed class c. In order to study the buffeting wind loading, this conclusion might not be on the safe side. Now, it is necessary to know properly how $\sigma_u(z)$ is distributed for the different wind speed classes, and if the assumption of a constant value per wind class is acceptable.

Starting from in-class pre-classified mean wind speed profiles $\bar{U}^{c}(z)$, the corresponding vectors of the standard deviation $\sigma_u^{c}(z)$ have been selected. For each wind profile class c the corresponding profiles $\bar{U}^{c}(z)$ are divided into bin widths of $\Delta\bar{U} = 5$ m/s at $z = 156$ m. $\sigma_u(z)$ remains rather constant along the height but its value increases when the mean

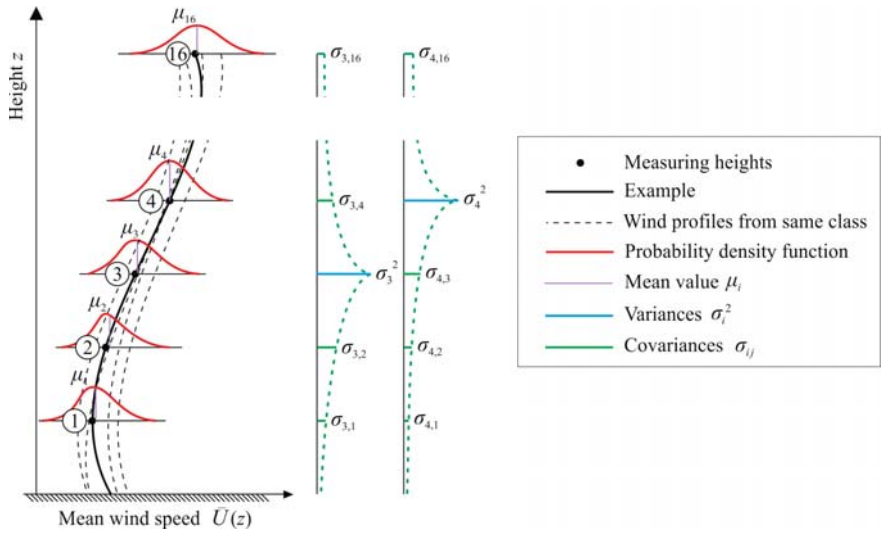

Figure 6.4: Statistical model for description of wind-class dependent wind field (Clobes u. a. [2011b])

wind speed gets higher. Consequently, a mean of standard deviations μ_{σ_u} over the height for every mean wind speed ranges and profile classes is calculated.

Figure 6.6 shows the summarized results of the evaluation of the wind turbulence for the different wind classes. The rounded points across the lines coincides with the measured values of σ_u. The lines have been plotted assuming a linear relationship between points. The duration in years of the long-term measurements has been not sufficient to record extreme wind speeds. Therefore, the dotted lines symbolize the supposed performance of σ_u for high wind speed ranges. The performance of the jet profiles is quite strange reducing the standard deviation σ_u even if $\bar{U}$ increases. The power law profile, equivalent to the logarithmic profile given in Eurocode, tends to confirm an equivalent value of σ_u as the one proposed in the standard for the location of Gartow.

The telecommunication mast is located in close proximity to the Elbe River and the surrounding area is covered with low vegetation. With the help of the CORINE Land Cover Data, an analysis of the terrain near the tower has been carried out. The obtained roughness length z_0 varies between 0.05 and 0.2 for the different direction sectors around the mast. These results suggest a direction-dependent terrain category II or III. In Figure 6.6 are plotted the values of σ_u given in the Eurocode in case of terrain category II and III for a 50-year return period wind. This kind of terrain category is also in concordance with a typical industrial area situated on city outskirts.

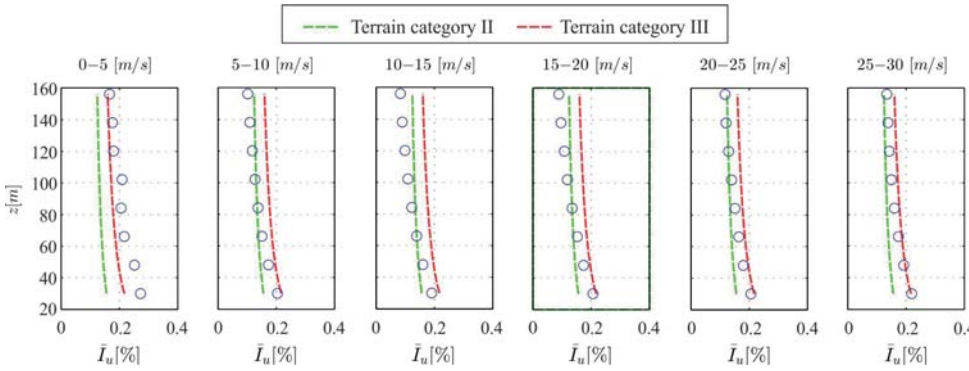

Figure 6.5: Turbulence intensity obtained for different speed ranges of the power law class

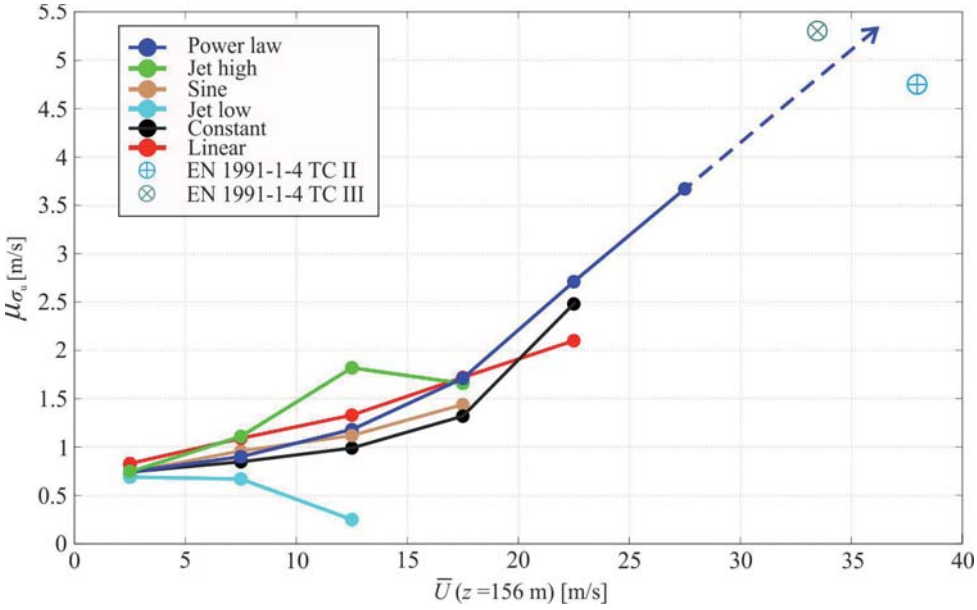

Figure 6.6: Tendency of σ_u with the mean wind speed at 156 m for the six different wind classes

Figure 6.5 depicts the calculated turbulence intensity profiles $I_u(z)$ after eq. 1.6 for the power law wind class. The green lines show the curves corresponding to a terrain category II and the red line to a TC III according to EN 1991-1-4. Except in cases of very low velocities, the profile of the turbulence intensity obtained in Gartow is comparable with an intensity profile for a terrain category between II and III. This fact was also observed by Willecke without differentiation of mean wind speed values and classes.

As shown in Figure 6.6, the other wind classes, especially the jet and sinus, tend in different way as compared with the power law and constant profiles. Therefore, a turbulence intensity profile $I_u(z)$ equivalent to the Eurocode cannot be obtained. For further details about the telecommunication mast, the neural network architecture and classification of the mean wind speed profiles see e.g. Willecke [2013].

6.2 Dynamic response of a 150 m cantilevered chimney under realistic buffeting loading

In this section, an equivalent dynamic calculation in the frequency domain as presented in Section 3.2 will be carried out. The finite element method has been applied on a chimney divided in 10 elements following the instructions given in Section 3.1.3. For the calculation, some modifications have been included, as the irregular mean wind speed shapes the input profiles or the aerodynamic admittance function $|\chi(f)|^2$.

In order to study the influence of realistic winds on the buffeting response and as a further step, on the fatigue prognosis, the implication of the different wind profile classes during its life time has to be considered. For this purpose, the statistical model previously presented will be used with the consideration of the occurrence frequency H^c of each wind profile class.

A Monte-Carlo simulation has been carried out to derive the statistic parameters of the response due to the high variability of wind speed values inside a wind class and class-dependent turbulence characteristics. In order to provide statistically firm data, a large number of simulations are needed. The total number of profiles measured in Gartow could be not enough to obtain statistically firm results. Therefore, new wind profiles have to be synthetically generated. These profiles have the same statistic characteristics than those measured in Gartow, being the covariance matrix of each wind class the starting point for the synthetic generation.

Basically, the simulated chimney is similar to the model presented in Figure 3.4 with the exception that a cantilevered structure without intermediate connection has been considered. Therefore, the natural frequencies are lower. The modal analysis have shown that the two first frequencies are located at $f_0 = 0.12$ Hz and $f_1 = 1.53$ Hz. Figure 6.7(a)

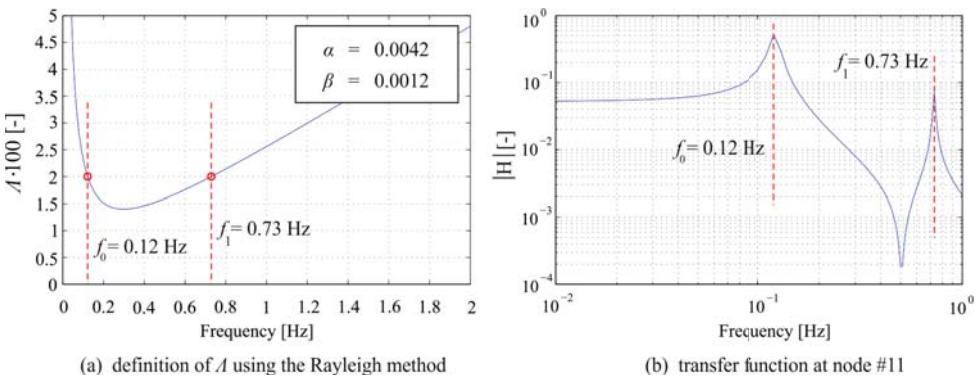

Figure 6.7: Rayleigh method (a) and transfer function at the tip of the cantilevered chimney(b)

shows the Rayleigh method for determination of the logarithm decrement of the structural damping Λ and Figure 6.7(b) the mechanical transfer function $|H(f)|$ at the typ of the chimney.

6.3 Generation of synthetic wind profiles

For a successful study about the fatigue life prognosis of steel chimneys, a large number of simulations are necessary to obtain a statistically firm solution. The profiles measured in Gartow could not be large enough in number in order to ensure the results statistically. For this purpose, synthetic wind profiles of each class are artificially generated to be used as input data for the simulation of the dynamic response of the steel chimney.

In the literature, different methods to generate correlated random vectors from a covariance matrix are presented. A quite easy method presented by Devroye [1986] uses the previously defined covariance matrix **COV**. Taking into account the theory of matrices, the covariance matrix is a positive definite matrix, and therefore it is possible to find a lower triangular nonsingular matrix **L** that yields to the following expression:

$$\mathbf{L} \cdot \mathbf{L}^* = \mathbf{COV} \tag{6.2}$$

where $\mathbf{L}^*$ denotes the conjugate transpose matrix of **L**. The selected method by Willecke for the decomposition of a symmetric positive matrix into a product of two lower triangular matrices is the Cholesky decomposition. If m vectors **r** of random variables with zero mean

and unit variance is defined at the different heights, then m synthetic correlated vectors $\mathbf{u}^c_{\mu=0}$ with zero mean are obtained for each wind class c as follows:

$$\mathbf{u}^c_{\mu=0} = \mathbf{L}^c \cdot \mathbf{r} \tag{6.3}$$

If the mean wind speed vector of each class $\boldsymbol{\mu}^c_{\bar{U}}$ is considered, then m synthetic wind profiles $\bar{\mathbf{u}}(z_i)^c$ are generated as:

$$\bar{\mathbf{u}}(z_i)^c = \mathbf{u}^c_{\mu=0} + \boldsymbol{\mu}^c_{\bar{U}} \tag{6.4}$$

The generated set of synthetic wind profiles $\bar{\mathbf{u}}(z_i)^c$ preserve the Gaussian characteristics of the initial statistical model defined by the mean vector $\boldsymbol{\mu}^c_{\bar{U}}$ and the covariance matrix $\mathbf{COV}^c_{\bar{U}}$. As shown in Willecke [2013], this method is very effective comparing the generated synthetic profiles with the real ones. The fluctuating component associated to each generated mean speed profile will be defined in the following section.

6.4 Modifications included in the process of calculation

The power spectral density function of the wind turbulence $S_{uu}(z, f)$ used in the calculation coincides with the recommendation given in the Eurocode (eq. 1.20). This variable depends on the standard deviation of the wind turbulence σ_u, and consequently on the wind profile class.

As explained in the previous section, for each wind profile generated artificially, a constant value of σ_u over the height has been assigned depending on the mean wind speed at 156 m height and on the corresponding wind profile class. Therefore, each synthetic wind profile generated according to eq. 6.4, is related to a constant power spectral density function $S_{uu}(f)$ over the height z. The nondimensional frequency $f_L(z)$ has been defined as $f_L = f \cdot T_u$. According to EN 1991-1-4 for a terrain category II, an integral time scale $T_u = 6.8$ seconds has been applied.

On the contrary to the numerical calculations presented in Section 3.2, the aerodynamic admittance function $|\chi(f)|^2$ have been now considered. In a similar way as the Eurocode, a fully correlation of pressures between the front and rear faces of the structure has been considered for the calculation, reducing $|\chi(f)|^2$ only to the crosswind R_y and vertical R_z components.

Figure 6.8 depicts the schematic view of the application of the aerodynamic admittance functions $|\chi(f)|^2$ and the coherence function $\gamma_{ij}(f)$ in the FEM program. The aerody-

namic admittance function is related to the dimensions of the area under consideration. The spectral density function of the wind forces $S_{ff_i}(z_i, f)$ applied on node i has to be multiplied by the corresponding admittance function $|\chi(z_i, f)|^2$. The wide B_j and deep D_j of the element are considered for the calculation of $|\chi(z_i, f)|^2$ and consequently, the reduced spatial correlation over the dashed area is covered. The analytical expression used for the aerodynamic admittance function is the same as in the Eurocode 1 according to eq. 4.17 with:

$$\eta_B = \frac{0.4 \cdot 11.5 \cdot f \cdot B_j}{\bar{U}_i}$$
$$\eta_H = \frac{0.4 \cdot 11.5 \cdot f \cdot \left(\frac{L_j + L_{j+1}}{2}\right)}{\bar{U}_i} \tag{6.5}$$

The inclusion of the aerodynamic admittance function in the process of calculation upgrades the importance of the simulation, including a new variable which is highly dependent on the incoming wind profile shape $\bar{U}(z)$.The entire process is depicted step by step in Figure 6.9, connecting the inputs with the outputs and providing a general overview of the complexity of the process. The structural system and wind loading are used as input data at different stages during the calculation process.

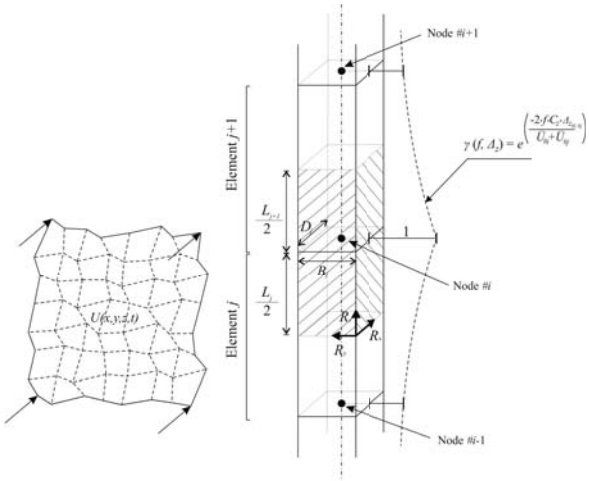

Figure 6.8: Application of $\gamma(z_i, f)$ and $|\chi(z_i, f)|^2$ to the FEM program

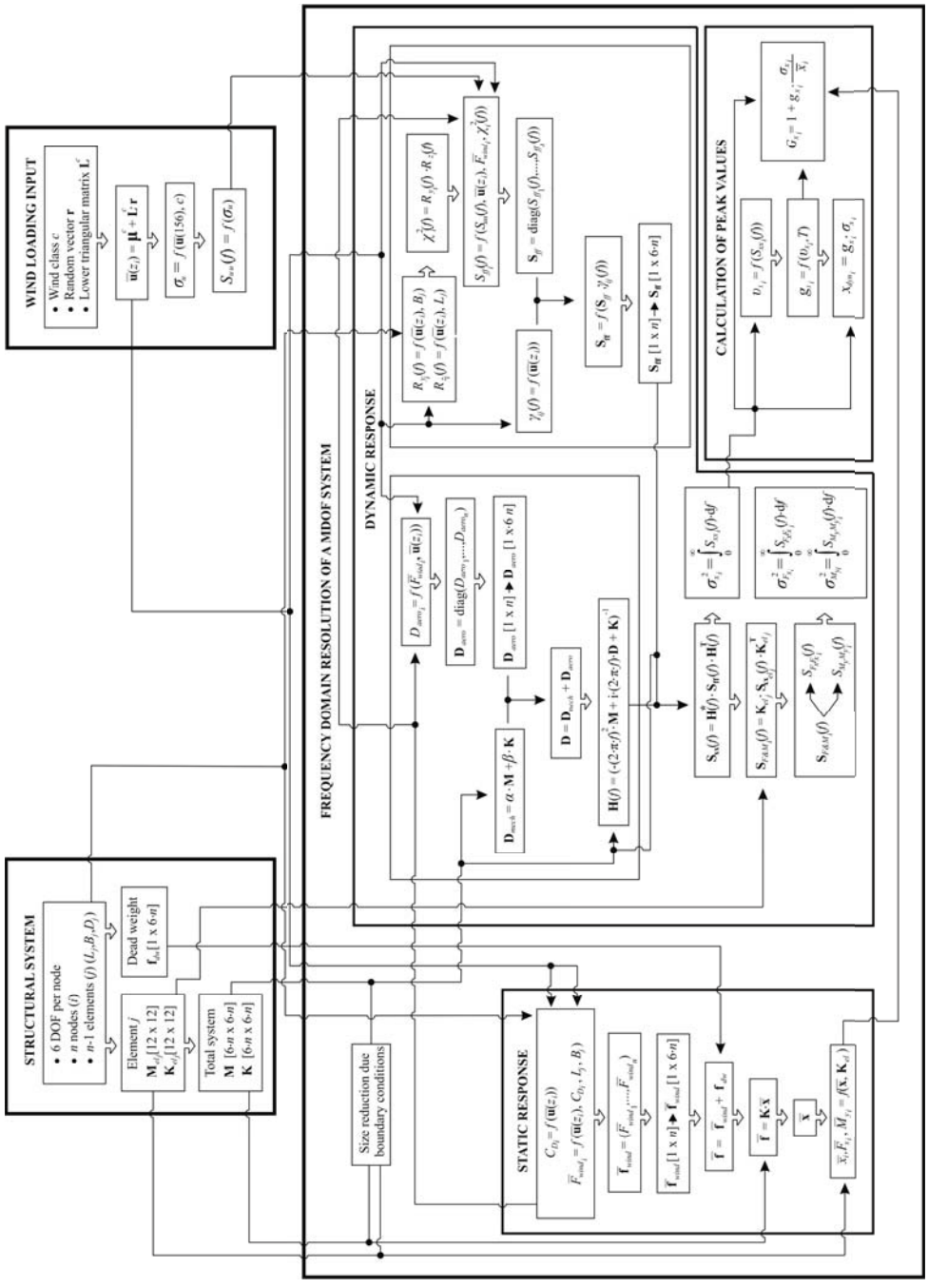

Figure 6.9: Process of calculation in the frequency domain of a MDOF system under stochastic wind action

6.5 Results of the Monte-Carlo simulation

For each synthetic wind speed profile generated applying eq. 6.4, the mean, fluctuating and maximum responses are calculated in terms of bending moment M_y at the foundation of the chimney (node #1).

The convergence of the maximum response $\hat{M}_y$, obtained according to eq. 3.17 has been considered as condition. In addition, the convergence of the fluctuating component has been also taken into account in terms of the standard deviation of the bending moment σ_{M_y}.

About 180.000 total simulations (m_{total}) have been carried out to obtain statistically stable results. The contribution of each wind profile class c has been taken into account considering their respective occurrence frequency H^c, as $m^c = m_{total} \cdot H^c$.

Figure 6.10 shows the results obtained from the Monte-Carlo simulation and the participation of the different profile classes in the buffeting response. Figure 6.10(a) illustrates the relative occurrence frequency P^c of the maximum response $\hat{M}_y$ for each wind class c. The power law and linear classes collect the wind profiles with the highest speeds and turbulence (see Figure 6.2) and therefore the largest responses are obtained. The responses caused by the jet classes are very small and concentrated on the low response ranges. The sinus and constant classes are located in the low-medium response range. Even though the linear profile class produces large bending moments at the base of the chimney, its participation in the global response is low ($H^6 = 9\%$) and its importance is dramatically reduced in comparison to the power law ($H^1 = 55.9\%$) and constant classes ($H^5 = 29.9\%$).

To consider the fatigue life of any structure, low and medium wind situations are more important due to their high occurrence frequencies. Therefore, in these cases it could be stated that the power law and constant profiles are the most important wind classes for a fatigue life analysis.

In order to optimize the calculation process of the Monte-Carlo simulation, a limitation frequency f_{cut} has been introduced as upper frequency. The huge content of data generated during the Monte-Carlo simulation can be reduced if the not essential information is neglected. For the calculation of the buffeting response, the contribution of dynamic component depends on the area located under the response spectrum. After numerical corroborations, the optimal upper frequency considered is located at $f_{cut} = 4 \cdot f_0$. Consequently, the resonant response is governed by the fundamental frequency, which is the typical behaviour under gust buffeting loading of slender structures (Holmes [2007]). Nevertheless, if the integral of the spectrum over the entire frequency range is calculated, the effective contribution of the natural frequencies higher than the fundamental is negligible, as shown in Figure 6.11.

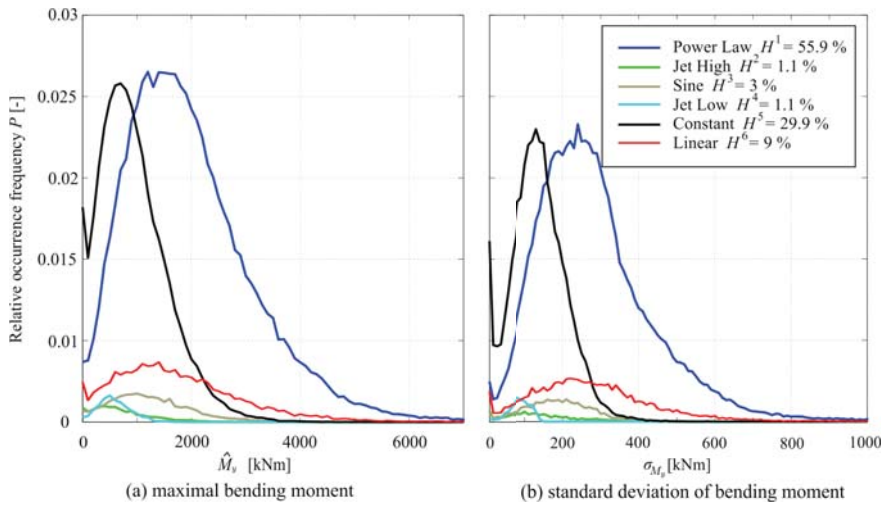

Figure 6.10: Results provided by the Monte-Carlo simulation divided into wind classes c

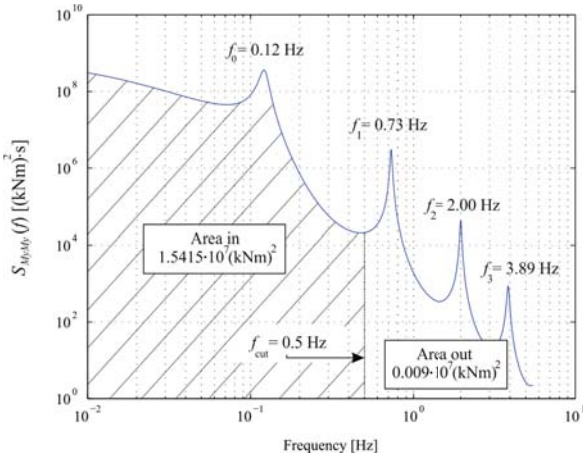

Figure 6.11: Frequency axis considered for the Monte-Carlo simulation

In case of fatigue analysis, the decision of the inclusion of an upper frequency could underestimate the number of stress amplitudes associated to the very low amplitude levels, but it is to expect that for a slender structures, where the response is dominated by the fundamental frequency f_0, this effect is diluted.

Jose Mari Sasieta. "Paisajes de viento".

7 Fatigue life prognosis considering realistic wind profile classes

The peak response of a structure under gusty wind is related to the extreme wind situations and is mathematically covered with the gust response factor or structural factor. The firsts chapters of the current work have treated this case, studying the influence produced by the interference effect on the extreme winds. But if a structure must be designed for a long lifetime, the fatigue caused by the wind has to be considered. And consequently, the main loading is governed by the medium and low wind situations.

The previous chapter has studied the influence of realistic mean wind speed shapes on the buffeting loading of industrial chimneys. The power law and linear mean wind speed profiles are responsible for the largest responses of the chimney. But for the fatigue prognosis, the occurrence frequency of each wind profile class H^c is a decisive variable to be introduced for the calculation.

The fatigue life of any structure under wind buffeting depends on the number of load cycles caused by the gusts and on the sequence in which these external loads are applied. The stochastic nature of the wind makes this analysis complex and the spectral characteristics of the incident loads determine the form and number of load cycles acting on the structure during its design lifetime. Therefore, for an efficient design of a structure under wind fatigue, a realistic load collective during its predetermined life time is necessary. Then, the load collective can be used in combination with the selected damage hypothesis to calculate the fatigue resistance of the chimney.

Kemper [2013] defines the following five parameters, which have influence on the fatigue life prognosis of each structure:

- Site-dependent wind characteristics
- Excitation by the fluid
- Structural dynamics
- Structural response
- Ultimate fatigue/strength design

These five elements are responsible for different aspects of the fatigue process, and the combination of them is necessary to asses correctly the fatigue prognosis of each structure.

EN 1991-1-4 provides an analytical solution to obtain the number of load cycles caused by gusts. Unlike the above presented list of parameters, EN 1991-1-4 shows an unique curve to determine the number of load cycles caused by gusts, without consideration of the site-dependent wind characteristics or structural dynamics. Kemper carried out a large number of numerical simulations on a SDOF linear structure with the aim of predicting the fatigue damage of slender structures for wind buffeting. The results showed a high sensitivity of the fatigue life prognosis on parameters like wind characteristics, fundamental frequency and/or damping.

Usually, the rainflow counting methodology is used to obtain a load or response collective of a structure for a given period. On the contrary to the typical rainflow methods in time domain, the spectral method of Dirlik is applied in the actual work. The information in the frequency domain provided by the Monte-Carlo simulation for each simulated wind profile has been used to calculate the probability density functions of stress ranges at the foundation of the chimney. The integration of these spectral functions over stress amplitudes ranges yields to the determination of a load collective for a certain period of time.

7.1 Number of load cycles caused by gusts presented in EN 1991-1-4

The Eurocode proposes in Annex B a method to estimate the number of times N_G that a load level ΔS is reached or exceeded during a period of 50 years (see eq. 1.23). The value ΔS is defined as the percentage to the maximum effect S_k on the structure. Figure 7.1 depicts eq. 1.23 in a logarithmic X axis.

The maximum effect S_k is a variable related with the response of the structure for an extreme wind with a return period of 50 years. This effect S_k can be interpreted as the maximum deflection of the structure $\hat{X}$ for gust buffeting, or acceleration $\hat{\ddot{X}}$, or maximum bending moment $\hat{M}_y$ etc. For an application of eq. 1.23 to a fatigue analysis, the most logical way is to transform the maximum effect S_k in a stress amplitude $\Delta\sigma_{max}$ and weight it for the different levels $\Delta\sigma_i/\Delta\sigma_{max}$ obtaining a cumulative number of occurrences $N_G(\Delta\sigma_i)$.

The formulation of the problem is not only vague in the definition itself but also in the conditions in which the corresponding expression can be used. No specifications about the site-dependent wind parameters and/or structural characteristics are necessary to use the

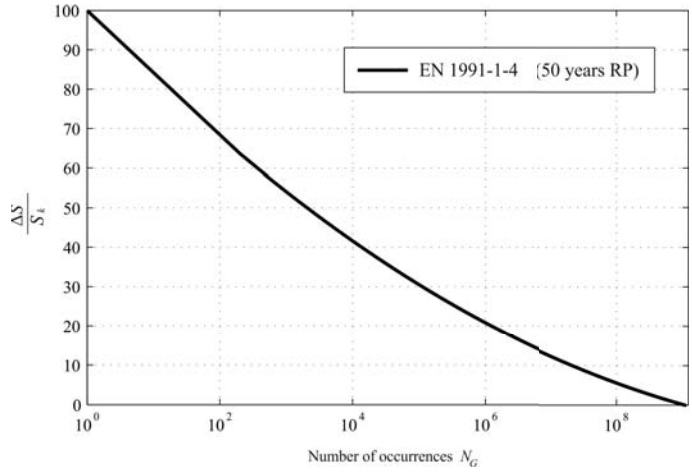

Figure 7.1: Number of gust loads N_G for the exceedance of an effect ΔS during a 50 years period (EN 1991-1-4)

formula. The unconfined use of EN 1991-1-4 seems to be imprecise and in addition, it is evident that this formulation does not take into account the occurrence of different profile classes for moderate winds. Cook [1990] affirms that the mathematical background of the curve is directly related to the mathematical method proposed by Davenport [1966]. The number of occurrences per annum in which the response of the structure is greater than a level x follows the expression:

$$N(x) = f_0 \cdot T \cdot k \cdot A^k \cdot \int_0^\infty \sigma_x^{k-1} \cdot exp\left[-A^k \cdot \sigma_x^k - \frac{x^2}{2 \cdot \sigma_x^2}\right] \cdot dx \tag{7.1}$$

where f_0 is the natural frequency of the structure, T the time period of design, A and k are the scale and shape parameter of a Weibull distribution respectively and σ_x is the standard deviation associated to the response amplitude x. This formulation is based on the assumption that the response of the structure is a Gaussian stationary process. This condition is necessary to implement the mathematical estimation of the upcrossing levels made by Rice [1945], also used for the determination of the expected frequency ν explained in the previous chapter. Therefore, the response x can be only treated mathematically as a narrow band process.

The estimation of the load cycles is derived from the probability distribution of the parent wind climate $p(\bar{U})$ in combination with the standard deviation of response process σ_x. Davenport considered that the probability distribution function of mean wind speed

$p(\bar{U})$ can be optimally represented using a Weibull distribution with $k \cong 2$ (Kemper [2013]). The joint function between mean wind distribution function $p(\bar{U})$ and response standard deviation of the response σ_x for each wind direction is defined following a systematic series of tests carried out in the wind tunnel. The probability density function of response process $p(\sigma_x)$ can also be approximated by a Weibull distribution obtaining the coefficients c and k, represented in eq. 7.1. An eventual dynamic amplification on the structure is not explicitly given, but it is supposed to be included in the response process $p(\sigma_x)$. The combination of probabilities of wind climates and response processes from wind tunnel experiments is described in detail in Davenport [1971] and Davenport [2007]. This methodology has been adopted to adjust eq. 1.23 to a return period of 50 years allowing its implementation in EN 1991-1-4.

7.2 Dirlik's method

The method of Dirlik [1985] is a wide expanded tool in mechanical engineering, which associates an arbitrary stochastic process $s(t)$ characterized by its spectral density function $S_s(t)$ and the probability density function of the rainflow ranges $p(\Delta s)$. This approach, defined entirely in the frequency domain, provides results equivalent to the rainflow counting methodology defined by Matsuishi u. Endo [1968] in the time domain. In terms of accuracy, Dirlik's formulation seems to be more precise and robust than others equivalent methods in the frequency domain presented in the literature (Halfpenny u. Kihm [2010]). The main reason for this, is its empirical origin in comparison with the other analytical formulations.

The upcrossing rate proposed by Rice yields the treatment of local maxima included in a narrow band process using a Rayleigh distribution and the density of the occurrence frequency of the rainflow ranges $N'(\Delta\sigma)$ during a period of time T. It can be determined as follows:

$$N'(\Delta\sigma) = \nu \cdot T \cdot p(\Delta\sigma) = \nu \cdot T \cdot \left[\frac{\Delta\sigma}{\sigma^2_{\Delta\sigma}} \cdot e^{\left(\frac{-\Delta\sigma^2}{2 \cdot \sigma^2_{\Delta\sigma}} \right)} \right] \tag{7.2}$$

As explained before, eq. 7.2 is only valid for structures with very low damping. However, in the case of wideband processes, it is not possible to obtain easily an analytical relationship between maximum amplitudes and rainflow ranges distribution and correction factors are normally introduced (Peil [1993]). Due to this mathematical limitation,

many engineers use the Rayleigh distribution in case of wide band processes. But this solution shows extremely conservative results as noted by Koo [2013].

To avoid this lack of information, Dirlik uses an extensive Monte-Carlo simulation to obtain an empirical method to calculate the probability density function $p(s)$ of the rainflow ranges of a stochastic signal $s(t)$ with arbitrary band width response in terms of its statistical moments m_n.

With this method it is possible to obtain the probability density function of the rainflow ranges (i.e. stress amplitudes) $p(\Delta\sigma)$ at the chimneys foundation, transforming the spectral density function of the bending moment $S_{M_yM_y}(f)$ into the spectral density function of the stress amplitudes $S_{\sigma\sigma}(f)$.

Ignoring the contribution of the normal force and dividing the bending moment $\Delta M_y(t)$ at time t by the section modulus of a circular tube W, the normal stress $\sigma(t)$ at time t is:

$$\Delta\sigma(t) = \frac{\Delta M_y(t)}{W} \tag{7.3}$$

The spectral density function of the stress amplitudes $S_{\sigma\sigma}(f)$ can be calculated applying the Fourier transform of the autocorrelation function $R_{\sigma\sigma}(t)$ of $\sigma(t)$:

$$S_{\sigma\sigma}(f) = \int_{-\infty}^{+\infty} R_{\sigma\sigma}(t) \cdot e^{(-i\cdot 2\pi\cdot f\cdot t)} \cdot dt \tag{7.4}$$

If an autocorrelation function is interpreted as a convolution in the time domain, the spectral density function $S_{\sigma\sigma}(f)$ can also be calculated multiplying the Fourier transformation $F_\sigma(f)$ of $\sigma(t)$ by the conjugated complex of the Fourier transformation $F_\sigma(\omega)^*$ of $\sigma(t)$ (Clobes u. a. [2012b]):

$$S_{\sigma\sigma}(f) = \frac{1}{T} \cdot F_\sigma(f) \cdot F_\sigma(f)^* \tag{7.5}$$

Where $F_\sigma(f)$ is calculated from bending moment $M_y(t)$:

$$F_\sigma(f) = \frac{1}{W} \cdot \int_{-\infty}^{+\infty} M_y(t) \cdot e^{(-i\cdot 2\pi\cdot f\cdot t)} \cdot dt \tag{7.6}$$

Finally, $S_{\sigma\sigma}(f)$ is can be easily determined:

$$S_{\sigma\sigma}(f) = \frac{1}{W^2} \cdot S_{M_y M_y}(f) \tag{7.7}$$

The probability density function of the stress ranges $p(\Delta\sigma)$ defined by Dirlik improves considerably the formulation made by Rice. Dirlik's approach can be used successfully for stochastic processes with any band-width. The definition of $p(\Delta\sigma)$ is based on the weighted sum of Rayleigh, modified Rayleigh and exponential probability distributions as follows:

$$p(\Delta\sigma) = \frac{\frac{D_1}{Q} \cdot e^{\left(\frac{-Z}{Q}\right)} + \frac{D_2 \cdot Z}{R^2} \cdot e^{\left(\frac{-Z^2}{2 \cdot R^2}\right)} + D_3 \cdot Z \cdot e^{\left(\frac{-Z^2}{2}\right)}}{2 \cdot \sqrt{m_0}} \tag{7.8}$$

in which:

$$D_1 = \frac{2 \cdot (x_m - \gamma^2)}{1 + \gamma^2} \qquad D_2 = \frac{1 - \gamma - D_1 + D_1^2}{1 - R}$$

$$D_3 = 1 - D_1 - D_2 \qquad Z = \frac{\Delta\sigma}{2 \cdot \sqrt{m_0}}$$

$$Q = \frac{1.25 \cdot (\gamma - D_3 - D_2 \cdot R)}{D_1} \qquad R = \frac{\gamma - x_m - D_1^2}{1 - \gamma - D_1 + D_1^2}$$

$$\gamma = \frac{m_2}{\sqrt{m_0 \cdot m_4}} \qquad x_m = \frac{m_1}{m_0} \cdot \sqrt{\frac{m_2}{m_4}}$$

$$m_n = \int_0^\infty f^n \cdot S_{\sigma\sigma}(f) \cdot df \qquad E[P] = \sqrt{\frac{m_4}{m_2}}$$

where m_n are the statistical moments and $E[P]$ symbolizes the number of peaks maxima per second or peak rate and γ is known as the irregularity factor (Bishop u. Sherrat [1989]):

$$\gamma = \frac{E[0]}{E[P]} = \frac{\text{expected number of zeros crossings}}{\text{expected number of peaks}} \tag{7.9}$$

and $E[0]$ can be calculated as follows:

$$E[0] = \sqrt{\frac{m_2}{m_0}} \tag{7.10}$$

This last expression is mathematically equivalent to eq. 3.19, which is used by Davenport in his approach. The factor γ takes values from 0 to 1 and defines the bandwidth characteristics of the stochastic process $s(t)$:

- Narrow band process $\rightarrow \gamma = 1$
- Wide band process $\rightarrow \gamma = 0$

Consequently, the frequency density of stress ranges $N'(\Delta\sigma)$ in an expected time T can be determined with Dirlik's method in following terms:

$$N'(\Delta\sigma) = E[P] \cdot T \cdot p(\Delta\sigma) \tag{7.11}$$

In other works as in Kemper u. Feldmann [2011] or Halfpenny u. Kihm [2010], the verification of the reliability of this spectral method is validated with parallel calculations using the rainflow counting method in the time domain. The spectral estimations represent excellent matches for gust excited structural responses. The number of cycles caused by gusts and damage predictions are quite identical for Dirliks method and for the rainflow counting method in time domain.

7.3 Influence of the wind profile class on the structural response

Figure 7.2(a) depicts the probability density function of the stress amplitudes $p(\Delta\sigma)$ for different generated profiles. The intention of the figure is to show the influence of the mean wind speed class on the PSD-based rainflow analysis. The curves are the result of structural calculations using a set of six random wind profiles, which correspond to each of the six different wind classes c. The dotted line represents the distribution of the stress amplitudes $\Delta\sigma$ if the logarithmic mean wind speed profile given in the Eurocode is used in the FEM program.

The randomly generated profiles of each class have been scaled to the expected mean wind speed at $z = 150$ m according to EN 1991-1-4. Consequently, Figure 7.2(a) shows the direct influence of the different wind classes on $p(\Delta\sigma)$. As shown schematically in

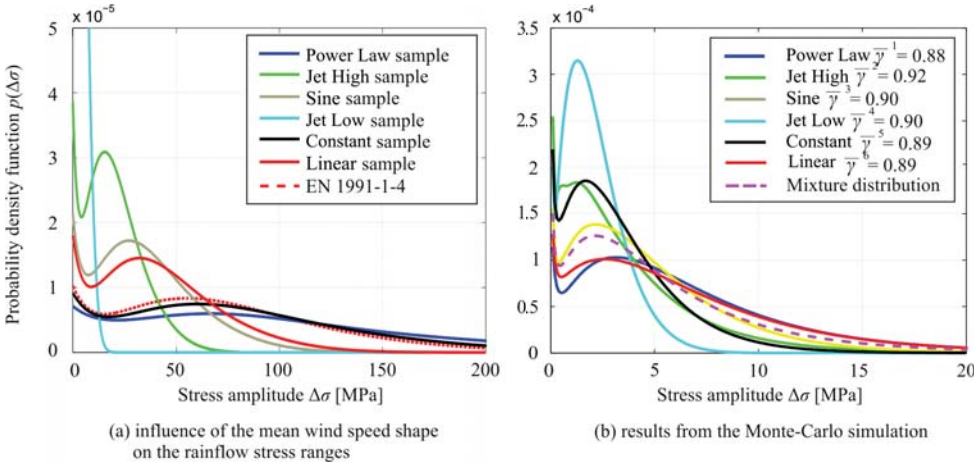

Figure 7.2: Influence of the mean wind class (a) and results obtained from the Monte-Carlo simulation (b)

Figure 6.9, the wind classes do not only have influence on the static response of the chimney. The dynamic part, which contains the fundamental information for the fatigue analysis, is also influenced by the class of the mean wind speed profile. The aerodynamic damping, as well as the coherence function $\gamma_{ij}(z, f)$, the aerodynamic admittance function $|\chi(f)|^2$ and the spectral density function of the wind forces $S_{ff}(z, f)$, are calculated at each node i or element j of the chimney, and consequently also dependent on the class of the mean wind speed profile.

In a parallel way, the given value of the standard deviation of the wind turbulence σ_u assigned to each generated wind speed profile individually, has been specified in terms of the corresponding wind class c and wind speed value at the tip of the chimney, see Figure 6.6. Therefore, σ_u, which plays a fundamental role on the fatigue prognosis under wind buffeting, can also be considered indirectly as a wind class-dependent variable.

The results showed in Figure 7.2(a) represent only a few samples to depict the application of Dirliks method for fatigue analysis in wind buffeting conditions. The high variability of the results forced the study to use the results of the Monte-Carlo simulation presented in the previous chapter in order to obtain statistically firm data.

Figure 7.2(b) shows the converged probability density function of the stress amplitudes $p(\Delta\sigma)$ provided by the Monte-Carlo simulation presented in the previous chapter. Despite the large number of necessary simulations for finding the convergence of $\hat{M}_y$ and σ_{M_y}, now "only" about 60.000 total simulations were necessary. The values of the mean irregularity

factor $\bar{\gamma}^c$ for each wind class c are also plotted. Their relatively high value confirms the form of the distributions, since most of the curves resulting from the simulation are quite similar to a Rayleigh distribution typical for narrow band processes.

For a further treatment of the fatigue life prognosis of the chimney considering realistic wind profiles, the occurrence frequencies H^c are considered. Therefore, the numerical solution provided applying Dirlik's method has been considered in terms of a mixture distribution $p_{\text{realistic}}(\Delta\sigma)$:

$$p_{\text{realistic}}(\Delta\sigma) = \sum_{c=1}^{6} H^c \cdot p_c(\Delta\sigma) \tag{7.12}$$

where $p_c(\Delta\sigma)$ are the probability distributions associated to each wind class c displayed in Figure 7.2(b). The mixture distribution is depicted with a pink dotted line. It can be observed how the curve is strongly dependent on the power law and constant profiles due to their high occurrence frequencies. The distribution mode is located in the low speed range attracted by the modes of the different wind profile classes. On the other hand, the high stress range is governed by the power law and linear profiles, because of their importance on the largest responses as shown in Figure 6.10.

7.4 Procedures to estimate the wind-induced fatigue

When a structure is subjected to external random forces as the wind, the total damage is calculated approximately using the well-known Palmgren-Miner method. The operation principle of this methodology consists in discretizing different load levels in separated damage cells and adding linearly their influence on the structure over the entire life time of the structure.

$$D = \sum \frac{n_i}{N_i} \tag{7.13}$$

D is the total damage and n_i is the number of cycles during the life time of the structure corresponding to the stress amplitude $\Delta\sigma_i$. N_i is the maximum number of cycles of stress amplitude $\Delta\sigma_i$ which causes a failure of the material. The fatigue curves are used to obtain N_i and are conceived as enveloping curves limiting the maximum number of cycles of the total amplitude levels $\Delta\sigma$.

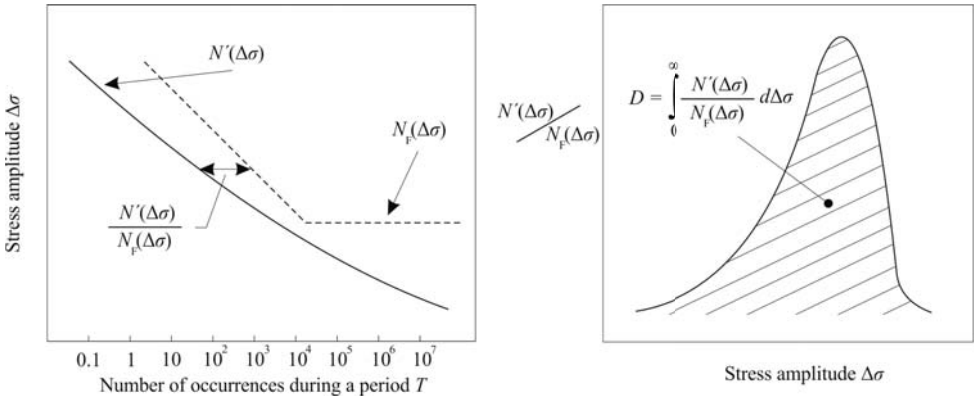

Figure 7.3: Estimation of cumulative fatigue damage due to wind action according to Palmgren-Miner law (Davenport [1966])

The common point of discussion of the different proposals given in the literature is related to a convincing approach to calculate the number of cycles n_i. Several methods are presented below.

7.4.1 Method of Davenport

The method developed by Davenport [1966] uses eq. 7.1 as the main expression to obtain the number of cycles of the amplitude stresses $\Delta\sigma_i$. The Palmgren-Miner method is applied as follows:

$$D = \int_0^\infty \frac{N'(\Delta\sigma_i)}{N_F(\Delta\sigma_i)} \cdot d\Delta\sigma_i \tag{7.14}$$

where $N_F(\Delta\sigma_i)$ is the expected number of cycles until failure at amplitude $\Delta\sigma_i$. eq. 7.1 defines the number of cycles exceeding the level x (or $\Delta\sigma_i$) in terms of a cumulative representation. To transform $N(\Delta\sigma_i)$ into a probability density function of stress amplitudes and consequently, to allow its implementation into a Palmgren-Miner hypothesis, eq. 7.1 has to be derived. Figure 7.3 depicts the application of the above explained methodology derived by Davenport to estimate the fatigue damage under wind loading during a period of design T. This method was defined under consideration of a narrow band structural response.

7.4.2 Method of Holmes

Holmes [2007] proposed a closed form solution to calculate the damage on a structure due to the wind action. In case of stochastic stress response $\sigma(t)$, the proportion of cycles with amplitudes in the range from σ to $\sigma + d\sigma$ is $p(\sigma) \cdot d\sigma$, where $p(\sigma)$ is the probability density function of the stress maxima. The total number of cycles in a period T of a narrow band process is $f_0 \cdot T$, being f_0 the fundamental frequency of the structure. Therefore, the total number of cycles with stress amplitudes in the range from σ to $\sigma + d\sigma$ is:

$$n(\sigma) = f_0 \cdot T \cdot p(\sigma) \cdot d\sigma \tag{7.15}$$

where $p(\sigma)$ is well approximated with a Rayleigh distribution. Considering K as the constant that governs the Wöhler relationship between maximum number of cycles $N_F(\sigma)$ and stress level σ:

$$N_F \cdot \Delta\sigma^m = K \tag{7.16}$$

And considering that the amplitudes of the rainflow ranges are equivalent to the double of the stress amplitudes, then the standard deviation of the rainflow ranges becomes $\sigma_{\Delta\sigma} = 2 \cdot \sigma_\sigma$. Finally, the expression of the linear accumulation of damage given in equation (4.15) yields to:

$$D = f_0 \cdot T \cdot \frac{1}{K \cdot \sigma_{\Delta\sigma}^2} \int_0^\infty \Delta\sigma^{m+1} \cdot e^{\left(\frac{-\Delta\sigma^2}{2 \cdot \sigma_{\Delta\sigma}^2}\right)} \cdot d\Delta\sigma \tag{7.17}$$

If the mathematical solution of Crandall u. Mark [1963] is applied, the integral becomes:

$$D = f_0 \cdot T \cdot \frac{1}{K} \cdot (\sqrt{2} \cdot \Delta\sigma)^m \cdot \Gamma\left(\frac{m}{2} + 1\right) \tag{7.18}$$

where $\Gamma(x)$ is the Gamma function. eq. 7.18 is derived considering a stationary process over the period of observation T without changing in the mean wind speed. To consider the varying wind speed, Holmes proposed a potential relationship between the influence of the variation of the mean wind speed and the stress value:

$$\Delta\sigma = a \cdot \bar{U}^n \tag{7.19}$$

Factor a can be defined as a modulation factor and can be numerically determined (Kemper [2013]). Exponent n depends on the resonant characteristics of the structure. The probability distribution of the mean wind speed $p(\bar{U})$ can be well described using a Weibull form. Therefore, the amount of damage caused by a range of mean wind speed from $\bar{U}$ to $\bar{U} + d\bar{U}$ can be obtained by combining equations eq. 7.18 and eq. 7.19:

$$D_{\bar{U}} = f_0 \cdot T \cdot \frac{1}{K} \cdot (\sqrt{2} \cdot a \cdot \bar{U}^n)^m \cdot \Gamma\left(\frac{m}{2} + 1\right) \cdot p(\bar{U}) \cdot d\bar{U} \tag{7.20}$$

The total damage D can be determined integrating the partial damages $D_{\bar{U}}$ over the entire spectrum of mean wind speeds:

$$D = f_0 \cdot T \cdot \frac{1}{K} \cdot \Gamma\left(\frac{m}{2} + 1\right) \cdot \int_0^\infty (\sqrt{2} \cdot a \cdot \bar{U}^n)^m \cdot p(\bar{U}) \cdot d\bar{U} \tag{7.21}$$

Using the Weibull distribution defined in eq. 1.22 and introducing a shape parameter $k = 2$, a closed form solution can be derived:

$$D = f_0 \cdot T \cdot \frac{(\sqrt{2} \cdot a)^m \cdot A^{m \cdot n}}{K} \cdot \Gamma\left(\frac{m}{2} + 1\right) \cdot \Gamma\left(\frac{m \cdot n + 2}{2}\right) \tag{7.22}$$

Consequently, this expression can be applied only in case of a narrow band process. For wide band processes, damage D can be calculated adjusting the narrow band damage with a factor λ previously determined in Wirsching u. Light [1980]:

$$D_{\text{wide band}} = \lambda \cdot D \tag{7.23}$$

7.4.3 Method of Dionne and Davenport

Dionne u. Davenport [1988] introduced a method to provide wind-induced fatigue estimates from gust factors in quasi-static design. Similarly to Holmes [2007], the response is considered as a narrow band process, but in this case the probability distribution of the mean wind speed $p(\bar{U})$ is described with a Rayleigh distribution. The final expression of the expected fatigue damage is also deduced using the Palgrem-Miner law:

$$D = f_0 \cdot T \cdot \left(\frac{\sqrt{2}}{11.5 \cdot \Delta\sigma_i}\right)^m \cdot \Gamma\left(\frac{m}{2} + 1\right) \cdot \int_0^\infty (Q \cdot K_1)^m \cdot e^{-Q} \cdot dQ \tag{7.24}$$

where K_1 is the factor proportional to the gust response factor G and it is divided into background and resonant components:

$$K_1 = \sqrt{B^2 + \frac{\pi}{4 \cdot \zeta} \cdot (2 \cdot Q)^{\beta_R}} \tag{7.25}$$

where β_R is a factor in the range 0.8 to 1.4. Factor Q represents the variation of the mean wind speed and depends on the selected Rayleigh distribution:

$$Q = \frac{1}{2} \cdot \left(\frac{\bar{U}}{\sigma_{\bar{U}}} \right)^2 \tag{7.26}$$

Unlike the approach presented by Holmes, this formulation is not given as a closed form solution but introduces explicitly the influence of the background and resonant response components on the fatigue life of the structure. As conclusion, Dionne and Davenport present a combination between gust response factor G and fundamental frequency f_0 to predict the susceptibility of a structure to wind-induced damage.

7.4.4 Method of Kemper

Kemper [2013] derives a flexible procedure to determine the number of cycles of an arbitrary stress level σ_i as function of the site-dependent characteristics and structural parameters. The $N'(\Delta\sigma)_{\text{Life}}$ function can be derived and defined as probability density function of rainflow ranges for the design time life T_{Life}:

$$N'(\Delta\sigma)_{\text{Life}} = \int_0^{\bar{U}_b} \frac{T_{\text{Life}}}{T_{\text{ref}}} \cdot N'(\Delta\sigma, \bar{U}) \cdot p(\bar{U}) \cdot d\bar{U} \tag{7.27}$$

where T_{ref} is defined as the reference time period in which the influence of the mean wind speed $\bar{U}$ is considered. In comparison with the other formulations, the integrand is integrated up to the basic wind velocity $\bar{U}_b$ defined in EN 1991-1-4 with a 50 years return period showing a clear intention to use the $N'(\Delta\sigma)_{\text{Life}}$ function as design tool for the structural engineers.

Kemper calculated numerically for a SDOF system the matrix containing the probability density function of the rainflow ranges $N'(\Delta\sigma, \bar{U})$ for different wind speed ranges using Dirliks method according to eq. 7.11.

In case of SDOF systems with basic linear assumptions, the matrix $N'(\Delta\sigma, \bar{U})$ can be approximated supposing a linear relationship between response level and applied mean

wind speed over the structure. Hence, it is only necessary for the calculation of $N'(\Delta\sigma, \bar{U}_b)$ for the basic wind speed $\bar{U}_b$:

$$N'(\Delta\sigma)_{\text{Life}} = \int_0^{\bar{U}_b} \frac{T_{\text{Life}}}{T_{\text{ref}}} \cdot N' \left(\Delta\sigma \cdot \frac{\bar{U}^2}{\bar{U}_b^2} \right) \cdot \frac{\bar{U}_b^2}{\bar{U}^2} \cdot p(\bar{U}) \cdot d\bar{U} \tag{7.28}$$

Due to its definition as probability density function, $N'(\Delta\sigma)_{\text{Life}}$ can be directly implemented in the Palgrem-Miner law as follows:

$$D = \int_0^{\Delta\sigma_{\max}} \frac{N'(\Delta\sigma)_{\text{Life}}}{N_F(\Delta\sigma)} \cdot d\Delta\sigma \tag{7.29}$$

where $\Delta\sigma_{\max}$ is the maximum stress amplitude that appears on the structure due to a wind action characterized by the basic wind speed $\bar{U}_b$. The comparison of the $N'(\Delta\sigma)_{\text{Life}}$ function with the time domain computations shows an excellent agreement in the damage prognosis (Kemper u. Feldmann [2011]). Kemper's method is also compared with the above presented methodology of Holmes. The results are in good concordance, but with increasing natural frequencies and bandwidth, both methodologies diverge.

For a direct comparison of this method to the proposal given in EN 1991-1-4 defined in eq. 1.23, an integration of the $N'(\Delta\sigma)_{\text{Life}}$ function over the entire amplitude ranges is necessary:

$$N(\Delta\sigma)_{\text{Life}} = \int_0^{\Delta\sigma_{\max}} N'(\Delta\sigma)_{\text{Life}} \cdot d\Delta\sigma \tag{7.30}$$

The integration yields to the transformation of a probability density function into a cumulative distribution function as given in the Eurocode. Now, $N(\Delta\sigma)_{\text{Life}}$ and N_G can be directly compared.

7.5 Damage prediction considering different wind classes

The above presented methods use the methodology derived by Davenport [1966], where the number of cycles of a given stress level $\Delta\sigma_i$ is obtained from a combination between the probability distribution of the mean wind speed $p(\bar{U})$ and the additional probability

between response level and mean wind speed $p(\Delta\sigma_i \cap \bar{U})$. Therefore, the load cycles during the design life of the structure are determined in terms of a conditional probability:

$$p(\Delta\sigma_i \mid \bar{U}) = p(\Delta\sigma_i \cap \bar{U}) \cdot p(\bar{U}) \tag{7.31}$$

In order to predict the fatigue damage within the design life time of the chimney, the number of cycles $N'(\Delta\sigma)_{\text{Life}}$ of each stress level bin $\Delta\sigma_i$ has to be derived for its application to the Palmgren-Miner law. The conditional probability described in eq. 7.31 is usually applied in the literature as in Kemper [2013], Peil u. Behrens [2000] and Petersen u. Reppermund [1986], calculating the maximum response for a given design wind speed and compensating it over the statistical distribution of the mean wind speed. In the current work, the results obtained from the Monte-Carlo simulation include internally these two components. Hence, the probability density function $p(\Delta\sigma_i)$ obtained from Dirlik's method inside a Monte-Carlo simulation includes the main goal of the current work. Contrary to the other works presented in the literature, the information contained in frequency density function $p(\Delta\sigma_i)$ includes the realistic wind profiles, their occurrence frequency H^c and the effect of the wind class over the entire structure. Consequently $N'(\Delta\sigma_i)_{\text{Life}}$ can be determined as follows:

$$N'(\Delta\sigma_i)_{\text{Life}} = E[P] \cdot T_{\text{Life}} \cdot p_{\text{realistic}}(\Delta\sigma_i) \tag{7.32}$$

where T_{Life} is the number of seconds over the entire design life of the structure and $p_{\text{realistic}}(\Delta\sigma_i)$ obtained according to eq. 7.12.

One advantage of working with probability density functions is the possibility of the direct analytical calculation of the fatigue damage. If the reduction of the constant amplitude fatigue limit $\Delta\sigma_D$ to its cut-off limit $\Delta\sigma_L$ is considered, a tri-linear Wöhlers law of fatigue damage can be applied to the determination of $N_F(\Delta\sigma)$. Consequently, eq. 7.29 can be divided in two components:

$$D = \int_{\Delta\sigma_L}^{\Delta\sigma_D} \frac{N'(\Delta\sigma_i)_{\text{Life}} \cdot d\Delta\sigma_i}{N_D \cdot \left(\frac{\Delta\sigma_D}{\Delta\sigma_i}\right)^{m_2}} + \int_{\Delta\sigma_D}^{\infty} \frac{N'(\Delta\sigma_i)_{\text{Life}} \cdot d\Delta\sigma_i}{N_D \cdot \left(\frac{\Delta\sigma_D}{\Delta\sigma_i}\right)^{m_1}} \tag{7.33}$$

In case of engineering solutions, this last equation is normally used with a discretization of the continuous stress amplitude spectrum into a finite number m of stress ranges of width $\Delta\sigma_w$. This can be obtained with the integration of the probability density function

$N'(\Delta\sigma_i)_{\text{Life}}$ obtaining a discretized load collective for each stress amplitude $\Delta\sigma_{m,i}$ (Kemper [2013]):

$$D = \sum_{i=k_L}^{k_D} \frac{\int_{\Delta\sigma_{m,i}-\frac{\Delta\sigma_w}{2}}^{\Delta\sigma_{m,i}+\frac{\Delta\sigma_w}{2}} N'(\Delta\sigma_i)_{\text{Life}} \cdot d\Delta\sigma_i}{N_D \cdot \left(\frac{\Delta\sigma_D}{\Delta\sigma_i}\right)^{m_2}} + \sum_{i=k_D}^{m} \frac{\int_{\Delta\sigma_{m,i}-\frac{\Delta\sigma_w}{2}}^{\Delta\sigma_{m,i}+\frac{\Delta\sigma_w}{2}} N'(\Delta\sigma_i)_{\text{Life}} \cdot d\Delta\sigma_i}{N_D \cdot \left(\frac{\Delta\sigma_D}{\Delta\sigma_i}\right)^{m_1}} \tag{7.34}$$

where k_L and k_D are the class indexes i which correspond to the stress levels $\Delta\sigma_L$ and $\Delta\sigma_D$.

7.5.1 Determination of the load collective

Starting from the mixture distribution shown in Figure 7.2(b), a load collective is calculated considering the realistic wind characteristics. The collective is derived integrating $N'(\Delta\sigma)$ in different load steps or from a cumulative distribution function for the design lifetime of the structure.

Due to the initial formulation of the current work, the wind speed distribution, the occurrence frequency of each wind profile class H^c and the mechanical characteristics of the structure are implicit in the mixture distribution $p_{\text{realistic}}(\Delta\sigma)$. The load stress can be calculated integrating the probability density function as follows:

$$N(\Delta\sigma > \Delta\sigma_i)_{\text{Life}} = E[P] \cdot T_{\text{Life}} \cdot \int_{\Delta\sigma_i}^{\infty} p_{\text{realistic}}(\Delta\sigma) \cdot d\Delta\sigma \tag{7.35}$$

where T_{Life} is the design lifetime in seconds.

The parent distribution of the mean wind speed used for the definition of $p_{\text{realistic}}(\Delta\sigma)$ shows an excellent behaviour to describe the low and moderate wind conditions. But the distribution of the extreme values is not well covered. Peil u. Nölle [1995] noted that for probabilities of occurrence lower than 0.01, the Weibull distribution is not an effective tool to represent extreme winds and the application of equation eq. 7.35 at these amplitude ranges is highly questionable. In a same way to the Weibull, the Gaussian distribution used for the determination of class-dependent mean wind speed vector $\boldsymbol{\mu}_{\bar{U}}^c$ and covariance matrix $\mathbf{COV}_{\bar{U}}^c$ seems to be not enough reliable for the generation of extreme values if a fatigue prognosis during 50 years design life of the structure will be calculated.

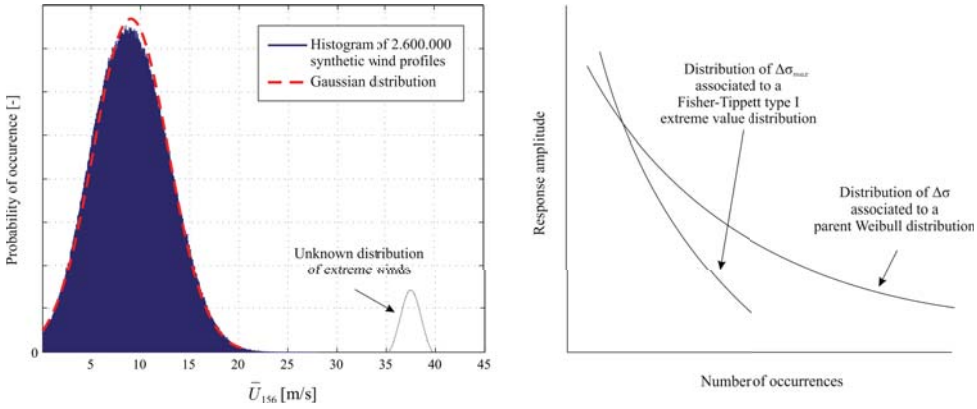

Figure 7.4: Histogram of 50 years winds (a) and influence of the distribution on the load collective (b)

Table 7.1 shows the differences in the maximum expected value between the Eurocode and Gartow. Taking into account, that the maximum wind is reached or exceeded once in 50 years, their probability of appearance can be defined as $p = 1/2,628,000$. Making use of the Weibull distribution, the expected wind speed $\bar{U}_e$ can be defined as:

$$e^{-\left(\frac{\bar{U}_e}{A}\right)^k} = \frac{1}{2628000} \tag{7.36}$$

The large shape parameters observed in Gartow are helpful to transform the probability density function from a Weibull distribution to a Gaussian. With this step, the low and medium ranges are correctly covered but the expected extreme winds $\bar{U}_e$ are in comparison to EN 1991-1-4 clearly underestimated. The values of k and A for each height have been obtained from Willecke [2013].

	k	A	$\bar{U}_{EC1}$	$\bar{U}_e$
$z = 30$ m	2.9	7.2	30.4	18.2
$z = 150$ m	3.3	12	38	27.1

Table 7.1: Differences observed in case of extreme winds

Clobes [2008] carried out an extreme value study using the measured data in Gartow. For each anemometer of the mast, the Fisher-Tippett-I distribution of the measured wind is defined to obtain the 50 years return period wind speed. In case of the anemometer located at a height of $z = 156$ m, the expected wind speed is approximately 38 m/s, which coincides very well with the mean wind speed given in the Eurocode for a terrain category II and wind zone II. Using the analysis made by Clobes, a set of extreme values have been manually added to the group of synthetic wind profiles generated using the mean vector and covariance. With this assumption, a direct comparison between these results and the Eurocode proposal can be done.

In order to obtain a conclusion about the real influence of the six different profile classes on the fatigue prognosis, it is necessary to compare the results obtained if only the power law class is considered with those results if the six different classes are included. Figure 7.5 depicts the load collective obtained for a time period of 50 years for the 150 m high cantilevered chimney virtually built in Gartow. The blue line represents the load collective for a time period of 50 years if only the presence of the power law class is considered. The red line is obtained under consideration of the six different wind profile classes c. This latter curve cannot reach at intermediate load levels the blue curve. This fact demonstrates that the consideration of six different profile shapes during the calculation can yield to more economical solutions for the fatigue than if only the power law shape is considered. Each of both curves were obtained after calculation of the structural response for more than 100.000 synthetic wind profiles.

The black line represents the overestimated solution provided by the Eurocode and discussed in Section 7.1. The green line represents the analytical solution defined by Kemper [2013] to determine a 50 years load collective depending on the fundamental frequency of the structure f_0, the scale parameter k of the Weibull distribution from site and the logarithmic decrement of the structural damping Λ.

7.5.2 Differences in the expected damage

In this section, a short comparison of the expected damage of a 150 m high cantilevered chimney depending on the selected method is provided. The total damage is calculated using the Palmgren-Miner method presented in eq. 7.13. The reduction of the constant amplitude fatigue limit $\Delta\sigma_D$ to its cut-off limit $\Delta\sigma_L$ is considered by obtaining a tri-linear Wöhler law.

For the discretization of the load levels, 10 different stress bins have been taken into account. Figure 7.6(a) shows the accumulation of damage for a design period of 50 years and a fatigue detail category of $\Delta\sigma_c = 71\ \mathrm{N/mm^2}$ according to EN 1993-1-9. The expected damage using the approach of the Eurocode is $D_{EC} = 3.89$. If the unique presence of

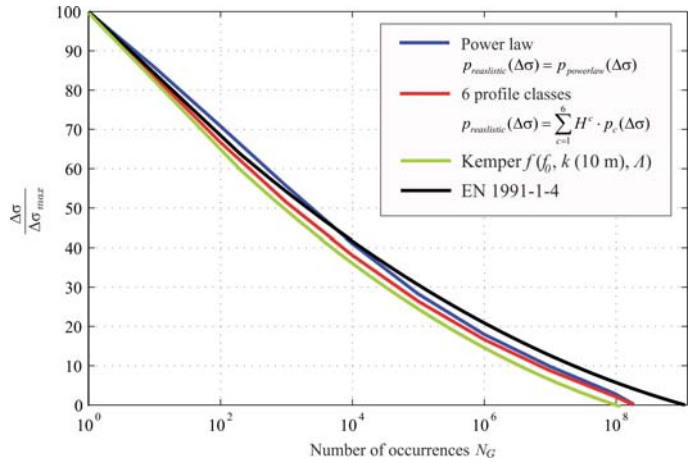

Figure 7.5: Comparison of load collectives

power law wind profiles is considered, an expected damage of $D_{PL} = 1.63$ is reached, while if the presence of six profile classes is assumed, a damage of $D_{6WC} = 1.22$ is determined.

As explained in the introduction, the proposal of the Eurocode cannot be directly compared with the statistical method of the actual work due to impossibility of managing structural parameters or wind-site statistics. Therefore, for a logical comparison, only the cases between only power law and six wind classes can be considered. For this purpose, the factor R_D, which compares the expected damage on the same structure using both methods, is defined as follows:

$$R_D = 1 - \frac{D_{6\text{ wind classes}}}{D_{\text{power law}}} \tag{7.37}$$

Figure 7.6(b) shows the factor R_D of the damage depending on the logarithmic decrement of structural damping Λ. The sensitivity analysis have shown that the logarithmic damping of the structure is less important for the expected damage prediction due to its low influence on R_D. That can be related with its relative importance in comparison to the aerodynamic damping, which becomes more important in case of slender structures. The consideration of six wind profiles classes reduces the expected damage in about 25% comparing if only power law shapes are considered. Nevertheless, this conclusion cannot be extrapolated to each structure. The separation of mean wind speed profiles on six different shapes can only be understand due to the height of the guyed mast Gartow. In case of a smaller structure, e.g. 50 meters high chimney, no real differences can be observed

between a power law profile and the others. On the other hand, if a higher chimney has to be studied, e.g. 300 meters high, the differences between wind classes become larger and therefore, the expected damage will be clearly different than if only the power law shape is considered. The definition of a height-dependent factor R_D is necessary to provide an useful engineering-application. Currently, this study is being carried out at the Institute of Steel Structures of the TU Braunschweig.

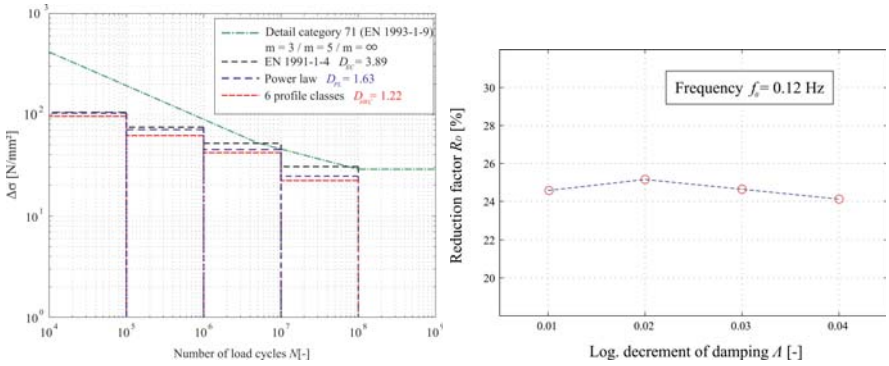

(a) Damage accumulation for node node #1 (b) Factor R_D for different damping grades

Figure 7.6: Study on the expected damage

8 Conclusions and outlook

The work presented here discusses about the gust buffeting design of industrial steel chimneys. The main topics studied in the current work are related to firstly, the disturbance produced by an adjacent building on the wind loading and secondly, the influence of realistic wind shapes on the fatigue prognosis of the structure.

In wind engineering, the disturbance on the wind flow due to the presence of a body is known as the interference effect. This phenomenon has been studied in the boundary layer wind tunnel of the Institute of Steel Structures of the Technische Universität Braunschweig. Due to the high sensitivity of some variables to external disturbances, a parametric study has been carried out. A large number of experimental tests have been carried out to achieve the change of the wind structure acting on the chimney due to the presence of a large nearby building. For this purpose, different power house shapes, different positions of the chimney with respect to the building and a varying wind direction have been considered. In order to provide new design formulas to cover the dynamic amplification produced by the interference effect, an analytical proposal for the disturbed mean wind speed profile $\bar{U}_d(z)$ is given depending on the type of building, position of the chimney and wind direction θ.

The results show an acceleration of the mean wind speed up to 3 times the height of the nearby building. The turbulent component also suffers important modifications, characterized by an increase of the standard deviation σ_u provoked by the vortex separation caused by the sharp edges of the building. In order to qualitatively show the influence of the disturbed flow on an industrial chimney, the dynamic response of a 150 m high propped chimney is calculated in the frequency domain under quasi-static assumptions. The inputs used for the simulation are those obtained from the wind tunnel experiments, and the results show a high variability with the wind direction θ. For the simulated chimney, the most adverse configuration provokes an increase up to 10 % on the bending moments with respect to the undisturbed flow conditions.

The influence of the interference effect on the aerodynamic admittance function $|\chi(f)|^2$ is also determined. Using a carbon fibre model of an industrial chimney and, considering the Reynolds number effect on the drag coefficient C_D, the forces and bending moments acting on the chimney are measured using the high frequency force balance. The aerodynamic admittance function $|\chi(f)|^2$ is identified and compared with the proposals given

in the literature for undisturbed wind conditions. It does not suffer remarkable changes with respect to the configuration without nearby building. Only in several configurations, related to the local increase of turbulence due to the vortex separation on the corners of the adjacent building, an increase of $|\chi(f)|^2$ is observed.

The mathematical background of the gust response factor G_x has been broken down and the influence of the disturbed flow in terms of $\bar{U}_d(z)$ has been inserted. The maximum response of a chimney under interference conditions has been determined in terms of a reference gust response factor $G_{x,0}$ calculated according to the current norm, a disturbed mean response calculated from the disturbed mean wind speed $\bar{U}_d(z)$ and new factor IF_{G_x} that covers the dynamic amplification produced by the interference effect. Contrary to the code, the maximum response of a propped chimney can also be now computed. In addition, the solution can be determined depending on the position of the chimney, on the ratio H^*/h, on the fundamental frequency of chimney f_0 and on the structural damping ratio ξ.

Regarding the fatigue life prognosis under gust buffeting loading, the proposal according to EN 1991-1-4 and a new proposal based on wind long-term wind profile statistics are compared. For this purpose, the wind data provided by Willecke at site Gartow, equivalent placement to an industrial area, is used. For this purpose, a Monte-Carlo simulation has been carried out to provide statistically firm data. A large number of synthetic wind profiles has been generated using the mean vector $\boldsymbol{\mu}_{\bar{U}}^{c}$ and the covariance matrix $\mathbf{COV}_{\bar{U}}^{c}$. These variables were separately defined for each wind class c classified by Willecke after 20-year wind measurements at the 344 m high telecommunication mast in Gartow. From these data, a classification of the standard deviation of the wind turbulence σ_u is also performed. This last variable is fundamental in the buffeting loading process and should be carefully considered. A unique realistic value of σ_u is separately assigned for each synthetic wind speed profile.

A 150 m high cantilevered chimney has been simulated and its dynamic response to wind buffeting calculated considering the realistic wind profile shapes. The model has been generated as realistically as possible including the influence of the aerodynamic damping, as well as the inclusion of several wind profile shape-dependent variables, thus making the simulation as precise as possible. The final results provided by the Monte-Carlo simulation show a clear differentiation between the wind classes c on the response of the chimney. Power law class and linear class produce the largest response as compared with other wind classes. But for the fatigue prognosis, the high occurrence frequency H^c of the power law class and constant class reduces the influence of the other wind classes in the overall response.

In order to study the expected fatigue damage of the structure, Dirlik's method has been applied. This flexible method, defined entirely in the frequency domain, yields to

the calculation of the probability distribution of the stress amplitudes $p(\Delta\sigma)$ directly from the spectral information of the bending moment at the foundation. This method is characterized by its accuracy being a combination of different probability distributions allowing its application to every stochastic process and arbitrary band width. The resulting probability distribution of the stress amplitudes $p_{\text{realistic}}(\Delta\sigma)$ is obtained considering the occurrence frequency of each wind class c.

The load collective obtained from the Monte Carlo simulation has been used to determine the expected damage of the chimney. The consideration of six wind classes yields to a more economic design comparing to a scenario for which only the power law wind profile shape is considered. In case of the 150 m high steel chimney, the consideration of six classes can reduce the expected damage up to 25% with respect to the situation if only the power law class is considered. The proposal provided by the Eurocode is a stiff tool, avoiding the engineer the selection of the wind site or structural characteristics and does not seem to be the best solution for the realistic calculation the expected damage. Looking at the definition of the parent statistical model, it is to expect that if the height of the structure increases, the differences in the expected damage between six wind classes and only power law should be higher. Investigations to demonstrate quantitatively this conjecture are currently being carried out.

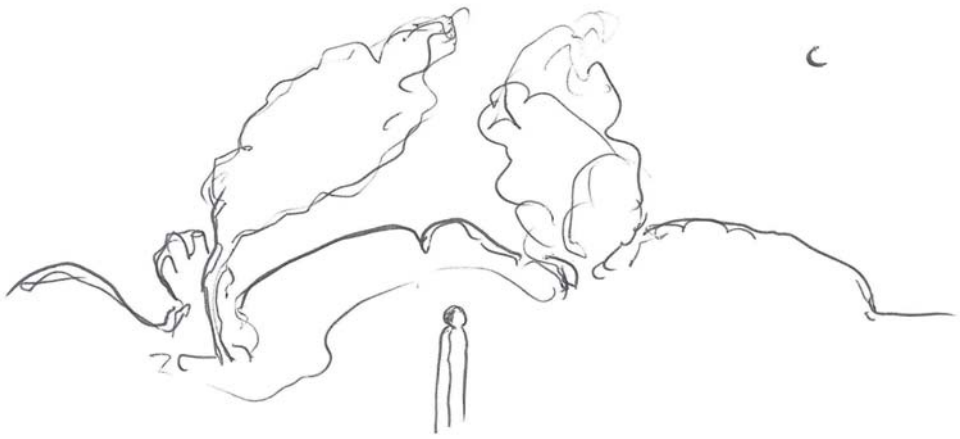

Jose Mari Sasieta. "Paisajes de viento".

Bibliography

[AIJ] *RLB Recommendations for Loads on Buildings. Structural Standards Committe. Architectural Institute of Japan (AIJ)*

[Aizpurua Aldasoro & Clobes 2013] Aizpurua-Aldasoro, H. ; Clobes, M.: Fatigue prognosis for chimneys under long-term wind profile statistics. In: *CICIND Report - Technical Meeting in Rio de Janeiro, Brazil* 29-2 (2013)

[ASCE 1999] *Wind Tunnel Studies of Buildings and Structures.* ASCE Manuals and Reports on Engineering Practice No. 67. Aerospace Division, 1999

[ASCE 7-05] *ASCE 7-05 Minimum Design Loads for Buildings and Other Structures. Part 6: Wind Loads. American Society of Civil Engineers*

[AS/NZS 1170.2:2011] *Structural design actions. Part 2: Wind actions. Standards Australia Limited/ Standards New Zealand 2011*

[Barre & Barnaud 1995] Barre, C. ; Barnaud, G.: High reynolds number simulation techniques and their application to shaped structures model test. In: *Journal Of Wind Engineering And Industrial Aerodynamics* 57 (1995), p. 145–157

[Batham 1973] Batham, J. P.: Pressure distributions on circular cylinders at critical Reynolds numbers. In: *Journal of Fluid Mechanics* 57 (1973), p. 209–228

[Behrens 2004] Behrens, M.: *Aerodynamische Admittanzansätze zur Böenwirkung auf hohe, schlanke Bauwerke*, Technische Universität Braunschweig, Germany, PhD-thesis, 2004

[Bishop & Sherrat 1989] Bishop, N. W. M. ; Sherrat, F.: Fatigue life prediction from power spectral density data. Part 1: traditional approaches. In: *Enviromental Engineering* 2 (1989), p. 11–14

[Boggs 1991] Boggs, D. W.: *Wind loading and response of tall structures using aerodynamic models*, Colorado State University, Fort Collins, Colorado, PhD-thesis, 1991

[Boggs & Peterka 1989] Boggs, D. W. ; Peterka, J. A.: Aerodynamic Mode Tests of Tall Buildings. In: *Journal of Engineering Mechanics* 115 (1989), p. 618–635

[Bowen 1979] Bowen, A. J.: *Some effects of escarpments on the atmospheric boundary layer*, Department of Mechanical Engineering, Univ. of Canterburry, Christchurch, New Zealand., PhD-thesis, 1979

[Bowen & Lindley 1977] Bowen, A. J. ; Lindley, D.: A wind-tunnel investigation of the wind speed and turbulence characteristics close to the ground over various escarpment shapes. In: *Boundary-Layer Meteorology* 12 (1977), p. 259–271

[Buresti 1981] Buresti, G.: The effect of surface roughness on the flow regime around circular cylinders. In: *Journal Of Wind Engineering And Industrial Aerodynamics* 8 (1981), p. 105–114

[Cermak 1958] Cermak, J. E.: Wind Tunnel for the Study of Turbulence in the Atmospheric Surface Layer. Tech. Rept. CER58JEC42 / Fluid Dynamics and Diffusion Laboratory, Colorado State University, Fort Collins. 1958. – Research report

[Cermak 2003] Cermak, J. E.: Wind-tunnel development and trends in applications to civil engineering. In: *Journal of Wind Engineering and Industrial Aerodynamics* 91 (2003), p. 355–370

[Clobes 2008] Clobes, M.: *Identifikation und Simulation instationärer Übertragung der Windturbulenz im Zeitbereich.* Shaker Verlag, 2008

[Clobes et al. 2012a] Clobes, M. ; Aizpurua-Aldasoro, H. ; Peil, U.: Interference Effects of Power Houses on Slender Steel Chimneys / CICIND. 2012. – Research report

[Clobes et al. 2012b] Clobes, M. ; Höbbel, T. ; Willecke, A.: 20 Jahre Windfeldmessungen am 344 m hohen Fachwerkgittermast Gartow II - Die Struktur des natürlichen Windes. In: *VDI - Berichte Nr. 2160, Kassel.*, 2012, p. 595–606

[Clobes et al. 2011a] Clobes, M. ; Willecke, A. ; Peil, U.: Shape-dependent characteristics of full-scale wind profiles. In: *Journal of Wind Engineering and Industrial Aerodynamics* 99 (2011), p. 919–930

[Clobes et al. 2011b] Clobes, M. ; Willecke, A. ; Peil, U.: Vortex-induced vibrations of slender structures considering long-term wind profile statistics. In: *Proc. of the 8th International Conference on Structural Dynamics, EURODYN, Leuven, Belgium* (2011), p. 1599–1606

[Clough & Penzien 1993] Clough, R.W. ; Penzien, J.: *Dynamics of Structures.* McGraw-Hill, Inc., 1993

[Cook 2007] Cook, N.: *Designer's Guide to EN 1991-1-4.* Thomas Telford, 2007

[Cook 1983] Cook, N. J.: A sensisitive 6-component high-frequency-range balance for building aerodynamics. In: *Journal Of Physics E: Scientific Instruments* 16 (1983), p. 390–393

[Cook 1985] Cook, N.J. ; Establishment, Building R. (Hrsg.): *The designer's guide to wind loading of building structures. Part 1: background, damage survey, wind data ams structural classification.* Butterworth-Heinemann Ltd, 1985

[Cook 1990] Cook, N.J.: *The designer's guide to wind loading of building structures. Part 2: static structures.* Butterworth-Heinemann Ltd, 1990

[Counihan 1969] Counihan, J.: An Improved Method of Simulating an Atmospheric Boundary Layer in a Wind Tunnel. In: *Atmospheric Environment* 3 (1969), p. 197–214

[Counihan 1975] Counihan, J.: Adiabatic Atmospheric Boundary Layers: A review and Analysis of Data from Period 1880-1972. In: *Atmospheric Environment* 9 (1975), p. 871–905

[Crandall & Mark 1963] Crandall, S. H. ; Mark, W. D.: *Random Vibration in Mechanical Systems.* Academic Press, New York, 1963

[CTE] *CTE , Documento Básico SE-AE. Parte 3.3. Viento 2008. Código Técnico de Edificación*

[Davenport 1961] Davenport, A. G.: The Applications Of Statistical Concepts To the Wind Loading Of Structures. In: *Proceedings of The Institution of Civil Engineers* 19 (1961), p. 449–472

[Davenport 1962] Davenport, A. G.: The Response Of The Slender, Line-Like Structures To A Gusty Wind. In: *Proceedings of The Institution of Civil Engineers* 23 (1962), p. 389–408

[Davenport 1963] Davenport, A. G.: The buffeting of structures by gusts. In: *Proceedings, International Conference on Wind Effects on Building and Structures, Teddington U.K., 26-8 June*, 1963

[Davenport 1964] Davenport, A. G.: Note on the distribution of largest values of a random function with application to gust loading. In: *ICE Proceedings* 28 (1964), p. 187–196

[Davenport 1966] Davenport, A. G.: The estimation of load repetitions on structures with application to wind induced fatigue and overload. In: *Proceedings of the RILEM International Symposium on the "Effects of Repeated Loading of Materials and Structures". Mexico City, September 15-17*, 1966

[Davenport 1967] Davenport, A. G.: Gust loading factors. In: *Journal of the Structural Division* 93 (1967), p. 11–34

[Davenport 1971] Davenport, A. G.: On the statistical prediction of structural performance in the wind enviroment. In: *Preprint 1420, ASCE National Structural Engineering Meeting, Baltimore, Maryland.*, 1971

[Davenport 2007] Davenport, A. G.: *Wind Tunnel testing: A general outline.* The Boundary Layer Wind Tunnel Laboratory, University of Western Ontario, London, Canada, 2007

[Devroye 1986] Devroye, L.: *Non-Uniform Variate Random Generation.* Springer-Verlag New York Inc., 1986

[Diederich 1956] Diederich, F. W.: The Dynamic Response of a Large Airplane to Continuous Random Atmospheric Disturbances. In: *Journal of the Aeronautical Sciences* 23 (1956), p. 917–930

[DIN EN 1991-1-4/NA] *DIN EN1991-1-4/NA: 2010-12. Nationaler Anhang - Einwirkungen auf Tragwerken - Teil 1-4: Allgemeine Einwirkungen-Windlasten, Beuth Verlag GmbH, Berlin*

[Dionne & Davenport 1988] Dionne, M. ; Davenport, A. G.: A simple relationship between the gust response factor and fatigue damage. In: *Journal of Wind Engineering and Industrial Aerodynamics* 30 (1988), p. 45–54

[Dirlik 1985] Dirlik, T.: *Application of computers to fatigue analysis*, Warwick University, Coventry, England, PhD-thesis, 1985

[Duchene-Marullaz 1975] Duchene-Marullaz, P. H.: *Turbulence atmospherique au voisinage d'une ville.* Centre Scientifique & Technique du Batiment (CSTB), Division climatologie, EN-CLI, 1975

[Dyrbye & Hansen 1997] Dyrbye, C. ; Hansen, S. O.: *Wind Loads on Structures.* John Wiley & Sons, 1997

[Eaddy & Melbourne 2011] Eaddy, M. ; Melbourne, W. H.: Forces on stationary smooth and rough circular cylinders in turbulent flow. In: *13th International Conference on Wind Engineering (ICWE 13), Amsterdam, Holland*, 2011

[EN 1991-1-4] *EN 1991-1-4: Actions on structures - Part 1-4: General Actions - Wind Actions. CEN - European Committee for Standarization*

[EN 1993-1-9] *EN 1993-1-9: Design of steel structures - Part 1-9: Fatigue. CEN - European Committee for Standarization*

[ESDU 74031] *ESDU 74031: Characteristics of atmospheric turbulence near the ground. Part II: single point data for strong winds (neutral atmosphere). Engineering Sciences Data Unit, London, 1974*

[ESDU 75001] *ESDU 75001: Characteristics of atmospheric turbulence near the ground. Part III: variations in space and time for strong winds (neutral atmosphere). Engineering Sciences Data Unit, London, 1975*

[ESDU 80025] *ESDU 80025: Mean forces, pressures and flow field velocities for circular cylindrical structures: single cylinder with two dimensional flow. Engineering Sciences Data Unit, London, 1980*

[ESDU 81017] *ESDU 81017: Mean forces, pressures and flow field velocities for circular cylindrical structures: finite-length cylinders in uniform and shear flow. Engineering Sciences Data Unit, London, 1981*

[ESDU 85020] *ESDU 85020: Characteristics of atmospheric turbulence near the ground. Part II: single point data for strong winds (neutral atmosphere). Engineering Sciences Data Unit, London, 1990*

[Fage & Warsap 1929] Fage, A. ; Warsap, J. H.: The effects of turbulence and surface roughness on the drag of a ciruclar cylinder. Report No. 1283 / Aeronautical Research Committee. Air Ministry of England. 1929. – Research report

[Fichtl & McVehil 1970] Fichtl, G. H. ; McVehil, G. E.: Longitudinal and lateral spectra of turbulence in the atmospheric boundary layer at the Kennedy Space Center. In: *Journal of Applied Metereology* 9 (1970), p. 51–63

[Halfpenny & Kihm 2010] Halfpenny, A. ; Kihm, F.: Rainflow cycle counting and acoustic fatigue analysis techniques for random loading. In: *10th International Conference RASD, Southampton*, 2010

[Harris 1970] Harris, R. I.: The Nature of the Wind. In: *The Modern Design of Wind Sensitive Structures. Proc. of the Seminar, Paper 3*, 1970

[Harris 1990] Harris, R. I.: Some further thoughts on the spectrum of gustiness in strong winds. In: *Journal of Wind Engineering and Industrial Aerodynamics* 33 (1990), p. 461–477

[Holmes 2007] Holmes, J. D.: *Wind Loading of Structures*. Routledge Chapman & Hall, 2007

[Holmes 2009] Holmes, J. D.: Codification Of Wind Loads On Wind-Sensitive Structures. In: *International Journal of Space Structures* 24 (2009), p. 87–95

[Hölscher 1993] Hölscher, N.: *Ein multivariater Ansatz für die aerodynamische Übertragungsfunktion der Winddrücke in atmosphärischer Grenzschichtströmung. Mitteilung Nr. 93-3*, Ruhr-Universität Bochum. Institut für Konstruktiven Ingenieurbau, PhD-thesis, 1993

[Hurty & Rubinstein 1964] Hurty, W.C. ; Rubinstein, M.: *Dynamics of Structures.* Pretice-Hall, Inc. New Jersey, 1964

[Irwin 1981] Irwin, P. A.: The Design of Spires for Wind Simulation. In: *Journal of Wind Engineering and Industrial Aerodynamics* 7 (1981), p. 361–366

[Ishizaki & Yoshikawa 1972] Ishizaki, H. ; Yoshikawa, Y.: A wind tunnel model experiment of wind loading on curved roofs. In: *Bulletin of the Disaster Prevention Research Institute of Kyoto University* 21-4-195 (1972), p. 247–263

[ISO 4354:2009] *ISO 4354:2009 - Wind Actions on Structures. ISO - International Standard*

[Kaimal et al. 1972] Kaimal, J.C. ; Wyngaard, J.C. ; Cotè, Y. I.: Spectral characteristics of surface-layer turbulence. In: *Journal of the Royal Meteorological Society* 98 (1972), p. 563–589

[von Kàrmàn 1948] Kàrmàn, T. von: Progress in the statistical theory of turbulence. In: *Journal of Maritime Research* 7 (1948)

[Kemper 2013] Kemper, F.: *Böeninduzierte Schwingungsanfälligkeit von durchlässigen Fassadenelementen unter Berücksichtigung nichtlinearer Struktureigenschaften im Grenzzustand der Ermüdung*, RWTH Aachen, Germany, PhD-thesis, 2013

[Kemper & Feldmann 2011] Kemper, F. ; Feldmann, M.: Fatigue life prognosis for structural elements under stochastic wind loading based on spectral methods. In: *Proc. of the 8th International Conference on Structural Dynamics, EURODYN, Leuven, Belgium*, 2011, p. 1629–35

[Khanduri u. a. 1998] Khanduri, A. C. ; Stathopoulos, T. ; Bèdard, C.: Wind-induced interference effects on buildings - a review of the state-of-the-art. In: *Engineering Structures* 20 (1998), p. 617–630

[Kolmogorov 1941] Kolmogorov, A. N.: Dissipation of Energy in Locally Isotropic Turbulence. In: *Doklady Akademii Nauk SSSR* 32 (1941), p. 19–21

[Koo 2013] Koo, J.: Effects of frequency response spacing on vibration fatigue analysis. In: *Proceedings of the FISITA 2012 World Automotive Congress* Bd. 195, 2013, p. 253–265

[Kopp 2012] Kopp, G. A.: Aerodynamic mechanisms for wind loads on tilted, roof - mounted, solar arrays. In: *Journal Of Wind Engineering and Industrial Aerodynamics* 111 (2012), p. 40–52

[Kwon & Kareem 2013] Kwon, D. K. ; Kareem, A.: Comparative study of major international wind codes and standards for wind effects on tall buildings. In: *Engineering Structures* 51 (2013), p. 23–35

[Longuet-Higgins 1952] Longuet-Higgins, M. S.: On the statistical distribution of the heights of sea waves. In: *Journal of Marine Research* 11 (1952), p. 245–266

[Maier-Erbacher & Plate 1988] Maier-Erbacher, J. ; Plate, E. J.: Aerodynamische Belastung zylindrischer Bauwerke / Sonderforschungsbereich 210/ET/48. Universität Karlsruhe. 1988. – Research report

[Matsuishi & Endo 1968] Matsuishi, M. ; Endo, T.: *Fatigue of metals subjected to varying stress*. Japan Society of Mechanical Engineers, 1968

[Meseguer et al. 2013] Meseguer, J. ; Sanz, A. ; Pindado, S. ; Franchini, S. ; Alonso, G.: *Efectos del Viento en Edificaciones y Estructuras*. Grupo Editoral Garceta, 2013

[Morison et al. 1950] Morison, J. R. ; O'Brien, M.D. ; Johnson, J.W. ; Schaaf, S. A.: The force exerted by surface waves on piles. In: *Journal of Petroleum Techniques* 189 (1950), p. 61–67

[Newberry et al. 1973] Newberry, C. W. ; Eaton, K. J. ; Mayne, J. R.: Wind Loading on Tall Buildings - Further Results from Royex House. Paper29/73 / Building Research Establishment HMSO. 1973. – Research report

[Niemann 1992] Niemann, H. J.: Das Verfahren zur Erfassung der Böenwirkung nach CEN 1 ein Vergleich mit der Vornorm DIN 1055 Teil 40 und dem ISO- Standard 4354. In: *WtG Bericht 2. Windlastnormen nach 1992* (1992), p. 45–65

[Niemann 1997] Niemann, H. J.: Die Spektraldichte der Windturbulenz als Grundlage zur rechnerischen und experimentellen Untersuchung böenerregter Schwingungen. In: *WtG Bericht 4. Windkanalanwendungen für die Baupraxis* (1997), p. 178–197

[Niemann 2013] Niemann, H. J.: International Standarization of Wind Actions on Chimneys. In: *CICIND Report* 29-2 (2013), p. 75–83

[Niemann & Hölscher 1990] Niemann, H. J. ; Hölscher, N.: A review of recent experiments on the flow past circular cylinders. In: *Journal of Wind Engineering and Industrial Aerodynamics* 33 (1990), p. 197–209

[Peil 1993] Peil, U.: Baudynamik. In: *Stahlbau Handbuch* 1- Part A (1993), p. 379–451

[Peil & Behrens 2000] Peil, U. ; Behrens, M.: Ermüdung von Beleuchtungs- und Signal masten durch den böigen Wind / DASt Forschungsbericht N.6330. 2000. – Research report

[Peil & Nölle 1995] Peil, U. ; Nölle, H.: Ermittlung der Lebensdauer hoher windbeanspruchter Bauwerke. In: *Bauingenieur* 70 (1995), p. 21–33

[Petersen u. Reppermund 1986] Petersen, C. ; Reppermund, K.: Zur Frage der Materialermüdung bei Windböenbeanspruchungen. In: *Festschrift Roik* (1986), p. 101–118

[Ribeiro 1991] Ribeiro, J. L. D.: Effects on surface roughness on the two-dimnesional flow past circular cylinders I: mean forces and pressures. In: *Journal of Wind Engineering and Industrial Aerodynamics* 37 (1991), p. 311–326

[Rice 1945] Rice, S. O.: Mathematical analysis of random noise. In: *Bell System Technical Journal* 19 (1945), p. 46–156

[Ruscheweyh 1997] Ruscheweyh, H.: Interferenzwirkung zwischen Schornstein und Gebäude auf die wirbelerregte Schwingung. In: *WtG Bericht 5. Baukonstruktion unter Windeinwirkung* (1997), p. 89–99

[Schewe 1983] Schewe, G.: On the force fluctuations acting on a circular cylinder in cross flow from subcritical up to transcritical Reynolds numbers. In: *Journal of Fluid Mechanics* 133 (1983), p. 265–285

[Schewe 1990] Schewe, G.: Beispiele für Kraftmessungen im Windkanal mit piezoelektrischen Mehrkomponentenmesselementen. In: *Zeitschrift für Flugwissenschaften und Weltraumforschung* 14 (1990), p. 32–37

[Schrader 1994] Schrader, P.: *Die statistische Stabilität gemessener integraler Längenmasse und anderer Windparameter*, Sonderforschungsbereich Tragwerksdynamik Ruhr-Universität Bochum. SFB 151-Berichte Nr. 26, PhD-thesis, 1994

[Schroers & Zilch 1981] Schroers, H. ; Zilch, K.: Messungen der Starkwindstruktur und deren Auswirkungen auf das Windlastkonzept von Bauwerke. Berichte 35/36 Gebäudeaerodynamik / Deutsche Forschungsgesellschaft DFG. 1981. – Research report

[Schümmer 2003] Schümmer, P.: *Einfluss der Oberflächenrauigkeit und der Turbulenz auf die windinduzierten Kräfte an einem Kreiszylinder*, Lehrstuhl für Stahlbau, RWTH Aachen, Diplomarbeit, 2003

[Simiu 1973] Simiu, E.: Gust Factors And Alongwind Pressure Correlations. In: *Journal of the Structural Division - Proceedings of the American Society of Civil Engineers* 99 (1973), p. 773–783

[Simiu 1980] Simiu, E.: Revised Procedure For Estimating Along-Wind Response. In: *Journal of the Structural Division - Proceedings of the American Society of Civil Engineers* 106 (1980), p. 1–10

[Simiu & Lozier 1975] Simiu, E. ; Lozier, D. W.: The Buffeting of Tall Structures by Strong Winds / U.S. Department of Commerce. 1975. – Research report

[Simiu & Scanlan 1985] Simiu, E. ; Scanlan, R. H.: *Wind Effects on Structures*. John Wiley & Sons, 1985

[Sockel 1984] Sockel, H.: *Aerodynamik der Bauwerke*. Friedr. Vieweg & Sohn, 1984

[Solari 1982] Solari, G.: Along-wind Response Estimation: Closed Form Solution. In: *Journal of Structural Division* 108 (1982), p. 225–244

[Solari 1987] Solari, G.: Turbulence modelling for gust loading. In: *Journal of Structural Engineering* 113 (1987), p. 1550–1569

[Solari 1988a] Solari, G.: Dynamic Alongwind Response Of Structures by Equivalent Wind Spectrum Technique / Istituto Di Scienza Delle Costruzioni - Universita di Genova - Facolta di Ingegneria. 1988. – Research report

[Solari 1988b] Solari, G.: Equivalent Wind Spectrum Technique: Theory and Applications. In: *Journal of Structural Engineering* 114 (1988), p. 1303–1323

[Solari 1990] Solari, G.: A Generalized Definition of Gust Factor. In: *Journal of Wind Engineering and Industrial Aerodynamics* 36 (1990), p. 539–548

[Solari 1993a] Solari, G.: Gust Buffeting. I: Peak Wind Velocity and Equivalent Pressure. In: *Journal of Structural Engineering* 119 (1993), p. 365–382

[Solari 1993b] Solari, G.: Gust Buffeting. II: Dynamic Alongwind Response. In: *Journal of Structural Engineering* 119 (1993), p. 383–398

[Spaethe & Trätner 1992] Spaethe, G. ; Trätner, A.: Winderregte Querschwingungen infolge Wirbelablösung bei kreiszylindrischen Bauwerken in Gruppen- und Reihenanordnung / Deutsches Institut für Bautechnik -DIBt-, Berlin. 1992. – Research report

[SPP 1981] *Gebäudeaerodynamik Heft 35-36.* Institut für Konstruktive Ingenieurbau der Ruhr-Universität Bochum, 1981

[Standen 1972] Standen, N.M.: A Spire Array for Generating Thick Turbulent Shear Layers for Natural Wind Simulation in Wind Tunnels. Technical Report LTR-LA-94 / National Aeronautical Establishment, Ottawa, Canada. 1972. – Research report

[Stathopoulos 1984] Stathopoulos, T.: Adverse Wind Loads on Low Buildings Due to Buffeting. In: *Journal of Structural Engineering* 110 (1984), p. 2374–2392

[Stull 1991] Stull, R. B.: *An Introduction to Boundary Layer Meteorology.* Kluwer Academic Publishers, 1991

[Telljohann 1998] Telljohann, G.: *Turbulenzmodellierung des Windes für Schwingungsuntersuchungen hoher, schlanker Bauwerke*, Institut für Stahlbau, Technische Universität Braunschweig, PhD-thesis, 1998

[Teunissen 1979] Teunissen, H. W.: Structure of mean winds and turbulence in the planetary boundary layer over rural terrain. Internal Report MSRB 79-1 / Atmospheric Enviroment Service, Downsview, Ontario, Canada. 1979. – Research report

[Troen & Petersen 1979] Troen, I. ; Petersen, E. L.: *European Wind Atlas.* National Laboratory of Riso, Denmark, 1979

[Tschanz 1982] Tschanz, T.: Measurement of total dynamic loads using elastic models with high natural frequencies. In: *Wind Tunnel Modeling for Civil Engineering Applications. National Bureau of Standards. Washington D.C.* (1982), p. 296–312

[Tse et al. 2009] Tse, K. T. ; Hitchcock, P. A. ; Kwok, K. C. S.: Mode shape linearization for HFBB analysis of wind-excited complex tall buildings. In: *Engineering Structures* 31 (2009), p. 675–685

[Vellozzi & Cohen 1968] Vellozzi, J. ; Cohen, E.: Gust Response Factors. In: *Journal Of the Structural Division ASCE* ST6 (1968), p. 1295–1313

[Verboom 2010] Verboom, G. K.: Gust Factor - Revisited. In: *CICIND Report* 26-2 (2010), p. 69–76

[Vickery 1963] Vickery, B. J.: Gust Response Factors - Discussion. In: *Journal of the Structural Division ASCE* ST3 (1963), p. 494–501

[Vickery 1965] Vickery, B. J.: On the flow behind a coarse grid and its use as a model of atmospheric turbulence in studies related to wind loads on buildings / NPL Aero Report 1143. 1965. – Research report

[Vickery 1970] Vickery, B. J.: On The Reliability of Gust Loading Factors / National Bureau of Standards. 1970. – Research report

[Wagner 2010] Wagner, T.: *Modelling of Wind Born Ice Accretion on Power Transmission Lines*, Insitute of Steel Structures, TU Braunschweig., PhD-thesis, 2010

[Wieringa 1989] Wieringa, J.: Shapes of annual distributions of wind speed observed on high meteorological masts. In: *Journal of Boundary-Layer Meteorology* 47 (1989), p. 85–110

[Wieselsberger & Betz 1923] Wieselsberger, C. ; Betz, A.: Versuche über den Luftwiderstand gerundeter und kantiger Körper / Ergebnisse der Aerodynamische Versuchsanstalt zu Göttingen. 1923. – Research report

[Willecke 2013] Willecke, A.: *Simulation der Wirbelerregung unter Berücksichtigung realistischer Windprofile*. Shaker Verlag, 2013

[Wirsching & Light 1980] Wirsching, P. H. ; Light, M. C.: Fatigue under wide band random stresses. In: *Journal of the Structural Division ASCE* 196 (1980), p. 1563–1607

[WtG] *Windkanalversuche in der Gebäudeaerodynamik. Windtechnologische Gesellschaft WtG*

[Zhou et al. 1999a] Zhou, Y. ; Gu, M. ; Xiang, H. F.: Alongwind Static Equivalent Wind Loads And Responses Of Tall Buildings. Part I: Unfavorable Distributions Of Static Equivalent Wind Loads. In: *Journal of Wind Engineering and Industrial Aerodynamics* 79 (1999), p. 135–150

[Zhou & Kareem 2003] Zhou, Y. ; Kareem, A.: Aerodynamic admittance function of tall buildings. In: *Proceedings of 11th International Conference on Wind Engineering, Lubbock, USA*, 2003

[Zhou et al. 1999b] Zhou, Y. ; Kareem, A. ; Gu, M.: Gust Loading Factors For Design Applications. In: *Proceedings of the 10th International Conference on Wind Engineering ICWE, Copenhagen* (1999), p. 169–176